NONLINEAR PHENOMENA IN HIGHER ORDER MODE FIBER FOR DEVELOPMENT OF LIGHT SOURCES FOR BIOMEDICAL IMAGING

A Dissertation

Presented to the Faculty of the Graduate School

of Cornell University

In Partial Fulfillment of the Requirements for the Degree of

Doctor of Philosophy

by

Jennifer Hanmei Lee

January 2011

NONLINEAR PHENOMENA IN HIGHER ORDER MODE FIBER FOR DEVELOPMENT OF LIGHT SOURCES FOR BIOMEDICAL IMAGING

Jennifer Hanmei Lee, Ph. D.

Cornell University 2011

Higher order mode (HOM) fibers present a breakthrough in fiber design, in its ability to provide anomalous dispersion in solid, silica-based fiber below 1300 nm. Anomalous dispersion is especially interesting for purposes of short-pulse propagation, since soliton propagation requires this sign of dispersion to balance the nonlinear phase induced by self-phase modulation. Since silica has normal material dispersion below 1300 nm, and a fundamental mode propagating in single-mode fiber has negative waveguide dispersion, access to anomalous dispersion below 1300 nm has been limited to special microstructured fibers. These microstructured fibers, however, are limited to regimes of power too extreme for biomedical applications. Hollow-core photonic bandgap fibers (PBGF), with their low nonlinearity, require pulse energies of many hundreds of nanojoules, while solid-core photonic crystal fibers (PCF), with their tight confinement, support only fractions of nanojoule-pulses. HOM fibers, are all-solid silica but can attain anomalous waveguide dispersion (and thus anomalous dispersion below 1300 nm) by propagating light solely in a higher-order mode (LP_{02}) of the fiber. With moderate nonlinearity (compared to PBGF) and relatively large mode area (compared to PCF), HOM fibers aim to provide 1-10 nJ pulses at wavelengths suitable for biomedical imaging applications. We demonstrate the nonlinear phenomena of soliton self-frequency shift and Cerenkov radiation generation in HOM fibers for providing short energetic pulses. By pumping an HOM

fiber with a free-space femtosecond fiber laser, Raman-shifted solitons and a compressible radiation band (Cerenkov radiation) on the long-wavelength side of the zero-dispersion wavelength were observed, spanning 1064 nm to 1450 nm. In addition, with longer fiber lengths and a picosecond fiber laser source, we were able to demonstrate an all-fiber system for generating shifted solitons and Cerenkov radiation. This all-fiber system was successfully used as a light source for two-photon fluorescence microscopy, and the focusing properties of the LP_{02} mode were carefully characterized.

BIOGRAPHICAL SKETCH

Jennifer Hanmei Lee was born in Pasadena, California and grew up in Hsinchu, Taiwan. The daughter of an optoelectronics engineer and a nuclear physicist, Jennifer was about 10 when her mother first attempted to teach her about exponential functions. Unfortunately, the concept was a few years beyond her elementary math skills, and she was unable to grasp its beauty and utility. Nevertheless, she favored math and science to language and history, and aspired to be a math teacher or Olympian.

In the summer of 1998, Jennifer attended an astronomy summer program in Ojai, California, where she learned the joys of calculus, physics, planetary orbits, computer programming, and staying up late. She liked these intellectual pursuits so much that she decided to attend the California Institute of Technology. At the persuasion of her father to pursue something more “practical” than gazing at the night sky, Jennifer chose to major in Applied Physics. Fortunately for her, this decision also meant she would take the popular Introduction to Optics class, be wowed by the demonstrations, and start down the path for her eventual career. It was also at Caltech that Jennifer had her brush with NCAA athletic glory. Due to the sore lack of women on campus, she garnered a spot on the varsity women’s basketball team despite not having any organized basketball experience. The team rarely won, but she learned a valuable lesson in redefining the words “success” and “failure.”

After finishing her undergraduate degree in sunny Southern California in 2003, Jennifer decided it was time for a change in climate and relocated to Ithaca, NY to begin her graduate studies at Cornell University. In the spring of 2004 she joined the lab of Professor Chris Xu and began her long march to understanding tiny glass fibers.

For Mommy, Daddy, and Jeffrey

ACKNOWLEDGMENTS

My journey through graduate school would not be complete, nor even have happened, without the help of some very gracious people and brilliant scientists. I am deeply grateful to Professor Chris Xu, my advisor, for his guidance and insight, and for teaching me how to be a resourceful scientist. I thank Professors Watt Webb, Frank Wise, Alex Gaeta, and Warren Zipfel for generous loaning of equipment, graduate student- and postdoc-manpower, and for the numerous collaboration opportunities between the Xu group and theirs.

Along the way I've had opportunities to collaborate with scientists outside of our research group, both at Cornell and externally. The first floor of Clark Hall is a hotbed of exciting optics research; I thank Khanh Kieu and Andy Chong from the Wise group for technical assistance with my experiments and for being a great resource on fiber lasers and amplifiers so nearby. My doctoral research has centered on a special fiber device from OFS in New Jersey and Denmark. I am indebted to the scientists at OFS — Siddharth Ramachandran, Samir Ghalmi, Man Yan, Lars Grüner-Nielsen, and Kim Jesperson — for designing, making, modifying, and remaking these devices. It has been a stimulating and fruitful collaboration, and I am glad to have been part of it.

No graduate student is an island. I have had the fortune of sharing an office and lab space with some fabulous friends. I owe the first thanks to Jim van Howe, who had the unfortunate duty of showing me the ropes, for his patience and imparted expertise, and for letting me tag along his final two projects. I owe much of my Matlab prowess to Kristen Reichenbach; I also thank her for her example of courage, in being undeterred by a male-dominated field, and in choosing a less-traveled career path. I would like to recognize Mike Durst and Demirhan Kobat for bravely enduring many

years with me in the narrow confines of 148 Clark. These two have been there to answer my dumb physics questions, help me troubleshoot experiments, philosophize about life with, and (more importantly) challenge my NCAA basketball pedigree. I thank Mike for always being positive and going the extra mile to be helpful, and for opening his home whenever there was a game I wanted to watch. I thank Demirhan for his help with the imaging experiments, his flexibility and availability, and for being a fellow night owl those odd morning hours in lab. It has been a pleasure working with them; I will miss them. In the last few years, Ji Cheng and Ke Wang have joined me in the HOM fiber effort. I thank these two sharp minds for their intuition and the enlightening discussions we've had about nonlinear fiber phenomena. I would also like to thank the other residents of our single-window office: Scott Howard, David Rivera, and Adam Straub; for being an endless fount of both intellectual and mundane fun.

The final thanks go to my friends and family who have supported me emotionally and spiritually through the highs and lows of these graduate school years. They have always been there, encouraging me, distracting me, feeding me, praying for me, and reminding me to put things in the eternal perspective. I want to especially acknowledge my friends in the Graduate Christian Fellowship, for being my family away from home; my climbing buddies, for making sure I stay safe while I have fun; my roommate Hannah, for being so thoughtful; and my childhood friends Maria and Jean, for being like sisters to me. My immediate and extended family, though thousands of miles away, have been incessant with phone calls of encouragement and gentle nudging to "hurry up, graduate and come home." I thank them for their love and patience. This thesis is dedicated to my parents and my brother, for teaching me so much, but especially for teaching me faith and perseverance. Soli Deo Gloria.

TABLE OF CONTENTS

LIST OF FIGURES

LIST OF TABLES

LIST OF ABBREVIATIONS

ADC	Analog-to-digital converter
BS	Beam splitter
CARS	Coherent anti-Stokes Raman scattering
CCD	Charge-coupled device
CFBG	Chirped fiber Bragg grating
CW	Continuous-wave
DC	Dichroic
EO	Electro-optic
ER	Extinction ratio
FWHM	Full-width at half-maximum
GNLSE	Generalized nonlinear Schrödinger equation
GVD	Group velocity dispersion
HOM	Higher order mode
HWHM	Half-width at half-maximum
IM	Intensity modulator
LBO	Lithium triborate
LPG	Long period grating
MZ	Mach-Zehnder
NLSE	Nonlinear Schrödinger equation
OPO	Optical parametric oscillator
PBGF	Photonic bandgap fiber
PC	Pulse-carver
PCF	Photonic crystal fiber
PM	Phase modulator
PMT	Photomultiplier tube
PP	Pulse-picker
PSF	Point-spread function
RBW	Resolution bandwidth
RF	Radio frequency
SESAM	Semiconductor saturable absorber mirror
SMF	Single-mode fiber
SPM	Self-phase modulation
SRS	Stimulated Raman scattering
SSFS	Soliton self-frequency shift
STED	Stimulated emission depletion
TPEF	Two-photon emission fluorescence
TPM	Two-photon fluorescence microscopy
VOA	Variable optical attenuator
YDFA	Ytterbium-doped fiber amplifier
ZDW	Zero-dispersion wavelength

CHAPTER 1

INTRODUCTION

1.1 Optical Fibers

Optical fibers, the thin strands of glass that bring us our high-speed, high-capacity data links, had its beginnings in Victorian light shows [1]. In 1841, Daniel Colladon used focused light to illuminate streams of water for fluid flow demonstrations in a dimly-lit lecture hall. He observed that the streams of water guided the light without it escaping, unless the stream was perturbed by an obstacle or the stream broke up [2]. The effect was showy, and led to the construction of many illuminated fountains across Europe in the late 1800s. This concept of light guiding was extended to glass rods, and much work was done in the late 1800s and early 1900s using glass rods for illumination and image transfer. Glass rods gradually gave way to thinner glass fibers, which were flexible and thus more versatile. While promising, early glass fibers were lossy and ineffective for delivering light more than a few meters. It was the development of glass-clad fibers in the 1950s [3, 4] and low-loss optical fiber in the 60s and 70s [5, 6] that truly enabled the optical fiber communications revolution. While fiber communications is arguably the realm of greatest commercial impact for optical fibers, optical fibers have also left its mark on the realms of illumination, light generation, metrology, medicine, and remote sensing.

The interaction of light with the optical fiber gives rise to linear effects such as chromatic dispersion and absorption, as well as nonlinear effects such as self- and cross-phase modulation, stimulated Raman and Brillouin scattering, and four-wave mixing. These effects, detrimental to signal fidelity in fiber communications, are actually the enabling factors for creating novel light sources based on nonlinear optical

phenomena. The core-guiding property of optical fiber gives localization of these effects, lending spatial confinement of the light-matter interactions and isolating these interactions from the external environment. This has special appeal for creating light sources: first, in-fiber confinement replaces complex free space optical setups, making these light sources alignment-free and easy-to-operate; and second, the isolation provided by the fiber-based approach makes these devices robust to environmental perturbations. In addition, the linear and nonlinear properties of a fiber can be tuned by engineering its material, structure, and geometry. This design freedom extends the capabilities of conventional and novel fiber structures. One example of this is the higher order mode (HOM) fiber, which was recently demonstrated to exhibit dispersion characteristics previously thought impossible for its fiber geometry [7]. With proper design, the HOM fiber can access a unique set of dispersion and nonlinearity characteristics that enable energetic pulse generation in the near infrared.

1.2 Light Sources for Nonlinear Microscopy

Since its beginnings, optical fibers have attracted much attention for applications to medicine, especially for remote viewing of internal body parts. The light guiding properties, mechanical flexibility, and small size of optical fibers are well-suited to the development of endoscopes. However, traditional white light reflection endoscopy is limited in resolution and penetration depth. Patient comfort and accuracy of medical diagnostics would be greatly improved if an endoscope were capable of imaging tissue *in situ* with the same resolution and specificity of conventional biopsy techniques of tissue excision and histology. This noninvasive "optical biopsy" is made possible by combining a fiber endoscope with multiphoton microscopy, which has fine lateral resolution and optical sectioning capability [8, 9]. One hurdle to the realization of such a multiphoton endoscope is the availability of an

appropriate light source. To excite the nonlinear processes involved in multiphoton microscopy, one needs a light source that provides short, energetic pulses in the near infrared. The current standards for such an excitation source are the Ti:Sapphire laser and the synchronously-pumped optical parametric oscillator (OPO). These solid state lasers, while versatile and powerful, are bulky, expensive, and difficult to operate. As such, they are ill-suited for the clinical setting. The work presented here focuses on the development of fiber-based light sources for multiphoton endoscopy. The engineerability and versatility of HOM fibers make it appealing as a platform on which to build this technology. The goal is simple: an easy-to-use, easy-to-transport, robust light source delivering high peak power, energetic pulses at wavelengths suitable for two-photon microscopy.

In this dissertation, I outline our efforts to develop a light source based on an HOM fiber, and its application to nonlinear microscopy. In Chapter 2, I briefly summarize our methods for numerically simulating fiber propagation and introduce non-conventional fiber designs. In Chapter 3, I introduce the phenomenon of soliton self-frequency shift (SSFS) as it has been observed in conventional and specialty fibers, and present the demonstration of SSFS in a HOM fiber for a tunable wavelength light source between 1.0 and 1.3 μm. In Chapter 4, I show that the band of Cerenkov radiation generated as a consequence of a shifting soliton approaching a zero dispersion wavelength is compressible and has potential to be another short-pulse source from the same HOM fiber. In Chapter 5, I present an all-fiber source based on nonlinear propagation in HOM fiber, as enabled by longer fiber length and a picosecond fiber laser source. In Chapter 6, the spatial imaging properties of the HOM fiber output are studied by characterizing its two-photon fluorescence point spread function (PSF). Finally, in Chapter 7, I summarize the presented work and outline a few potential directions for further study of HOM fibers and their applications in

biomedical imaging. Appendix A presents a separate but related effort to develop sources for nonlinear microscopy: a time lens source synchronized to a modelocked laser for coherent Raman microscopy.

REFERENCES

1. J. Hecht, *City of Light*, New York: Oxford University Press, 1999.

2. D. Colladon, "On the reflections of a ray of light inside a parabolic liquid stream," *Comptes Rendus*, vol. 15, pp. 800, 1842.

3. B. O'Brien, "Optical Image Forming Devices," U.S. Patent 2,825,260, March 4, 1958.

4. A. C. S. van Heel, "A New Method of transporting Optical Images without Aberrations," vol. 173, pp. 4392, 1954.

5. K. C. Kao and G. A. Hockham, "Dielectric-Fibre Surface Waveguides for optical frequencies," *Proceedings of the IEE*, vol. 113, pp. 1151-1158, 1966.

6. D. B. Keck, R. D. Maurer and P. C. Schultz, "On the ultimate lower limit of attenuation in glass optical waveguides," *Applied Physics Letters*, vol. 33, pp. 307-309, 1973.

7. S. Ramachandran, S. Ghalmi, J. W. Nicholson, M. F. Yan, P. Wisk, E. Monberg and F. V. Dimarcello, "Anomalous dispersion in a solid, silica-based fiber," *Optics Letters*, vol. 31, pp. 2532-2534, 2006.

8. W. Denk, J. Strickler and W. Webb, "Two-photon laser scanning fluorescence microscopy," *Science*, vol. 248, pp. 73-76, 1990.

9. W. R. Zipfel, R. M. Williams and W. W. Webb, "Nonlinear magic: multiphoton microscopy in the biosciences," *Nature Biotechnology*, vol. 21, pp. 1369-1377, 2003.

CHAPTER 2

BACKGROUND

2.1 Numerical Modeling of Fiber Propagation

To understand the propagation of light in an HOM fiber, we consider the evolution of a pulse as described by the generalized nonlinear Schrödinger equation (GNLSE) [1, 2]. The GNLSE can be derived from Maxwell's equations, and makes the assumption that the light is of a single linear polarization whose polarization state is not affected during propagation. We also assume that there are no back-propagating waves, and we can decompose the pulse into its carrier and envelope $E(r,t) = \frac{1}{2}\left[E(x,y,z,t)\exp(-i\omega_o t) + c.c\right]$. Writing the wave equation in the frequency domain, it can be solved by separation of variables for the transverse mode and the spectral envelope $\tilde{A}(z,\omega-\omega_0)$. Transforming back to the time-domain, the GNLSE describing the envelope $A(z,T)$ in the moving reference frame of the traveling light ($T = t - z/v_g$, v_g being group velocity of the envelope) is:

$$\frac{\partial A}{\partial z} + \frac{\alpha}{2}A - \sum_{k\geq 2}\frac{i^{k+1}}{k!}\beta_k\frac{\partial^k A}{\partial T^k} = i\gamma\left(1 + i\tau_{shock}\frac{\partial}{\partial T}\right)\left(A(z,T)\int_{-\infty}^{\infty}R(T')\left|A(z,T-T')\right|^2 dT'\right) \tag{2.1}$$

where α is the linear absorption, and β_k are the dispersion coefficients given by the Taylor expansion of propagation constant β about carrier frequency ω_0:

$$\beta(\omega) = \beta_0 + \beta_1\left(\omega-\omega_0\right) + \frac{1}{2}\beta_2\left(\omega-\omega_0\right)^2 + \frac{1}{6}\beta_3\left(\omega-\omega_0\right)^3 + \ldots \tag{2.2}$$

β_2 is related to the dispersion parameter D by $D = -\frac{2\pi c}{\lambda^2}\beta_2$. In this dissertation, D will primarily be used in describing fiber dispersion. The parameter γ represents the nonlinear effects from the nonlinear refractive index n_2 and is given by the relation

$$\gamma = \frac{n_2 \omega_0}{c A_{eff}(\omega_0)} \tag{2.3}$$

$\tau_{shock}\,\partial/\partial t$ describes the self-steepening and shock formation, and is related to the carrier frequency: $\tau_{shock} = 1/\omega_0$. *R(T)* describes the Raman response, and can be approximated well by the following expression:

$$R(t) = (1 - f_R)\delta(t) + f_R \left[\frac{\tau_1^2 + \tau_2^2}{\tau_1 \tau_2^2} \exp\left({}^{-t}\!/_{\tau_2} \right) \sin\left({}^{t}\!/_{\tau_1} \right) \right] H(t) \tag{2.4}$$

The parameters are set to fit the measured Raman response of silica: $f_R = 0.18$, $\tau_1 =$ 12.2 fs, and $\tau_2 = 32$ fs [1, 3]. *H(t)* is the Heaviside step function.

To understand the effects of propagation, we need to solve Eqn. (2.1). We describe in this chapter two commonly used methods: the split-step Fourier method, and solving the frequency-domain GNLSE.

2.1.1 Split-step Fourier Method

The split-step Fourier method solves the GNLSE in the frequency domain for linear effects, and in the time domain for nonlinear effects [1]. For many-cycle pulses, we assume the envelope is slowly varying and Taylor-expand the squared-magnitude of the envelope function:

$$\left|A(z, T - T')\right|^2 = \left|A(z,T)\right|^2 - T' \frac{\partial}{\partial T} \left|A(z,T)\right|^2 + \ldots \tag{2.5}$$

Inserting this into (2.1), we can pull *A(z,T)* out of the integrals, yielding:

$$\begin{aligned} &\frac{\partial A}{\partial z} + \frac{\alpha}{2} A - \sum_{k \geq 2} \frac{i^{k+1}}{k!} \beta_k \frac{\partial^k A}{\partial T^k} \\ &= i\gamma \left(\begin{array}{l} A\left|A\right|^2 \int_{-\infty}^{\infty} R(T')dT' + i\tau_{shock} \frac{\partial}{\partial T} A\left|A\right|^2 \int_{-\infty}^{\infty} R(T')dT' \\ + A \frac{\partial \left|A\right|^2}{\partial T} \int_{-\infty}^{\infty} T' R(T')dT' + i\tau_{shock} \frac{\partial}{\partial T} A \frac{\partial \left|A\right|^2}{\partial T} \int_{-\infty}^{\infty} T' R(T')dT' \end{array} \right) \end{aligned} \tag{2.6}$$

We simplify the GNLSE using $\int_{-\infty}^{\infty} R(t)dt = 1$ and defining $T_R = \int_{-\infty}^{\infty} tR(t)dt$. While the Raman response is accurately represented by the full integral form of T_R, when the

slope of the Raman gain over the pulse spectrum is linear, T_R can be reasonably approximated as a constant [4].

$$\frac{\partial A}{\partial z}+\frac{\alpha}{2}A-\sum_{k\geq 2}\frac{i^{k+1}}{k!}\beta_k\frac{\partial^k A}{\partial T^k}=i\gamma\left(A|A|^2+i\tau_{shock}\frac{\partial}{\partial T}A|A|^2+T_R A\frac{\partial|A|^2}{\partial T}\right) \tag{2.7}$$

The final term in (2.6), proportional to $\tau_{shock}T_R$, is small and does not appear in (2.7).

To employ the split-step method, we will group the terms and write the GNLSE in the form

$$\frac{\partial A}{\partial z}=\left(\hat{D}+\hat{N}\right)A \tag{2.8}$$

Where the linear operator $\hat{D}$ represents all the linear effects: dispersion, linear absorption:

$$\hat{D}=-\frac{\alpha}{2}+\sum_{k\geq 2}\frac{i^{k+1}}{k!}\beta_k\frac{\partial^k}{\partial T^k} \tag{2.9}$$

And the nonlinear operator $\hat{N}$ represents the nonlinear effects; here intensity-dependent nonlinear index, self-steepening, shock, and Raman scattering:

$$\hat{N}=i\gamma\left(|A|^2+\frac{i}{\omega_0}\frac{1}{A}\frac{\partial}{\partial T}\left(|A|^2A\right)-T_R\frac{\partial|A|^2}{\partial T}\right) \tag{2.10}$$

The length of propagation is divided into many small steps Δz, and at each step, the linear and nonlinear effects are considered separately. In the first half of the step $\Delta z/2$, we set $\hat{N}=0$ and solve the NLSE with only linear effects in the Fourier domain. The operator $\hat{D}$ in the Fourier domain is

$$\hat{D}(i\omega')=-\frac{\alpha}{2}+\sum_{k\geq 2}\frac{i^{k+1}}{k!}\beta_k(i\omega')^k \tag{2.11}$$

We write for clarity in the shifted frequencies $\omega'=\omega-\omega_0$. The propagation half-step is described by:

$$\begin{aligned}&A(z,T)\xrightarrow{FT}\tilde{A}(z,\omega')\\&\tilde{A}(z+\Delta z/2,\omega')=\tilde{A}(z,\omega')\exp\left[\hat{D}(i\omega')\frac{\Delta z}{2}\right]\end{aligned} \tag{2.12}$$

In the middle of the step, we set $\hat{D} = 0$ and solve the GNLSE with only nonlinear effects in the time domain:

$$\begin{aligned} &\tilde{A}(z+\Delta z/2,\omega') \xrightarrow{FT^{-1}} A(z+\Delta z/2,T) \\ &A(z+\Delta z/2,T) = A(z+\Delta z/2,T)\exp\left[\hat{N}\Delta z\right] \end{aligned} \tag{2.13}$$

For the second half of the step, we once again set $\hat{N} = 0$ and apply linear effects:

$$\begin{aligned} &A(z+\Delta z/2,T) \xrightarrow{FT} \tilde{A}(z+\Delta z/2,\omega') \\ &\tilde{A}(z+\Delta z,\omega') = \tilde{A}(z+\Delta z/2,\omega')\exp\left[\hat{D}(i\omega')\frac{\Delta z}{2}\right] \end{aligned} \tag{2.14}$$

For judicious choice of step size and time window, the split-step method is effective and fast for calculating propagation of pulses as short as tens of femtoseconds. The split-step Fourier method was the numerical method used in Chapters 3 and 4 of this dissertation for understanding the propagation of femtosecond input pulses in HOM fibers.

2.1.2 Integrating the GNLSE in the Frequency Domain

Another method to solve the GNLSE is by solving the frequency domain ordinary differential equation directly [2]. Doing so, it is straightforward to incorporate the frequency dependence of A_{eff}, which in the split-step Fourier method described above, could only be estimated by a single $A_{eff}(\omega_0)$ at each propagation step. To obtain the GNLSE in the Fourier domain, we take the Fourier transform of (2.1).

$$\frac{\partial\tilde{A}}{\partial z} + \frac{\alpha}{2}\tilde{A} + \sum_{k\geq 2}\frac{i^{k+1}}{k!}\beta_k(i\omega')^k\tilde{A} = i\gamma(-\tau\omega')FT\left\{A(z,T)\int_{-\infty}^{\infty}R(T')\left|A(z,T-T')\right|^2 dT'\right\} \tag{2.15}$$

If we group the linearly dispersive terms on the left hand side of the equation as an operator $\hat{L}$

$$\hat{L} = -\frac{\alpha}{2} + i\sum_{k\geq 2}\frac{1}{k!}\beta_k(\omega')^k \tag{2.16}$$

And make the variable substitution for the envelope

$$\tilde{A}'(z,\omega') = \tilde{A}(z,\omega')\exp(-\hat{L}z) \tag{2.17}$$

As well as the following substitutions:

$$\begin{aligned} \bar{A}(z,T) &= FT^{-1}\left\{\frac{\tilde{A}(z,\omega')}{A_{eff}^{1/4}(\omega')}\right\} \\ \bar{\gamma}(\omega') &= \frac{n_2 n_0 \omega'}{c n_{eff}(\omega') A_{eff}^{1/4}(\omega')} \end{aligned} \tag{2.18}$$

We can write the GNLSE as

$$\frac{\partial \tilde{A}'}{\partial z} = i\bar{\gamma}\left(\omega'\right)\exp(-\hat{L}z)FT\left\{\bar{A}(z,T)\int_{-\infty}^{\infty} R(T')\left|\bar{A}(z,T-T')\right|^2 dT'\right\} \tag{2.19}$$

The A_{eff} can be fitted from measured values and incorporated in this equation, as well as the Raman response as estimated in (2.4). The resulting differential equation can then be solved using numerical integration methods, a few of which are available packaged in Matlab. Frequency-domain integration of the GNLSE was the method employed for calculations in Chapter 5 of this dissertation, and was written following the code provided in Chapter 3 of Ref. [2].

2.1.3 Conditions for Soliton Propagation

If we consider fiber propagation as governed by the GNLSE, but ignoring all linear and nonlinear effects except the group velocity dispersion (GVD) and the self-phase modulation (SPM), the GNLSE in (2.7) reduces to the familiar nonlinear Schrödinger equation (NLSE):

$$\frac{\partial A}{\partial z} + \frac{i\beta_2}{2}\frac{\partial^2 A}{\partial T^2} = i\gamma A\left|A\right|^2 \tag{2.20}$$

The equation is written in normalized units using

$$\begin{aligned} U &= \frac{A}{\sqrt{P_0}} \\ \xi &= \frac{z}{L_D} \\ \tau &= \frac{T}{T_0} \end{aligned} \tag{2.21}$$

Where P_0 is the peak power and T_0 is the pulsewidth. Dispersion length is defined as $L_D = T_0^2/|\beta_2|$, and nonlinear length $L_{NL} = 1/(\gamma P_0)$. The parameter N is defined as $N^2 = L_D/L_{NL}$, and is the soliton order. The NLSE in (2.20) can now be written as

$$\frac{\partial U}{\partial \xi} + i\frac{\mathrm{sgn}(\beta_2)}{2}\frac{\partial^2 U}{\partial \tau^2} = iN^2 U|U|^2 \tag{2.22}$$

Making the substitution $u = NU$ and rearranging the equation:

$$i\frac{\partial u}{\partial \xi} - \frac{\mathrm{sgn}(\beta_2)}{2}\frac{\partial^2 u}{\partial \tau^2} + u|u|^2 = 0 \tag{2.23}$$

A solution of this equation is the fundamental soliton ($N = 1$), which has the form

$$u = \mathrm{sech}(\tau)\exp(i\xi/2) \tag{2.24}$$

Its peak power we can obtain at by solving for P_0 for $N = 1$.

$$P_0 = \frac{cA_{eff}|\beta_2|}{n_2\omega_0 T_0^2} = \frac{\lambda A_{eff}|\beta_2|}{2\pi n_2 T_0^2} \tag{2.25}$$

The linear phase induced by GVD is

$$d\phi_L = -\frac{\mathrm{sgn}(\beta_2)}{2u}\frac{\partial^2 u}{\partial \tau^2}d\xi \tag{2.26}$$

And the nonlinear phase induced by SPM is

$$d\phi_{NL} = |u|^2 d\xi \tag{2.27}$$

The sum of the linear and nonlinear phase is then

$$d\phi_L + d\phi_{NL} = -\mathrm{sgn}(\beta_2)\left(\frac{1}{2} - \mathrm{sech}^2(\tau)\right)d\xi + \mathrm{sech}^2(\tau)d\xi \tag{2.28}$$

When β_2 is negative, the sum of the linear and nonlinear phase is a constant (1/2), meaning no phase distortion across the pulse is induced during propagation and the pulse travels unperturbed in the fiber. Here we see two requirements for soliton propagation: anomalous dispersion ($\beta_2 < 0$, or $D > 0$), and sufficient peak power (the launch requirement for a fundamental soliton, P_0).

2.2 Specialty Fibers and Fiber Dispersion[1]

As was outlined in the preceding description of the fundamental soliton solution to the NLSE, anomalous dispersion is a prerequisite for soliton propagation. This section will discuss the dispersive properties of three types of fibers: standard single-mode fiber (SMF), microstructured optical fibers, and HOM fibers. Furthermore, I will use the characteristic power for soliton propagation (defined as the peak power of a fundamental soliton $P_0 = \lambda A_{eff} \left|\beta_2\right| / 2\pi n_2 T_0^2 \propto A_{eff} \left|D\right| / n_2 T_0^2$) to comment on the pulse energies attainable with the various fiber types.

The total dispersion of a fiber is the sum of material dispersion, D_m, and waveguide dispersion, D_w. Since the waveguide dispersion of the fundamental (LP_{01}) mode in standard SMF is normal ($D_w < 0$), soliton propagation is largely limited by the region of anomalous material dispersion in silica, $\lambda > 1.3$ μm. We can understand this by considering the mode evolution of the LP_{01} mode. As wavelength increases, the LP_{01} mode monotonically transitions from the high-index central core to the surrounding lower index regions, yielding a smaller effective mode index. Thus, the group velocity, which scales inversely as the group index, decreases with increasing wavelength. Waveguide dispersion, related to the group velocity by $D_w = d\left(1/v_g\right)/d\lambda$, is therefore negative.

Newer fiber designs that exhibit different mode propagation characteristics allow for positive waveguide dispersion values. Positive waveguide dispersion larger than the magnitude of negative material dispersion can then achieve anomalous dispersion at previously unattainable wavelengths. In addition, these newer fiber platforms can be engineered to have different dispersion profiles by dimensional scaling or tuning of index parameters. We can divide the microstructured optical fibers

[1] The contents of this section have been reproduced in part from *Journal of Selected Topics in Quantum Electronics*, **14**, 713 (2008)

discussed here into two main groups: index-guided photonic crystal fibers and hollow-core photonic bandgap fibers. We will use PCF to refer to the index-guided structures and PBGF to refer to the hollow-core structures. Fig. 2.1(a) and (b) show typical PCF and PBGF structures.

Light in high-index core PCFs is index-guided (total-internal reflection), as with conventional solid-silica step-index SMF. Due to the high index contrast between the silica core and air-hole clad, the PCF can be thought of as a thin silica strand in air. Such a structure can have large anomalous dispersion over the wavelength regions where silica has normal material dispersion [5]. In addition, the photonic crystal lattice that forms the cladding can be designed to give a wide range of dispersion profiles [6]. The small core size and thus small A_{eff} of PCF enable observation of nonlinear effects at low pulse energies ($P_0 \sim A_{eff}$).

PBGFs, on the other hand, with its low-index core, does not guide with total-internal reflection. Instead, it guides light by the bandgap effect created by the periodic lattice that surrounds the central defect [7]. As with PCFs, the dispersion of PBGFs can be engineered by appropriate design of the photonic crystal lattice cladding. The appeal of PBGF lies in its hollow core: the low nonlinearity of the propagation medium enables high energy ($P_0 \sim 1/n_2$) pulse delivery [8].

HOM fiber, in contrast with microstructured optical fibers, has large A_{eff} and moderate nonlinearity (both comparable to conventional SMF), and shows promise for supporting solitons of pulse energies 1-10 nJ. Such an exciting new fiber type was recently demonstrated that yields strong anomalous dispersion in the 1-μm wavelength range [9]. This all-solid silica fiber structure is index-guided as with SMF. This represents a major breakthrough in fiber design because it was previously considered impossible to obtain anomalous dispersion at wavelength shorter than 1.3 μm in such

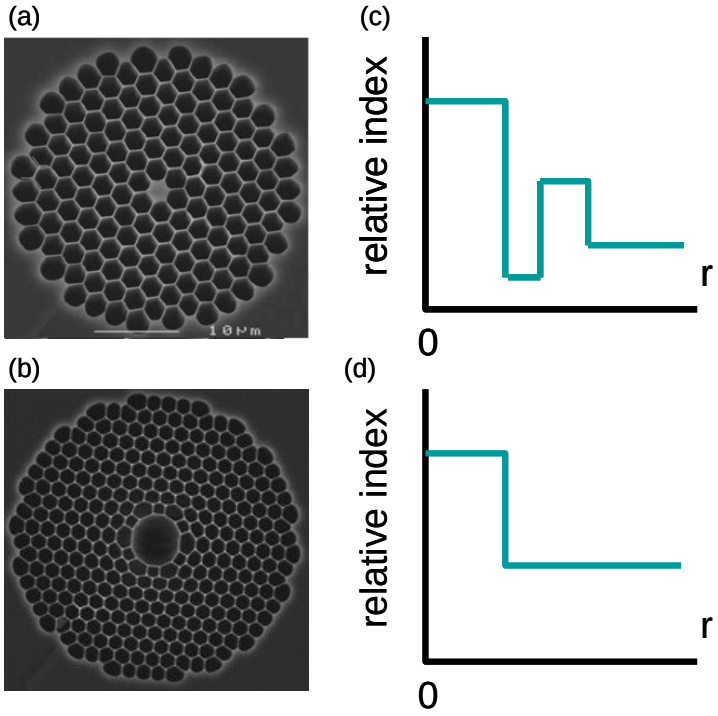

Figure 2.1 (a) SEM image of a PCF, (b) SEM image of a PBGF, (c) radial index profile of an HOM fiber, (d) index profile of a conventional step-index fiber. Index profiles not to scale. Images in (a) and (b) courtesy of Thorlabs and Crystal Fibre.

an all-solid silica fiber. The key to the design was the ability to achieve strong positive (anomalous) D_w for the LP_{02} mode (a higher-order mode) of a specially designed HOM fiber. Combined with in-fiber gratings, this enabled constructing an anomalous dispersion element with low loss (~ 1%) and A_{eff} of ~40-70 μm^2.

In contrast to the normal waveguide dispersion of the LP_{01} mode, the LP_{02} mode can exhibit anomalous waveguide dispersion. The LP_{02} mode, instead of transitioning to the lower index cladding with increasing wavelength, can be designed to have the opposite mode evolution: as the wavelength increases, the mode transitions from the lower index regions to the higher index core. Following the same analysis as we did previously when considering the dispersion of the LP_{01} mode, but now with an effective modal index that increases with increasing wavelength, we conclude that D_w is positive (anomalous) for the LP_{02} mode.

In fact, very large positive values of D_w can be obtained, vastly exceeding the magnitude of (negative) D_m. This yields a mode with positive total D (anomalous dispersion). Note that this evolution is governed by the various high index regions of the waveguide which can be modified to achieve a variety of dispersion magnitudes, slopes and bandwidths. Sample index profile for an HOM fiber shown in Fig. 2.1 (c), in contrast with the top-hat index profile of conventional SMF in Fig. 2.1 (d). The design flexibility with the index contrast and size of core and cladding rings yields a recipe to obtain positive dispersion in a variety of wavelength ranges. In fact, the enormously successful commercial dispersion compensation fiber was designed to achieve a variety of dispersion values based on the same concept [9, 10]. The HOM fibers investigated in the following chapters are designed to achieve anomalous dispersion in the near infrared, with maximum D between 50 and 80 ps/nm/km, and A_{eff} on the order of 50 μm^2.

REFERENCES

1. G. P. Agrawal, *Nonlinear Fiber Optics*, San Diego, California: Academic Press, 2001.

2. J. M. Dudley and J. R. Taylor, *Supercontinuum Generation in Optical Fibers*, New York: Cambridge University Press, 2010.

3. K. J. Blow and D. Wood, "Theoretical description of transient stimulated Raman scattering in optical fibers," *IEEE Journal of Quantum Electronics*, vol. 25, pp. 2665-2673, 1989.

4. J. P. Gordon, "Theory of the soliton self-frequency shift," *Optics Letters*, vol. 11, pp. 662-664, 1986.

5. J. C. Knight, J. Arriaga, T. A. Birks, A. Ortigosa-Blanch, W. J. Wadsworth and P. S. Russell, "Anomalous dispersion in photonic crystal fiber," *IEEE Photonics Technology Letters*, vol. 12, pp. 807-809, 2000.

6. J. C. Knight, "Photonic crystal fibres," *Nature*, vol. 424, pp. 847-851, 2003.

7. R. F. Cregan, B. J. Mangan, J. C. Knight, T. A. Birks, P. S. Russell, P. J. Roberts and D. C. Allan, "Single-mode photonic band gap guidance of light in air," *Science*, vol. 285, pp. 1537-1539, 1999.

8. D. G. Ouzounov, F. R. Ahmad, D. Muller, N. Venkataraman, M. T. Gallagher, M. G. Thomas, J. Silcox, K. W. Koch and A. L. Gaeta, "Generation of megawatt optical solitons in hollow-core photonic band-gap fibers," *Science*, vol. 301, pp. 1702-1704, 2003.

9. S. Ramachandran, S. Ghalmi, J. W. Nicholson, M. F. Yan, P. Wisk, E. Monberg and F. V. Dimarcello, "Anomalous dispersion in a solid, silica-based fiber," *Optics Letters*, vol. 31, pp. 2532-2534, 2006.

10. L. Gruner-Nielsen, M. Wandel, P. Kristensen, C. Jørgensen, L. V. Jørgensen, B. Edvold, B. Pálsdóttir and D. Jakobsen, "Dispersion-compensating fibers," *Journal of Lightwave Technology*, vol. 23, pp. 3566, 2005.

CHAPTER 3

SOLITON SELF-FREQUENCY SHIFT IN HIGHER ORDER MODE FIBER[2]

3.1 Introduction

A soliton is a wave packet whose temporal profile does not change with propagation. In the early 1970s, Zakharov and Shabat [1] and Hasegawa and Tappert [2] showed theoretically that these solitonic solutions exist for propagation in dielectric fiber. Soon after, Satsuma and Yajima added to the understanding by presenting higher-order soliton solutions [3]. The first experimental observation of a fiber-bound optical soliton was in 1980 [4]. Mollenauer *et al.* observed that pulses from a mode-locked laser coupled into a low-loss single-mode fiber (SMF) exhibited dispersive broadening at low power. Then at higher powers, they observed the fundamental and higher order solitons predicted in [1-3].

The soliton is a solution of the nonlinear Schrodinger equation (NLSE), which governs light propagation. In the regime where the equation cannot be approximated by solely dispersive or nonlinear propagation, the soliton solution exists due to the interplay of group velocity dispersion (GVD) and self-phase modulation (SPM). In a soliton, the linear phase shift caused by GVD is completely cancelled by the nonlinear phase shift caused by SPM, resulting in a pulse that propagates unperturbed down the fiber. To get this phase cancellation, the dispersion must be positive (anomalous). Since its discovery, optical solitons have had widespread impact in optics, in particular to telecommunications and ultrafast science.

[2] The contents of this chapter have been reproduced in part from *Journal of Selected Topics in Quantum Electronics*, **14**, 713 (2008)

Dianov *et al.* reported in 1985 a Raman pumping of the Stokes frequency by a sufficiently powerful input into a single-mode quartz optical fiber [5]. In 1986, Mitschke and Mollenauer reported a increasing red-shift of the center frequency of a subpicosecond soliton pulse with increasing power in standard single-mode, polarization maintaining fiber [6]. They named the phenomenon soliton self-frequency shift (SSFS). Due to Raman gain, the blue portion of the soliton spectrum pumps the red portion of the spectrum, causing a continuous red-shift in the soliton spectrum. This wavelength shift was observed to increase with both input power and fiber length. The mathematical basis of SSFS is described in [7]. Gordon found that the frequency shift per unit length was proportional to T_0^{-4}, T_0 being the pulsewidth. SSFS is not significant for telecom scale (at least tens or hundreds of picoseconds-long) pulses. The long pulsewidth leads to only a fraction of GHz shift over tens of thousands of kilometers. The delay between the discovery of the optical soliton and the observation of the SSFS was primarily because of the lack of a reliable subpicosecond high-power soliton source.

Other early work in SSFS [8-11] showed that for a short pulse at high power (capable of producing N ≈ 10 order soliton), instead of forming a higher-order soliton as expected from [3, 4], fissioned to form numerous fundamental solitons. These fundamental solitons would then individually shift in frequency. Beaud *et al.* [8] observed the formation of multiple Stokes pulses each with the temporal profile of a fundamental soliton. These Stokes pulses underwent frequency shift, resulting in an output spectrum with spectrally separated soliton peaks. The remaining energy not converted to a soliton was dissipated in a dispersive wave at the source wavelength.

Since its discovery in SMF, SSFS has also been observed in other fiber platforms, including tapered microstructured air-silica fiber [12], high-index-core photonic crystal fiber (PCF) [13, 14], hollow-core photonic bandgap fiber (PBGF)

[15], and solid-silica higher order mode (HOM) fiber [16]. The region of anomalous dispersion for silica limits SSFS in standard step-index silica-based fiber to wavelengths longer than 1.3 μm. Microstructured optical fibers and other new fiber designs, on the other hand, have non-conventional mode-propagation characteristics [17, 18], which give rise to fiber dispersion profiles previously unattainable by step-index silica-based fibers. These novel fiber structures have extended the accessible region down to the near IR, and even visible wavelengths [18, 19].

Since the frequency shift from SSFS is deterministic, SSFS has seen much application over the last decade to fabricating fiber-delivered, widely frequency-tunable, femtosecond pulse sources [20, 21]. Other applications of SSFS include analog to digital conversion [22, 23], and telecom applications such as signal processing [24, 25], tunable time delays [26, 27], switching and demultiplexing [28-30].

In this chapter, we will describe SSFS as observed in various fiber platforms, namely SMF, high-index core PCF, hollow-core PBGF, and solid all-silica HOM fiber. In addition, we will review applications of SSFS for making tunable- and multi-wavelength sources, analog to digital conversion, and all-optical tunable delay lines.

3.2 Fiber Structures

SSFS has been observed in many types of fibers. In early experiments in SMF, SSFS has been observed between 1.3 μm and 2 μm. Microstructured optical fibers such as PCF and PBGF have been shown to exhibit SSFS between 0.8 μm and 1.7 μm. Recently, SSFS has also been shown in HOM fibers between 1 μm and 1.3 μm. Each fiber type has unique characteristics of dispersion and nonlinearity, as described in Chapter 2, and the behavior of SSFS in these fiber platforms are dictated by these

properties. Table 3.1 summarizes past representative experiments of SSFS in different fiber platforms.

3.2.1 SSFS in Single Mode Fiber

The first discovery of SSFS was made in polarization maintaining (PM) single mode step-index fiber [5, 6]. Mitschke and Mollenauer [6] observed up to 10 THz shift of an input at 1.5 μm, about 75 nm shift. Since then there have been numerous demonstrations of SSFS in standard PM SMF showing shift over different wavelengths. Beaud *et al.* [8] showed wavelength shift from 1.36 to 1.54 μm, Nishizawa *et al*. showed a redshift up to 2.03 μm [31]. Many other groups have shown SSFS in PM SMF in between these wavelength ranges [20, 32-34]. Other efforts include demonstrations in doped fiber amplifiers [35], highly nonlinear fiber [36], birefringent fiber [37, 38], fiber with length-variable dispersion [39], as well as non-PM fibers [32, 40, 41].

3.2.2 SSFS in Microstructured Optical Fiber

As was described in Chapter 2, microstructured fibers such as index-guided PCFs and hollow-core PBGFs can be engineered to access anomalous dispersion at wavelengths not attainable by conventional solid-silica fibers. This anomalous dispersion access provided by these fiber structures also opens the door to observation of SSFS at these wavelengths. The first demonstration of SSFS in an index-guided microstructured optical fiber was in a tapered PCF by Liu *et al*., showing wavelength shift from 1.3-1.65 μm [12]. Later, Washburn *et al.* [13] as well as Cormack *et al.* [14] demonstrated SSFS in untapered PCF in regions of normal silica dispersion ($\lambda < 1.3$ μm). Since these early demonstrations, groups have shown wavelength shifts within the wavelength range of 0.6-1.7 μm [14, 42-48]. In addition to the demonstrations in

TABLE 3.1
EXAMPLES OF SOLITON SELF-FREQUENCY SHIFT IN FIBER

Fiber	Wavelength Range (μm)	Pulse Energy	Reference
PM SMF	1.36-1.54	0.4 nJ	Beaud 1987
	1.56-2.03	0.2 nJ	Nishizawa 2001
HNLF	1.56-1.72	15 pJ	Chestnut 2003
Doped fiber amplifier	1.55-1.60	~1 nJ	Kim 2002
Birefringent fiber	1.56-1.70	~0.1 nJ	Nishizawa 1999
Non-PM SMF	1.55-1.7	0.4 nJ	Wei, 2004
	1.55-1.83	60 pJ	Korolev 2007
Tm-Ho	1.97-2.15	2 nJ	Kivisto 2007
Tapered PCF	1.3-1.65	1 nJ	Liu 2001
	0.81-1.13	0.1 nJ	Kobtsev 2004
PCF	0.85-1.05	60 pJ	Washburn 2001
	0.8-1.26	~0.4 nJ	Cormack 2002
	0.78-1.0	~50 pJ	Nishizawa 2003
	1.03-1.33	0.5 nJ	Lim 2004
	0.82-1.35	~10 pJ	Ishii 2006
	1.05-1.69	~0.2 nJ	Takayanagi 2006
PBGF	1.47-1.53	~600 nJ	Ouzounov 2003
HOM fiber	1.06-1.20	0.8 nJ	van Howe 2007
	1.06-1.30	1 nJ	Lee 2007

PM: Polarization maintaining, SMF: single mode fiber, PCF: photonic crystal fiber (here refers to index-guiding structures), PBGF: photonic bandgap fiber (here refers to hollow core structures), HOM: higher-order-mode

index-guided PCFs, Ouzounov *et al.* recently demonstrated SSFS in a hollow core PBGF. For propagation in an air-filled PBGF, they observed soliton self-frequency shift of 60 nm from 1.47-1.53 μm [15].

The wavelength access provided by dispersion engineering in these microstructured fibers is exciting; however, each novel fiber design has limitations in allowed pulse energies. The pulse energy required to support stable Raman-shifted solitons in index-guided PCFs and hollow-core PBGFs is either very low, a fraction of a nJ for silica-core PCFs [13, 46], or very high, greater than 100 nJ (requiring an input from an amplified optical system) for hollow-core PBGFs [49]. The low-energy limit is due to high nonlinearity in the PCF. In order to generate large positive waveguide dispersion to overcome the negative dispersion of the material, the effective area of the fiber core must be reduced. For positive total dispersion at wavelengths less than 1.3 μm this corresponds to an A_{eff} of 2-5 μm^2, approximately an order of magnitude less than conventional SMF. The high-energy requirement for PBGF is due to low nonlinearity in the air-core where the n_2 of air is roughly 1000 times less than that of silica. These extreme ends of nonlinearity dictate the required pulse energy (P_0) for fundamental soliton propagation, which scales as $P_0 \propto A_{eff} |D| / n_2 T_0^2$. In fact, most PCF and tapered fibers with positive dispersion are intentionally designed to demonstrate nonlinear optical effects at the lowest possible pulse energy. On the other hand, hollow-core PBGFs are often used for applications that require linear propagation, such as pulse delivery. For these reasons, previous work showing SSFS below 1.3 μm were performed at soliton energies either too low or too high (by at least an order of magnitude) for many practical applications, where wavelength-tunable bulk solid state lasers are currently the mainstay for the excitation source [50].

3.2.3 SSFS in HOM Fiber

HOM fibers achieve anomalous dispersion at wavelengths of normal silica material dispersion by propagating the light in a higher-order mode of the fiber instead of the fundamental mode. Like the microstructured fibers described above, the HOM fiber dispersion is also widely engineerable, while having large A_{eff} (compared to PCF) and moderate nonlinearity (compared to the air-core of PBGF). These attributes enable it to generate solitons in the intermediate pulse energy regime (1-10 nJ) between PCFs and PBGFs. We present here the demonstration of SSFS from 1.06 μm to 1.2 μm with up to 57% power efficiency in a HOM fiber [16]. The HOM fiber used in this experiment had positive dispersion (~60 ps/nm-km) below 1.3 μm and a relatively large effective area [18], approximately ten times that of index-guided PCFs for similar dispersion characteristics. Through soliton shaping and higher-order soliton compression within the HOM fiber, we were able to generate clean 49 fs pulses from 200 fs input pulses. In addition, we also observed red-shifted Cerenkov radiation in the normal dispersion regime for appropriately energetic input pulses. This dispersive wave to which the soliton energy couples efficiently is called Cerenkov radiation in fiber [51-53], in analogy to the Cerenkov radiation generated by a charged particle moving through a dispersive medium. The phenomenon of Cerenkov radiation generation in HOM fiber is discussed further in Chapter 4.

Fig. 3.1(a) shows the dispersion curve for the LP_{02} mode in the HOM fiber used in our experiment. To generate positive dispersion below 1.3 μm while simultaneously maintaining a large effective area, light propagates solely in the LP_{02} mode. A dispersion of 62.8 ps/nm-km at 1.06 μm is comparable to that of microstructured fibers used previously for SSFS [12, 13, 46], and exhibits two zero-dispersion wavelengths (ZDWs) at 908 nm and 1247 nm. The mode profile at the end face of the HOM fiber is shown in Fig. 3.1(b), demonstrating a clean higher-order

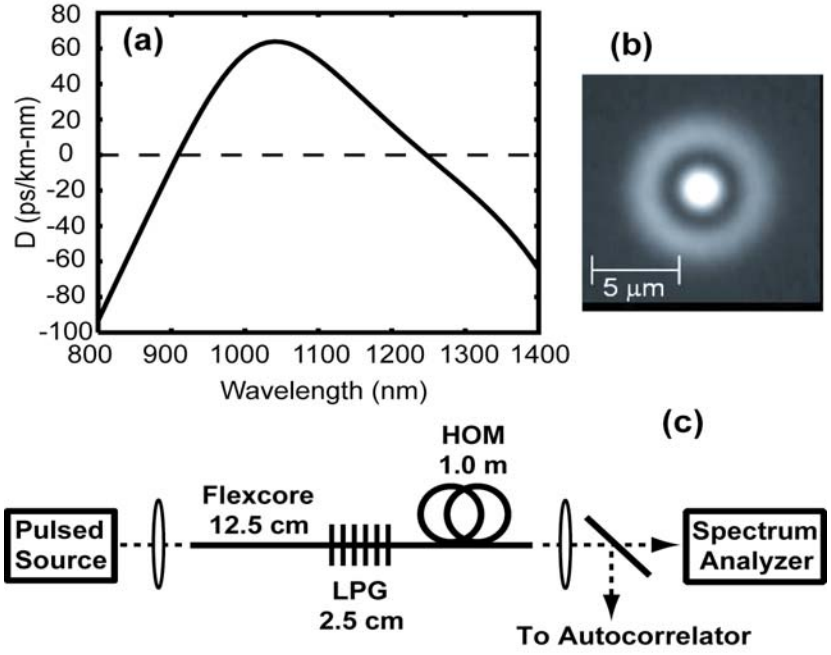

Figure 3.1 (a) Total dispersion for propagation in the LP_{02} mode. (b) Experimental near-field image of the LP_{02} mode with effective area $A_{eff} = 44\ \mu m^2$. (c) Experimental setup used to couple light through the HOM fiber module.

LP_{02} mode and an effective area of 44 μm^2.

The HOM fiber module (Fig. 3.1 (c)) consists of a segment of standard SMF (flexcore), a long period grating (LPG) [54], and 1.0 m of HOM fiber. Light propagates in the fundamental mode in the flexcore pigtail, is coupled to the LP_{02} mode in the LPG (99% mode conversion efficiency), then propagates solely in the higher order mode through the HOM fiber We note that the all-silica HOM fiber leverages the standard silica fiber manufacturing platform and retains the low loss properties (for both transmission and bending) of a conventional SMF, allowing easy termination and splicing.

The experimental setup for observing SSFS in HOM fiber is shown in Fig. 3.1(c). The pump source consisted of a fiber laser (Fianium FP1060-1S) which delivered a free space output of ~200 fs pulses at a center wavelength of 1064 nm and an 80 MHz repetition rate. Using a variable attenuator, the input pulse energy was varied from 1.36 nJ to 1.63 nJ to obtain clean spectrally-shifted solitons with a maximum wavelength shift of 136 nm (12% of the carrier wavelength), Fig. 3.2(a). Theoretical traces from numerical simulation (using the split-step Fourier method) for similar input pulse energy are plotted adjacent to the experimental data in Fig. 3.2(d). The non-PM nature of the higher order mode fiber does not give rise to any observable instability, as observed from the clean spectra of the solitons as well as the agreement with numerical simulation.

We measure 57% power conversion from the input pulse spectrum to the red-shifted soliton for the case of 1.39 nJ input pulses to achieve ~0.8 nJ output soliton pulses, Fig. 3.2(a). The corresponding second-order interferometric autocorrelation (Fig. 3.3) gives an output pulse width of 49 fs, assuming a $sech^2$ pulse shape, showing a factor of four in pulse width reduction due to higher-order soliton compression

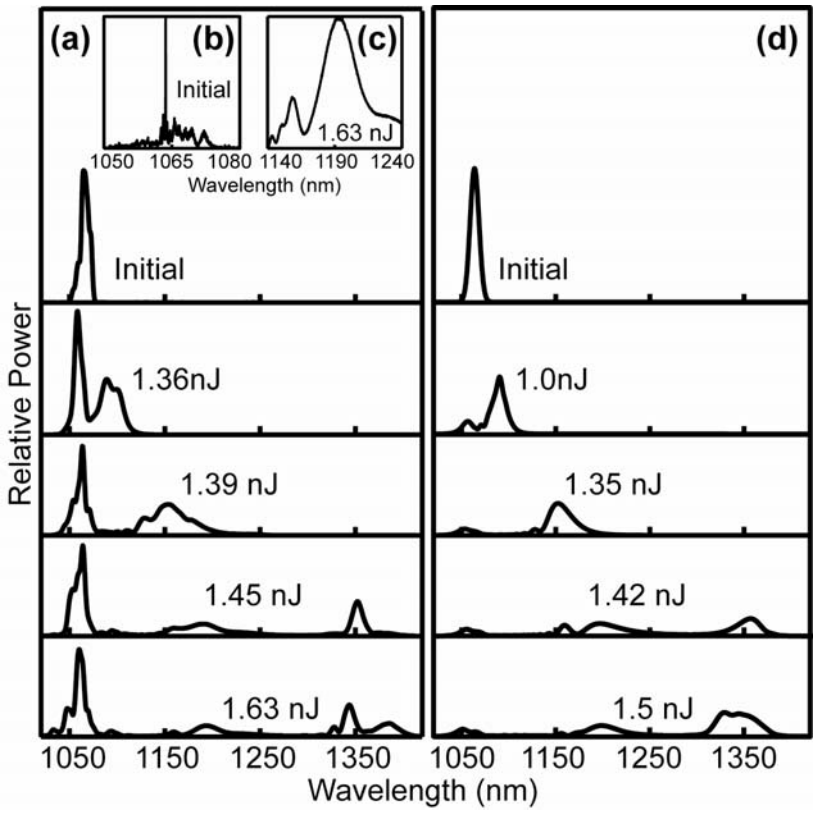

Figure 3.2 (a) Soliton self-frequency shifted spectra corresponding to different input pulse energies into the HOM fiber. All traces taken at 4.0 nm resolution bandwidth (RBW). Input pulse energy noted on each trace. Power conversion efficiency is 57 % for 1.39 nJ input. (b) High resolution trace of the initial spectrum; 0.1 nm RBW. (c) High resolution trace of the shifted soliton for 1.63 nJ input into the HOM fiber; 0.1 nm RBW. (d) Soliton self-frequency shifted spectra calculated from simulation using a 200 fs input Gaussian pulse and shifted soliton energies comparable to those in (a). Input pulse energy noted on each trace.

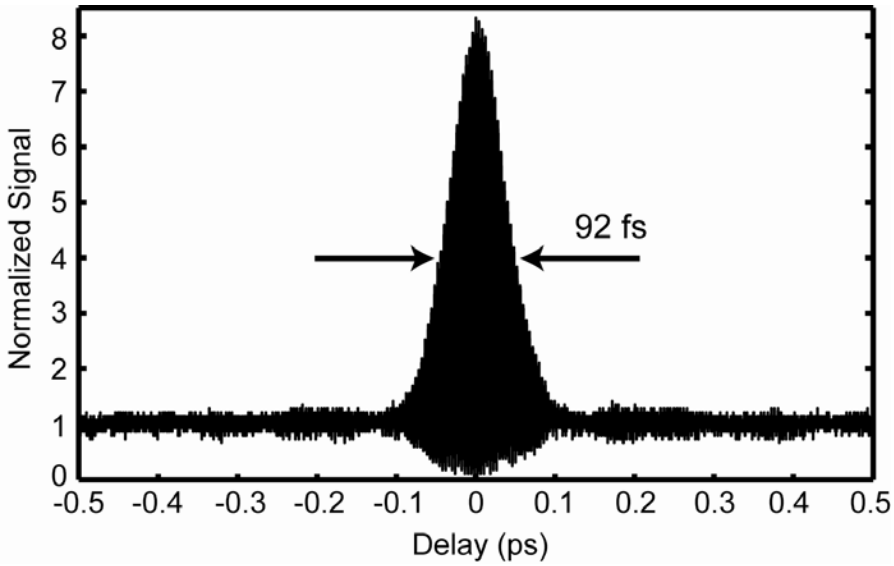

Figure 3.3. Second-order interferometric autocorrelation trace of HOM output for 1.39 nJ input pulses. Autocorrelation FWHM measured to be 92 fs corresponding to a deconvolved pulse width of 49 fs.

(soliton order $N = 2.1$) in the HOM fiber. The measured spectral bandwidth of 35 nm gives a time-bandwidth product of 0.386 which is 23% beyond that expected for a sech^2 pulse shape. We further note the ripple-free, high-resolution spectrum of the shifted soliton at 1.63 nJ input, Fig. 3.2(c), indicative of single mode propagation in the LP_{02} mode.

Though not demonstrated in our experiments, light can be easily coupled back into the fundamental mode using another LPG at the output end. Previous work showed that by using a dispersion-matching design, ultra-large bandwidths can be supported by a LPG [54]. Recently conversion efficiency of 90% over a bandwidth of 200 nm was obtained for a similar fiber structure [55]. Such a LPG will ensure the output pulse is always converted back to a Gaussian profile, within the tuning range. On the other hand, depending on the intended usage, the higher order mode output could also be used directly without mode conversion. The focusing properties of the LP_{02} mode for nonlinear microscopy applications are discussed in Chapter 6.

3.2.4 Extended Soliton Shift in HOM Fiber with Dispersion Engineering[3]

One can imagine that an HOM fiber module could be engineered to produce shifted solitons of different wavelengths and pulse energies with a different dispersion design. For example, simple dimensional scaling of the index profile can be used to shift the dispersion curve of the LP_{02} mode. Our numerical modeling shows that output soliton energy of approximately 2 nJ can be realized if the dispersion curve is shifted ~ 100 nm to the longer wavelength side. Additionally, pulse energy can be scaled by increasing D or A_{eff}. Aside from increasing the magnitude of dispersion through manipulation of the index profile and dimensions of the fiber, the effective area can be significantly enhanced by coupling into even higher-order modes. An

[3] The contents of this section have been reproduced in part from OFC/NFOEC 2007, PDP38.

effective area of ~2000 μm^2 (more than 40 times this HOM fiber) was recently achieved by coupling to the LP_{07} mode [55].

Indeed, we obtained much improved SSFS performance by dispersion engineering of the HOM fiber. The dispersion is changed by simple dimensional scaling in this case, yielding a dispersion curve with ZDWs separated by 415 nm. We demonstrated SSFS below 1.3 μm over a 240 nm range (100 nm more than in 3.2.3). The shifted spectra from Section 3.2.3 and the HOM fiber under study here are shown side by side in Fig. 3.4. With measured soliton energies above 1.0 nJ, Fig. 3.4 represents the largest wavelength shift of energetic pulses in the technologically important, but hard-to-access range of 1-1.3 μm.

The experimental setup for observing extended SSFS in HOM fiber was the same as described in Section 3.2.3, but now the HOM fiber module consisted of a 13.5 cm standard single mode (Flexcore) pigtail, a long period grating (LPG) mode converter, and 2.4 m of HOM fiber. The LP_{02} mode in this HOM fiber had a large effective mode field area of 70 μm^2 at 1064 nm.

The dependence of soliton shift on input power is shown in Fig. 3.5. With increasing input pulse energy, we observed soliton fission and redshift of the fissioned soliton. As the input energy was increased beyond 2.9 nJ, the center wavelength of the soliton shifted to 1300 nm, nearly 240 nm away from the input pulse. Further increasing the input pulse energy did not increase the range of the soliton shift because of the ZDW of the HOM located at 1368 nm. We also observed a Cerenkov radiation band appearing in the normal dispersion regime, centered at 1480 nm. Further increasing the input pulse energy pumped energy into the Cerenkov radiation in lieu of further shifting the soliton.

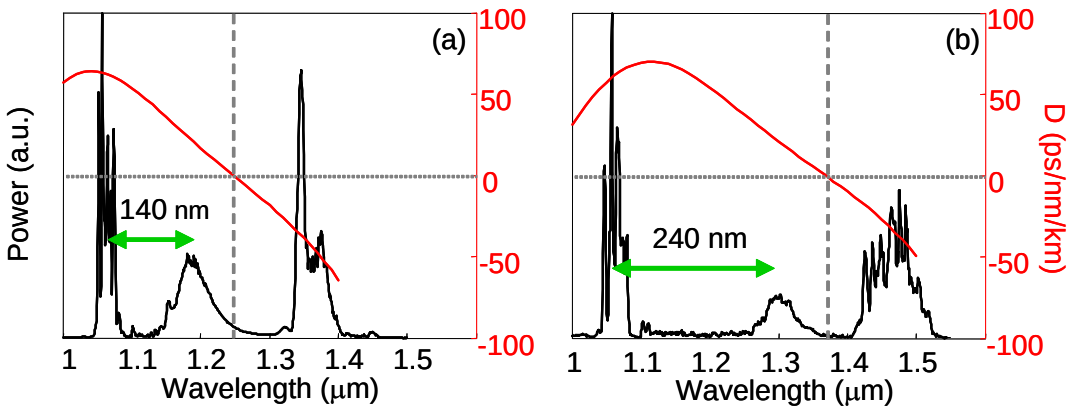

Figure 3.4. Spectrum showing SSFS in HOM fiber overlaid with dispersion curves, (a) initial demonstration (as described in 3.2.3), (b) dispersion shifted design. Zero dispersion wavelength is marked with a dashed line. Residual input is attenuated by 7 dB in both plots to accentuate the wavelength shifted features.

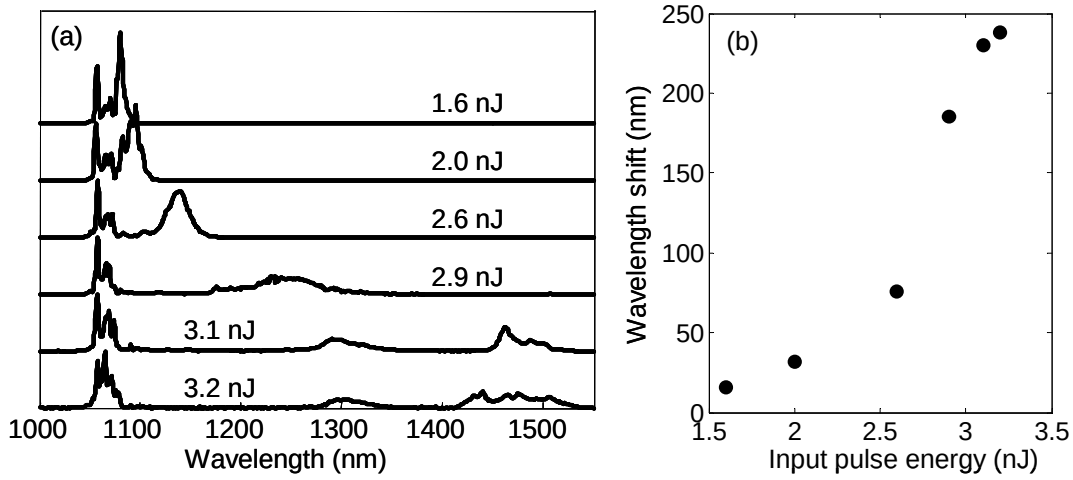

Figure 3.5. (a) Measured spectra for different input pulse energies as indicated next to each trace. Residual input is attenuated by 7 dB to accentuate the wavelength shifted features. (b) Soliton wavelength shift (from 1064 nm) as a function of input pulse energy.

We measured the autocorrelation of a shifted soliton centered at 1125 nm. The second-order interferometric autocorrelation is shown in Fig. 3.6. The intensity autocorrelation full width half-max (FWHM) was 140 fs, and assuming a sech^2 shape, gave a deconvolved pulsewidth of 91 fs. Soliton energy was measured to be 1.05 nJ, the highest energy level ever achieved by SSFS in a solid core fiber at below 1300 nm. We note that solitons with a larger wavelength shift have larger bandwidth and would result in a shorter pulsewidth and higher pulse energy. We note that at maximum coupled power, the HOM fiber can be cut to the appropriate length for maximal soliton energy, i.e. just before the appearance of Cerenkov radiation.

In this section, we demonstrated SSFS from 1064 nm to 1300 nm in a solid silica HOM fiber. A shifted soliton of 1.05 nJ pulse energy and 91 fs pulsewidth was measured. The large range of wavelength tunability combined with high pulse energies make this the first practical all-fiber tunable source with performance approaching that of an optical parametric oscillator (OPO) pumped by a modelocked Ti:Sapphire laser.

3.3 Applications of SSFS

Using its power-dependent wavelength tuning property, SSFS can be straightforwardly used to provide a widely tunable laser source at different wavelength ranges from a fixed-wavelength input. Nishizawa and Goto demonstrated a compact tunable source over 1.56-1.78 μm by simply varying the input power into the shifting fiber [20]. Other tunable sources employing SSFS have been shown for wavelengths ranging 0.8 μm up to 2 μm (see Table 3.1). In addition to wavelength tuning by varying input power, it has also been shown that wavelength tuning can be achieved by changing the input polarization to a highly birefringent fiber exhibiting SSFS [38]. The birefringence also introduces an additional degree of freedom, which can be used

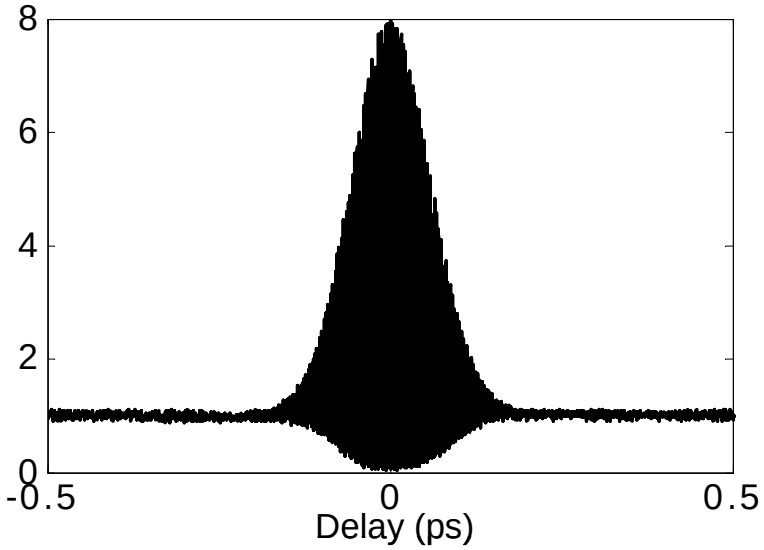

Figure 3.6. Second-order interferometric autocorrelation shows 140 fs intensity FWHM, a 91 fs pulse assuming a sech^2 shape.

in making multi-wavelength sources [37, 56].

SSFS demonstrations in HOM fiber, described in preceding sections, showed wavelength tuning range and pulse energies that could be invaluable for developing an all-fiber, energetic, wavelength-tunable source for a variety of practical applications. For example, the tunable wavelength range of 1-1.3 μm and pulse energy of a few nJ are of great interest for multiphoton imaging. SSFS in fiber, along with a fixed-wavelength fiber laser, could be easily integrated into a fiber endoscopy system with turnkey operation.

In addition to laser wavelength tuning, SSFS has also been employed to realize high-speed analog-to-digital conversion. The main advantage of photonic analog-to-digital converters (ADCs) over electronic ADCs is the ultrastable sampling provided by optical pulses. Konishi *et al.* proposed to use the power-dependent frequency shift property of SSFS to realize photonic ADC [22]. Recently, Nishitani, Konishi, and Itoh demonstrated a 4-bit photonic ADC by using SSFS in combination of SPM-induced spectral compression [57]. Additionally, Xu and Liu [23] proposed a method to significantly reduce the optical complexity associated with the SSFS-based photonic ADC by employing passive splitters and wavelength interleaving filters.

A third application of SSFS is to optical buffering and tunable delays. An all-optical tunable delay line consisting of intensity-dependent delay based on SSFS and supercontinuum generation and filtering was recently proposed [27] and demonstrated [58]. By using the chromatic dispersion of a fiber and the wavelength tunability supplied by SSFS, a tunable delay of up to 720 ps for a 0.45 ps pulse (corresponding to a delay-to-pulse-width ratio of 1600) was achieved. Tuning of the delay was achieved by varying the input peak power to the soliton-shifting fiber. The light was reconverted to the input wavelength via supercontinuum generation and spectral filtering after the delay stage.

3.4 Summary and Outlook

We have reviewed the fundamentals of SSFS, various state-of-the-art fiber platforms for SSFS, and recent experimental SSFS demonstrations. We presented in detail the demonstrations of SSFS in HOM fibers, and its tunability via dispersion engineering. Several interesting applications of SSFS, such as wavelength-tunable laser sources, ADC, and tunable delays, were briefly discussed.

The recent experimental demonstration of SSFS from 1.06 nm to 1.3 μm in a HOM fiber indicated the possibility for significantly increased wavelength shift with dispersion engineering. The record magnitude of wavelength shift at pulse energies greater than 1 nJ make this the first practical demonstration of an all-fiber tunable source that approaches the performance of state-of-the-art bulk OPOs. Even larger wavelength shifts and higher pulse energies are expected by using further improved HOM fiber structures that enable both large dispersion and large fiber effective area. Using SSFS in HOM fiber shows great promise for developing a new approach for an all-fiber, compact, energetic, and wavelength-tunable femtosecond source.

REFERENCES

1. V. E. Zakharov and A. B. Shabat, "Exact Theory of 2-Dimensional Self-Focusing and One-Dimensional Self-Modulation of Waves in Nonlinear Media," *Soviet Physics JETP-USSR*, vol. 34, pp. 62-&, 1972.

2. A. Hasegawa and F. Tappert, "Transmission of Stationary Nonlinear Optical Pulses in Dispersive Dielectric Fibers .1. Anomalous Dispersion," *Applied Physics Letters*, vol. 23, pp. 142-144, 1973.

3. J. Satsuma and N. Yajima, "Initial Value-Problems of One-Dimensional Self-Modulation of Nonlinear-Waves in Dispersive Media," *Supplement of the Progress of Theoretical Physics*, vol. pp. 284-306, 1974.

4. L. F. Mollenauer, R. H. Stolen and J. P. Gordon, "Experimental-Observation of Picosecond Pulse Narrowing and Solitons in Optical Fibers," *Physical Review Letters*, vol. 45, pp. 1095-1098, 1980.

5. E. M. Dianov, A. Y. Karasik, P. V. Mamyshev, A. M. Prokhorov, V. N. Serkin, M. F. Stelmakh and A. A. Fomichev, "Stimulated-Raman Conversion of Multisoliton Pulses in Quartz Optical Fibers," *JETP Letters*, vol. 41, pp. 294-297, 1985.

6. F. M. Mitschke and L. F. Mollenauer, "Discovery of the soliton self-frequency shift," *Optics Letters*, vol. 11, pp. 659-661, 1986.

7. J. P. Gordon, "Theory of the soliton self-frequency shift," *Optics Letters*, vol. 11, pp. 662-664, 1986.

8. P. Beaud, W. Hodel, B. Zysset and H. Weber, "Ultrashort pulse propagation, pulse breakup, and fundamental soliton formation in a single-mode optical fiber," *IEEE Journal of Quantum Electronics*, vol. 23, pp. 1938-1946, 1987.

9. W. Hodel and H. P. Weber, "Decay of femtosecond higher-order solitons in an optical fiber induced by Raman self-pumping," *Optics Letters*, vol. 12, pp. 924-926, 1987.

10. Y. Kodama and A. Hasegawa, "Nonlinear pulse propagation in a monomode dielectric guide," *IEEE Journal of Quantum Electronics*, vol. 23, pp. 510-524, 1987.

11. K. Tai, A. Hasegawa and N. Bekki, "Fission of optical solitons induced by stimulated Raman effect," *Optics Letters*, vol. 13, pp. 392-394, 1988.

12. X. Liu, C. Xu, W. H. Knox, J. K. Chandalia, B. J. Eggleton, S. G. Kosinski and R. S. Windler, "Soliton self-frequency shift in a short tapered air-silica microstructure fiber," *Optics Letters*, vol. 26, pp. 358-360, 2001.

13. B. R. Washburn, S. E. Ralph, P. A. Lacourt, J. M. Dudley, W. T. Rhodes, R. S. Windeler and S. Coen, "Tunable near-infrared femtosecond soliton generation in photonic crystal fibres," *Electronics Letters*, vol. 37, pp. 1510-1512, 2001.

14. I. G. Cormack, D. T. Reid, W. J. Wadsworth, J. C. Knight and P. S. J. Russell, "Observation of soliton self-frequency shift in photonic crystal fibre," *Electronics Letters*, vol. 38, pp. 167-169, 2002.

15. D. G. Ouzounov, F. R. Ahmad, D. Muller, N. Venkataraman, M. T. Gallagher, M. G. Thomas, J. Silcox, K. W. Koch and A. L. Gaeta, "Generation of megawatt optical solitons in hollow-core photonic band-gap fibers," *Science*, vol. 301, pp. 1702-1704, 2003.

16. J. van Howe, J. H. Lee, S. Zhou, F. Wise, C. Xu, S. Ramachandran, S. Ghalmi and M. F. Yan, "Demonstration of soliton self-frequency shift below 1300 nm in higher-order mode, solid silica-based fiber," *Optics Letters*, vol. 32, pp. 340-342, 2007.

17. J. C. Knight, "Photonic crystal fibres," *Nature*, vol. 424, pp. 847-851, 2003.

18. S. Ramachandran, S. Ghalmi, J. W. Nicholson, M. F. Yan, P. Wisk, E. Monberg and F. V. Dimarcello, "Anomalous dispersion in a solid, silica-based fiber," *Optics Letters*, vol. 31, pp. 2532-2534, 2006.

19. J. C. Knight, J. Arriaga, T. A. Birks, A. Ortigosa-Blanch, W. J. Wadsworth and P. S. Russell, "Anomalous dispersion in photonic crystal fiber," *IEEE Photonics Technology Letters*, vol. 12, pp. 807-809, 2000.

20. N. Nishizawa and T. Goto, "Compact system of wavelength-tunable femtosecond soliton pulse generation using optical fibers," *IEEE Photonics Technology Letters*, vol. 11, pp. 325-327, 1999.

21. M. E. Fermann, A. Galvanauskas, M. L. Stock, K. K. Wong, D. Harter and L. Goldberg, "Ultrawide tunable Er soliton fiber laser amplified in Yb-doped fiber," *Optics Letters*, vol. 24, pp. 1428-1430, 1999.

22. T. Konishi, K. Tanimura, K. Asano, Y. Oshita and Y. Ichioka, "All-optical analog-to-digital converter by use of self-frequency shifting in fiber and a pulse-shaping technique," *Journal of the Optical Society of America B*, vol. 19, pp. 2817-2823, 2002.

23. C. Xu and X. Liu, "Photonic analog-to-digital converter using soliton self-frequency shift and interleaving spectral filters," *Optics Letters*, vol. 28, pp. 986-988, 2003.

24. J. K. Lucek and K. Smith, "All-Optical Signal Regenerator," *Optics Letters*, vol. 18, pp. 1226-1228, 1993.

25. M. Kato, K. Fujiura and T. Kurihara, "Asynchronous all-optical bit-by-bit self-signal recognition and demultiplexing from overlapped signals achieved by self-frequency shift of Raman soliton," *Electronics Letters*, vol. 40, pp. 381-382, 2004.

26. T. Hori, N. Nishizawa, M. Yoshida and T. Goto, "Cross-correlation measurement without mechanical delay scanning using electronically controlled wavelength-tunable femtosecond soliton pulse," *Electronics Letters*, vol. 37, pp. 1077-1078, 2001.

27. S. Oda and A. Maruta, "All-optical tunable delay line based on soliton self-frequency shift and filtering broadened spectrum due to self-phase modulation," *Opt. Express*, vol. 14, pp. 7895-7902, 2006.

28. A. N. Starodumov, "Nonlinear Soliton Pulse Switching Caused by Raman Self-Frequency Shift," *Kvantovaya Elektronika*, vol. 20, pp. 500-502, 1993.

29. H. HatamiHanza, J. Hong, A. Atieh, P. Myslinski and J. Chrostowski, "Demonstration of all-optical demultiplexing of a multilevel soliton signal employing soliton decomposition and self-frequency shift," *Ieee Photonics Technology Letters*, vol. 9, pp. 833-835, 1997.

30. N. Nishizawa and T. Goto, "Ultrafast all optical switching by use of pulse trapping across zero-dispersion wavelength," *Optics Express*, vol. 11, pp. 359-365, 2003.

31. N. Nishizawa and T. Goto, "Widely wavelength-tunable ultrashort pulse generation using polarization maintaining optical fibers," *IEEE Journal of Selected Topics in Quantum Electronics*, vol. 7, pp. 518-524, 2001.

32. J. K. Lucek and K. J. Blow, "Soliton Self-Frequency Shift in Telecommunications Fiber," *Physical Review A*, vol. 45, pp. 6666-6674, 1992.

33. A. S. Gouveianeto, "Modulation Instability and Soliton-Raman Generation in P_2O_5 Doped Silica Fiber," *Journal of Lightwave Technology*, vol. 10, pp. 1536-1539, 1992.

34. N. Nishizawa, R. Okamura and T. Goto, "Widely wavelength tunable ultrashort soliton pulse and anti-Stokes pulse generation for wavelengths of 1.32-1.75 μm," *Japanese Journal of Applied Physics Part 2*, vol. 39, pp. L409-L411, 2000.

35. D. H. Kim, J. U. Kang and J. B. Khurgin, "Cascaded Raman self-frequency shifted soliton generation in an Er/Yb-doped fiber amplifier," *Applied Physics Letters*, vol. 81, pp. 2695-2697, 2002.

36. D. A. Chestnut and J. R. Taylor, "Soliton self-frequency shift in highly nonlinear fiber with extension by external Raman pumping," *Optics Letters*, vol. 28, pp. 2512-2514, 2003.

37. N. Nishizawa, R. Okamura and T. Goto, "Simultaneous generation of wavelength tunable two-colored femtosecond soliton pulses using optical fibers," *IEEE Photonics Technology Letters*, vol. 11, pp. 421-423, 1999.

38. M. Kato, "Wavelength-tunable multicolor Raman soliton generation using an ellipse polarized pump pulse and highly birefringent optical fibers," *Journal of Lightwave Technology.*, vol. 24, pp. 805-809, 2006.

39. A. V. Andrianov, S. V. Muraviov, A. V. Kim and A. A. Sysoliatin, "Generation of optical soliton pulses smoothly tunable in a wide frequency range in silica fibers with variable dispersion," *JETP Letters*, vol. 85, pp. 364-368, 2007.

40. D. P. Wei, T. V. Galstian, A. Zohrabyan and L. Mouradian, "Tunable femtosecond soliton generation in Ge-doped fibre," *Electronics Letters*, vol. 40, pp. 1329-1330, 2004.

41. A. E. Korolev, D. V. Kuksenkov and V. N. Nazarov, "Controllable self-frequency shift of subpicosecond soliton light pulses in a nonlinear optical fiber," *Optics and Spectroscopy*, vol. 102, pp. 86-89, 2007.

42. N. Nishizawa, Y. Ito and T. Goto, "0.78-0.90-μm wavelength-tunable femtosecond soliton pulse generation using photonic crystal fiber," *IEEE Photonics Technology Letters*, vol. 14, pp. 986-988, 2002.

43. J. H. V. Price, K. Furusawa, T. M. Monro, L. Lefort and D. J. Richardson, "Tunable, femtosecond pulse source operating in the range 1.06-1.33 μm based on an Yb3+-doped holey fiber amplifier," *Journal of the Optical Society of America B*, vol. 19, pp. 1286-1294, 2002.

44. D. T. Reid, I. G. Cormack, W. J. Wadsworth, J. C. Knight and P. S. J. Russell, "Soliton self-frequency shift effects in photonic crystal fibre," *Journal of Modern Optics*, vol. 49, pp. 757-767, 2002.

45. N. Nishizawa, Y. Ito and T. Goto, "Wavelength-tunable femtosecond soliton pulse generation for wavelengths of 0.78-1.0 μm using photonic crystal fibers and a ultrashort fiber laser," *Japanese Journal of Applied Physics Part 1*, vol. 42, pp. 449-452, 2003.

46. H. Lim, J. Buckley, A. Chong and F. W. Wise, "Fibre-based source of femtosecond pulses tunable from 1.0 to 1.3 μm," *Electronics Letters*, vol. 40, pp. 1523-1525, 2004.

47. N. Ishii, C. Y. Teisset, S. Kohler, E. E. Serebryannikov, T. Fuji, T. Metzger, F. Krausz, A. Baltuska and A. M. Zheltikov, "Widely tunable soliton frequency shifting of few-cycle laser pulses," *Physical Review E*, vol. 74, pp. 36617, 2006.

48. J. Takayanagi, T. Sugiura, M. Yoshida and N. Nishizawa, "1.0-1.7-μm wavelength-tunable ultrashort-pulse generation using femtosecond Yb-doped fiber laser and photonic crystal fiber," *IEEE Photonics Technology Letters*, vol. 18, pp. 2284-2286, 2006.

49. F. Luan, J. C. Knight, P. S. Russell, S. Campbell, D. Xiao, D. T. Reid, B. J. Mangan, D. P. Williams and P. J. Roberts, "Femtosecond soliton pulse delivery at 800nm wavelength in hollow-core photonic bandgap fibers," *Optics Express*, vol. 12, pp. 835-840, 2004.

50. A. Diaspro, *Confocal and Two-Photon Microscopy*, New York: Wiley-Liss, 2002.

51. A. G. Bulushev, E. M. Dianov, O. G. Okhotnikov and V. N. Serkin, "Raman Self-Frequency Shift of the Spectrum of Femtosecond Optical Solitons and Suppression of This Effect in Optical Fibers and Soliton Lasers," *JETP Letters.*, vol. 54, pp. 619-622, 1991.

52. N. Akhmediev and M. Karlsson, "Cherenkov radiation emitted by solitons in optical fibers," *Physical Review A*, vol. 51, pp. 2602-2607, 1995.

53. D. V. Skryabin, F. Luan, J. C. Knight and P. S. J. Russell, "Soliton Self-Frequency Shift Cancellation in Photonic Crystal Fibers," *Science*, vol. 301, pp. 1705-1708, 2003.

54. S. Ramachandran, "Dispersion-tailored few-mode fibers: a versatile platform for in-fiber photonic devices," *Journal of Lightwave Technology*, vol. 23, pp. 3426-3443, 2005.

55. S. Ramachandran, J. W. Nicholson, S. Ghalmi, M. F. Yan, P. Wisk, E. Monberg and F. V. Dimarcello, "Light propagation with ultralarge modal areas in optical fibers," *Optics Letters*, vol. 13, pp. 1797-1799, 2006.

56. N. Nishizawa and T. Goto, "Trapped pulse generation by femtosecond soliton pulse in birefringent optical fibers," *Optics Express*, vol. 10, pp. 256-261, 2002.

57. T. Nishitani, T. Konishi and K. Itoh, "Demonstration of 4-bit photonic analog-to-digital conversion employing self-frequency shift and SPM-induced spectral compression," presented at ECOC 2007, Berlin, Germany, 2007, 6.6.3.

58. T. Kunihiro, T. Kanou, S. Oda and A. Maruta, "Soliton self-frequency shift based slow light in optical fiber up to 1600 delay-to-pulse-width ratio," presented at ECOC 2007, Berlin, Germany, 2007, 8.2.2.

CHAPTER 4

GENERATION OF FEMTOSECOND PULSES AT 1350 NM BY CERENKOV RADIATION IN HIGHER ORDER MODE FIBER[4]

4.1 Introduction

Higher order mode (HOM) fiber has attracted significant interest recently due to the freedom it provides to design unique dispersion characteristics in all-solid silica (non-holey) fibers [1]. This new fiber platform allows for anomalous dispersion below 1300 nm by propagating light solely in one of the higher-order modes [1]. Such dispersion characteristics were previously attainable only by photonic crystal fibers (PCF). The unique characteristics of the HOM fiber, such as large anomalous dispersion and a large effective area (approximately ten times that of index-guided PCFs), provide a number of new opportunities for applications in nonlinear fiber optics. For example, we recently demonstrated soliton self-frequency shift (SSFS) below 1300 nm in an HOM fiber. The advantage of using HOM fiber lies in the ability to generate higher energy self-frequency shifted solitons than attainable in microstructured PCFs [2]. Output pulse energy obtainable for cleanly frequency-shifted solitons in index-guided PCFs is limited to fractions of a nanojoule [3, 4] due to light confinement to a smaller effective area, rendering pulses more susceptible to nonlinearity. In contrast, the HOM fiber platform allows advantages of interesting dispersion curves similar to PCFs, yet with a higher tolerance to nonlinearity. The ability to obtain complex dispersive profiles in fiber is interesting because of its prospect for realizing sources in hard-to-access spectral regions by exploiting the

[4] The contents of this chapter reproduced from *Optics Letters*, **32**, 1053, 2007.

generation of Cerenkov radiation [5]: that is, the dispersive waves shed by solitons near the zero-dispersion wavelength (ZDW). HOM fibers, with its higher tolerance to nonlinearities, will allow for energetic sources at wavelengths where fiber-based sources are not currently available.

Cerenkov radiation in fibers has been demonstrated in microstructured fibers pumped near the ZDW as well as experiments generating self-frequency shifted solitons [5-9]. An ideal soliton requires a perfect balance between dispersion and nonlinearity so that energy becomes confined to a discrete packet both spectrally and temporally. With the introduction of perturbations such as higher-order dispersion, this stable solution breaks down, allowing the transfer of energy between the soliton in the anomalous dispersion regime and newly shed dispersive radiation in the normal dispersion regime. Such energy transfer occurs most efficiently in fibers for solitons near the ZDW. The spectral regime to which energy couples most efficiently has been dubbed "Cerenkov radiation" due to an analogous phase matching condition in particle physics. The phenomenon of Cerenkov radiation in fibers is often associated with SSFS as it allows a convenient mechanism for more efficient energy transfer between the soliton and the Cerenkov band. When the third-order dispersion is negative, SSFS will shift the center frequency of the soliton toward the ZDW, resulting in efficient energy transfer into the Cerenkov radiation in the normal dispersion regime. A more rigorous description and analytical derivation of Cerenkov radiation in fibers can be found in various theoretical works [10-12].

In this chapter we show generation of Cerenkov radiation at 1350 nm in an HOM fiber with 20% power conversion efficiency (approximately 25% photon efficiency). We successfully filter and compress the Cerenkov output pulses to 106 fs. Cerenkov radiation generated in the normal dispersion regime of this HOM fiber can be used to extend the wavelength range covered by the shifting soliton, or to create a

three-color pulsed source (centered at the pump, frequency shifted soliton, and Cerenkov radiation wavelengths). This new class of fiber shows great promise for generating femtosecond pulses at various wavelengths in the energy regime of several nJs.

4.2 Experimental Methods

The experimental setup is shown in Fig. 4.1(a). The pump source consists of a pulsed fiber laser (Fianium FP1060-1S) centered at 1064 nm, with 80 MHz repetition rate and 200 fs pulsewidth. We couple the source into the HOM fiber module, which consists of a 12.5 cm standard single mode fiber (flexcore) pigtail, 2.5 cm of long period grating (LPG) and 1 m of HOM fiber. The LPG converts the fundamental mode to the higher-order LP_{02} mode with good (>90%) efficiency over a large (50 nm) bandwidth; for the input wavelength of 1064 nm, 99% of the fundamental mode is converted to the LP_{02} mode, which exhibits anomalous dispersion in the HOM fiber between 908 and 1247 nm [1], see Fig. 4.1(b). At the input wavelength, the LP_{02} mode, shown in Fig. 4.1(c), has an effective area $A_{eff} = 44\ \mu m^2$. The output of the HOM fiber module is collimated and measured with an optical spectrum analyzer and a second order interferometric autocorrelator. A 1300 nm long-pass filter is used to select out the Cerenkov radiation, and a pair of silicon prisms are used for dispersion compensation and to simultaneously filter out any residual pump wavelength. A polarizer and a half-wave plate serve as a variable optical attenuator (VOA) at the input of the HOM fiber module.

We also numerically simulate the system using the split-step Fourier method [13]. The source is modeled as a Gaussian pulse with added self-phase modulation (SPM) to approximately match the source spectrum from the experiment (Fig. 4.2

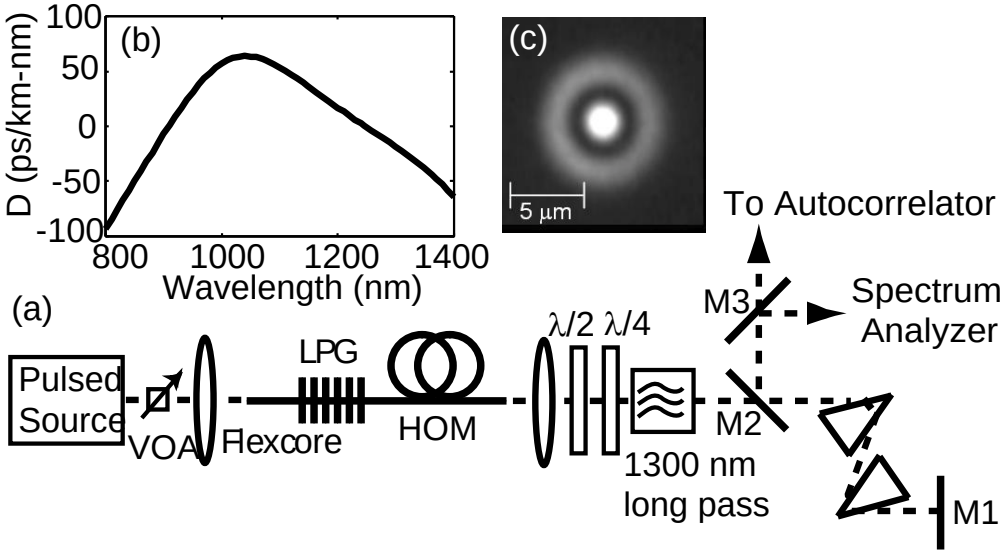

Figure 4.1. (a) Experimental setup used to measure the Cerenkov pulse generated in the HOM fiber, (b) measured dispersion for the LP_{02} mode in the HOM fiber, (c) the measured mode profile of the LP_{02} mode.

insets). For propagation in the HOM fiber, we include SPM (nonlinear parameter $\gamma = 2.2\ W^{-1}km^{-1}$), stimulated Raman scattering (Raman response $T_R = 5$ fs), self-steepening, wavelength dependent A_{eff}, and dispersion up to fifth-order. Dispersion coefficients are calculated by numerically fitting the dispersion curve shown in Fig. 4.1(b) [1]. We also scale the power accordingly during Raman wavelength-shifting to take into account energy lost to phonons.

4.3 Results and Discussion

We are able to couple a total power of 265 mW (3.31 nJ pulse energy) into the HOM fiber module. At this power level, the residual input, shifted soliton, and Cerenkov radiation can be clearly seen in the output spectrum shown in Fig. 4.2(a). The optical power residing in the Cerenkov band is ~53 mW (0.66 nJ pulse energy), a power conversion efficiency of 20% (25% photon conversion efficiency). We qualitatively match the experimental spectrum in simulation, shown in Fig. 4.2(b). We note the excellent qualitative match between simulation and experiment and the relatively good quantitative match. The observed quantitative discrepancy could arise from our approximation of both the input source characteristics and the dispersion curve, which is not characterized beyond 1400 nm. This simulated spectrum corresponds to an input power of 189 mW (2.36 nJ pulse energy), with 30% conversion to the Cerenkov band, equivalently 0.70 nJ in the Cerenkov pulse. At this power level, the soliton (centered at approximately 1200 nm) has shifted enough energy past the ZDW so that resonant coupling occurs efficiently at 1350 nm (Cerenkov radiation). Intuitively, growth of the Cerenkov radiation begins exponentially with increasing input power until the "spectral recoil" exerted by the Cerenkov radiation on the soliton cancels the Raman self-frequency shift [5]. After the

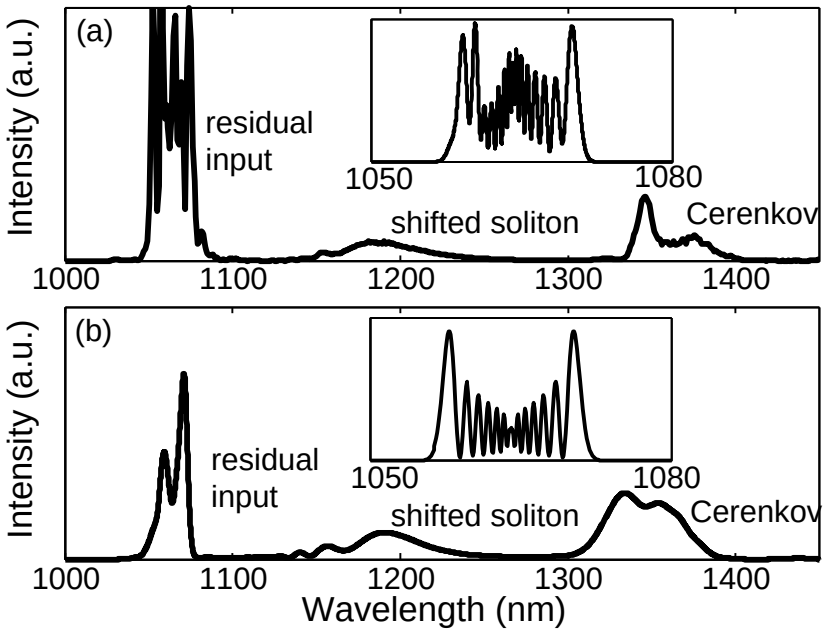

Figure 4.2. Optical spectrum at output of HOM fiber module. (a) from experiment, (b) from simulation. Insets show source spectra on a 30 nm window.

soliton is frequency-locked, for our experiment at 1200 nm, increasing the pump power will only transfer energy to the Cerenkov spectrum instead of shifting the soliton further. Simulation shows that up to approximately 5 nJ can be pumped into the Cerenkov band, after which nonlinear effects begin to degrade the system. Experimental pulse energies were limited by the pump source's non-Gaussian beam shape, which results in poor coupling into the HOM fiber module.

We additionally measure Cerenkov output pulse energy as a function of input pulse energy by varying the attenuation at the input of the HOM fiber module. We can see from Fig. 4.3 that the Cerenkov pulse energy increases rapidly at input energies of approximately 2 nJ (input power 160 mW). This "threshold" behavior, as well as the location of the knee agrees well with our simulation. The threshold behavior has also been experimentally observed previously in PCF [5]. A discrepancy in Cerenkov pulse energy between numerical results and experiment was found at the highest input pulse energies we investigated, where simulation shows a faster increase in Cerenkov energy than the experimental results. We currently do not have an explanation for this discrepancy.

A second order autocorrelation trace of the filtered Cerenkov pulse at the output of the HOM fiber module is shown in Fig. 4.4(a); it is visibly chirped and has an autocorrelation FWHM of 907 fs. We are able to compress this pulse to 207 fs autocorrelation FWHM, shown in Fig. 4.4(b), with appropriate dispersion compensation by a silicon prism pair. We calculate the dispersion provided by the silicon prism pair (prism separation distance approximately 7 cm in optical pathlength) to be $\beta_2 = -0.0065$ ps^2 and $\beta_3 = -1.9\times10^{-5}$ ps^3. Applying such dispersion compensation values to our spectrally matched simulation, we obtain numerically an autocorrelation FWHM of 200 fs and a pulsewidth of 103 fs. If we assume the same pulse shape, the experimentally measured deconvolved pulsewidths with and without

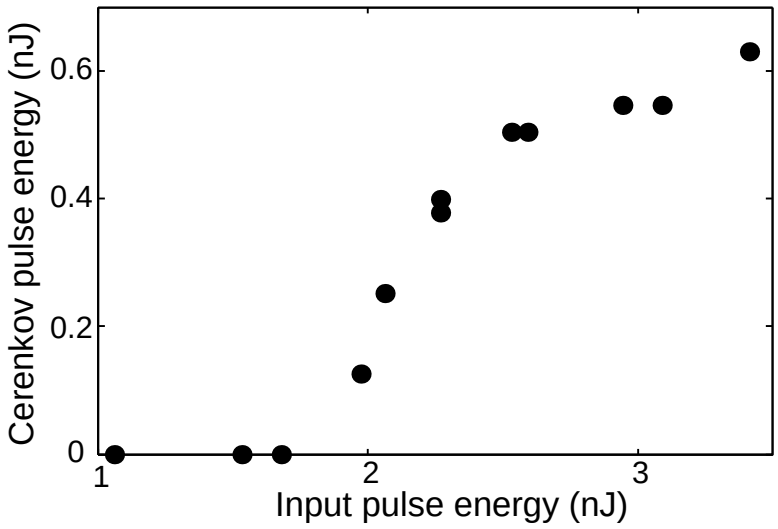

Figure 4.3. Cerenkov output pulse energy as a function of input pulse energy.

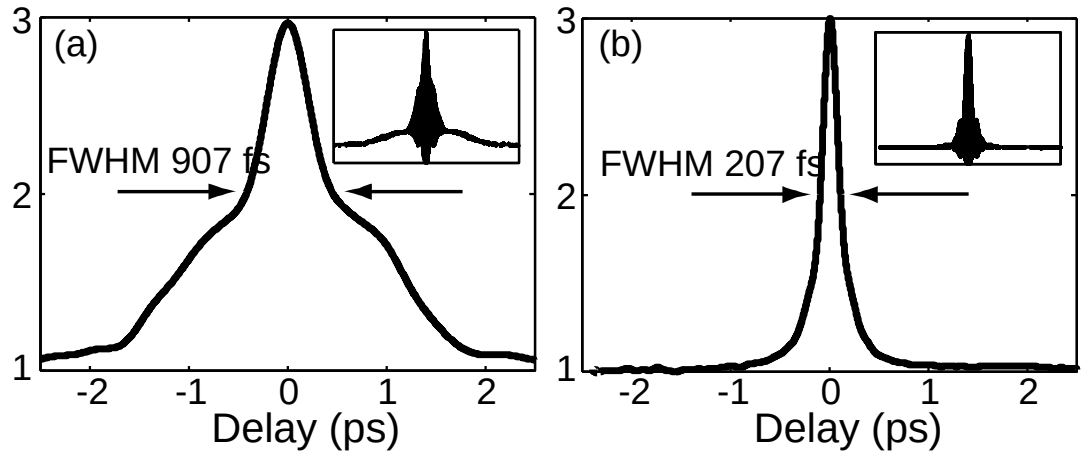

Figure 4.4. Intensity autocorrelation traces of Cerenkov pulse, (a) at the output of the HOM fiber module, without dispersion compensation, and (b) dispersion compensated pulse. Vertical axes span from 1 to 3 for collinear autocorrelation. Interferometric autocorrelation traces are shown in insets. Assuming the pulse shape predicted by simulation, this corresponds to pulsewidths of 465 fs and 106 fs, in (a) and (b) respectively.

dispersion compensation are 106 fs and 465 fs, respectively.

The location of the Cerenkov radiation can be tuned through engineering of the fiber dispersion [9]. For example, simple dimensional scaling of the index profile of the HOM fiber can be used to shift the dispersion curve of the LP_{02} mode. By shifting the ZDW 50 nm to the shorter wavelength side, the generated Cerenkov radiation will also shift by approximately the same amount. Such design control could lead to the generation of useful femtosecond pulsed sources in spectral regimes unattainable by current laser systems. Furthermore, the large effective area and flexibility for dispersion engineering in the HOM fiber open up the possibility to achieve pulse energies significantly beyond the level demonstrated here.

Although not demonstrated in our experiment, the generated Cerenkov pulse can be converted back to the fundamental mode by another LPG at the output of the HOM fiber module. With proper dispersion matching, efficient and broadband (> 100 nm) LPG has already been experimentally demonstrated for mode conversion [14]. On the other hand, depending on the intended usage, the higher order mode output could also be used directly without mode conversion.

4.4 Conclusions

In summary, we demonstrate a method of generating short pulses at 1350 nm by exciting Cerenkov radiation in a HOM fiber with a 1064 nm pulsed fiber source. We have successfully dechirped a 465 fs pulse at the output of the HOM fiber to a 106 fs pulse with a pair of silicon prisms. This method of generating short pulses at 1350 nm can potentially be extended to other wavelengths and to higher pulse energies with appropriate design of the HOM fiber.

REFERENCES

1. S. Ramachandran, S. Ghalmi, J. W. Nicholson, M. F. Yan, P. Wisk, E. Monberg and F. V. Dimarcello, "Anomalous dispersion in a solid, silica-based fiber," *Optics Letters*, vol. 31, pp. 2532-2534, 2006.

2. J. van Howe, J. H. Lee, S. Zhou, F. Wise, C. Xu, S. Ramachandran, S. Ghalmi and M. F. Yan, "Demonstration of soliton self-frequency shift below 1300 nm in higher-order mode, solid silica-based fiber," *Optics Letters*, vol. 32, pp. 340-342, 2007.

3. X. Liu, C. Xu, W. H. Knox, J. K. Chandalia, B. J. Eggleton, S. G. Kosinski and R. S. Windler, "Soliton self-frequency shift in a short tapered air-silica microstructure fiber," *Optics Letters*, vol. 26, pp. 358-360, 2001.

4. H. Lim, J. Buckley, A. Chong and F. W. Wise, "Fibre-based source of femtosecond pulses tunable from 1.0 to 1.3 μm," *Electronics Letters*, vol. 40, pp. 1523-1525, 2004.

5. D. V. Skryabin, F. Luan, J. C. Knight and P. S. J. Russell, "Soliton Self-Frequency Shift Cancellation in Photonic Crystal Fibers," *Science*, vol. 301, pp. 1705-1708, 2003.

6. G. Genty, M. Lehtonen, H. Ludvigsen, J. Broeng and M. Kaivola, "Spectral broadening of femtosecond pulses into continuum radiation in microstructured fibers," *Optics Express*, vol. 10, pp. 1083-1098, 2002.

7. J. Herrmann, U. Griebner, N. Zhavoronkov, A. Husakou, D. Nickel, J. C. Knight, W. J. Wadsworth, P. S. J. Russell and G. Korn, "Experimental Evidence for Supercontinuum Generation by Fission of Higher-Order Solitons in Photonic Fibers," *Physical Review Letters*, vol. 88, pp. 173901, 2002.

8. I. Cristiani, R. Tediosi, L. Tartara and V. Degiorgio, "Dispersive wave generation by solitons in microstructured optical fibers," *Optics Express*, vol. 12, pp. 124-135, 2003.

9. F. Lu, Y. Deng and W. Knox, "Generation of broadband femtosecond visible pulses in dispersion-micromanaged holey fibers," *Optics Letters*, vol. 30, pp. 1566-1568, 2005.

10. N. Akhmediev and M. Karlsson, "Cherenkov Radiation Emitted by Solitons in Optical Fibers," *Physical Review A*, vol. 51, pp. 2602-2607, 1995.

11. F. Biancalana, D. Skryabin and A. Yulin, " Theory of the soliton self-frequency shift compensation by the resonant radiation in photonic crystal fibers," *Physical Review E*, vol. 70, pp. 016615, 2004.

12. E. N. Tsoy and C. M. d. Sterke, "Dynamics of ultrashort pulses near zero dispersion wavelength," *Journal of the Optical Society of America B*, vol. 23, pp. 2425-2433, 2006.

13. G. P. Agrawal, *Nonlinear Fiber Optics*, San Diego, California: Academic Press, 2001.

14. S. Ramachandran, "Dispersion-tailored few-mode fibers: a versatile platform for in-fiber photonic devices," *Journal of Lightwave Technology*, vol. 23, pp. 3426-3443, 2005.

CHAPTER 5

AN ALL-FIBER SYSTEM FOR OBSERVING SSFS AND CERENKOV RADIATION IN LONG HOM FIBERS

5.1 Introduction

Recent developments in fiber design for dispersion engineering have led to the emergence of an all-silica fiber with anomalous dispersion below 1300 nm. This fiber has the unique dispersion characteristic of a large positive waveguide dispersion from higher-order mode (HOM) propagation that offsets negative material dispersion of silica [1]. Previously, this type of dispersion profile had only been accessible to microstructured optical fibers such as index-guided photonic crystal fibers [2] and hollow-core photonic bandgap fibers [3]. The anomalous dispersion profile of the HOM fiber used here, with moderate dispersion values (~60 ps/nm/km) at 1000 nm and a zero dispersion wavelength (ZDW) around 1215 nm, allows us to explore two nonlinear phenomena useful for generating short pulses: soliton self-frequency shift (SSFS) and Cerenkov radiation. SSFS is a consequence of intrapulse Raman scattering, causing a continuous wavelength shift of the pulse spectrum to longer wavelengths with propagation [4]. SSFS gives us access to a tunable wavelength source in the anomalous dispersion region with the shifting soliton [5]; Cerenkov radiation, a result of a phase-matched condition of the soliton k-vector to a dispersive wave on the other side of the ZDW, giving us a fixed-wavelength source in the normal dispersion regime [6, 7].

This wavelength shift has special appeal because it opens the door to designing simple, robust, compact fiber sources at wavelengths of interest for nonlinear optical

imaging, but where suitable in-fiber gain media are lacking. Recent reports have shown that by utilizing longer excitation wavelengths (1280 nm instead of 800 nm) to excite two-photon fluorescence, far greater penetration depths are possible [8]. Conventional pulsed sources for these long wavelength regimes are bulky and nontrivial to operate and maintain. For example, a Ti:Sapphire-pumped optical parametric oscillator, while having the desirable qualities of being widely wavelength-tunable, energetic, and of good spatial and temporal quality, does not lend itself naturally to widespread adoption for clinical practice due to their high cost, large size, and complex operation procedures. On the other hand, a HOM fiber system leveraging SSFS and Cerenkov radiation can access the similar wavelengths and pulse energies, while being fiber-delivered and requiring no optical alignment for operation.

Previous demonstrations of such a fiber-delivered source based on HOM fibers [5, 6] required a femtosecond input source to obtain the peak power needed to excite soliton formation and shift in a short length of HOM fiber (~1 m). However, with sufficiently long fiber length (a few meters), this condition can be relaxed. Indeed, we have shown that with a few-picosecond input and several-meters long HOM fiber we can still see the nonlinear phenomena previously observed. In this chapter we explain our understanding of the mechanism of SSFS and Cerenkov radiation in a picosecond-pumped HOM fiber. We demonstrate successful use of a picosecond source to excite wavelength-shifted solitons and Cerenkov radiation in an HOM fiber. We measured a 46 fs soliton pulse, and were able to obtain up to 28 % power conversion efficiency (~35 % photon efficiency) from the source wavelength to the Cerenkov band. We further show that the source is useful for biomedical imaging by employing it as the excitation source for a two-photon fluorescence microscope (TPM) to image lens tissue and mouse brains.

5.2 Propagation in Picosecond-pumped HOM Fibers

The realm of picosecond pumping differs from femtosecond pumping of HOM fibers because the input pulse energy required to observe soliton behavior within a length of fiber results in a much higher soliton order *N*. While the basic process of soliton fission, soliton shift, then Cerenkov generation still occurs, more than one of these pulse-creating nonlinear processes can happen in the length of HOM fiber. The generated wavelength components can overlap and interfere, leading to complex output pulse characteristics. To aid our understanding of these nonlinear phenomena from an HOM fiber, we carried out numerical calculations to solve the generalized nonlinear Schrodinger equation by integrating in the frequency domain, as described in Chapter 2. Fiber effects of dispersion, nonlinearity, frequency-dependent A_{eff}, self steeping, shock, and Raman response (as in (2.4)) are taken into account in calculations. The frequency domain approach allows for straightforward incorporation of the frequency-dependent A_{eff}, and behaves well under conditions that result in multiple-soliton formation. The dispersion (D) and A_{eff} of the fiber used in this experiment are shown in Fig. 5.1. Both dispersion and Aeff were fitted with a polynomial fit (dispersion to 11 orders, A_{eff} to 10).

We first consider a femtosecond input into a short length of HOM fiber. We simulate a 1.3 nJ, 400 fs transform-limited sech input into a 2 m length of HOM fiber. Spectrograms of the output at different lengths (at 0.4 m increments) are shown in Fig.5.2 (a-e), spectrograms shown use a 50 fs gate pulse. We observe, with increasing length, the phenomena of soliton-effect compression, fission of a single soliton, SSFS, and Cerenkov radiation generation. As the fully-shifted soliton propagates in the fiber, it is accompanied by the Cerenkov radiation on its leading edge. We see that the Cerenkov radiation propagates and disperses without interaction with other non-

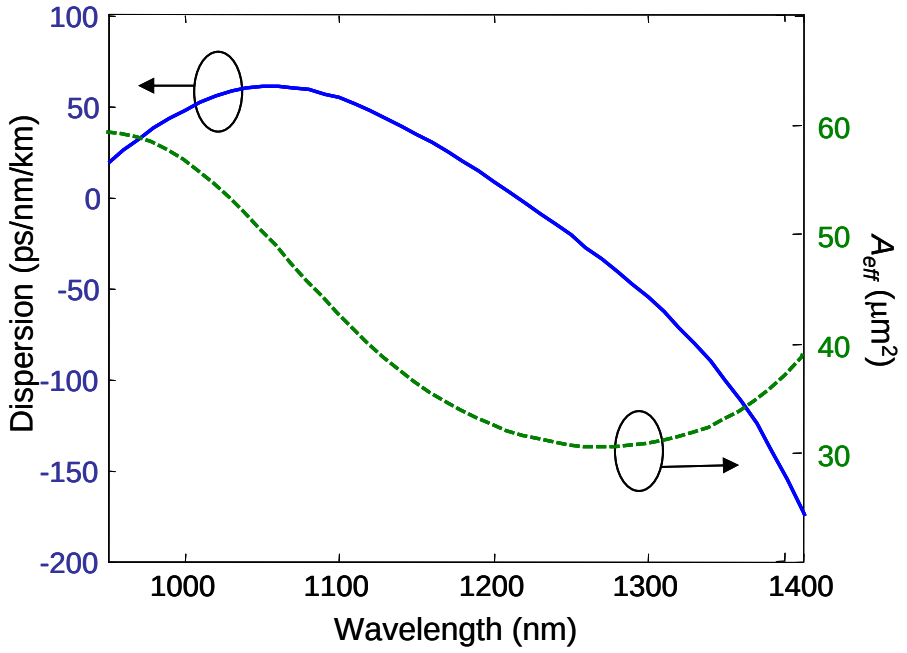

Figure 5.1: D and A_{eff} with respect to wavelength for the HOM fiber used. D is plotted on the left axis, A_{eff} is plotted on the right axis.

solitonic spectral components. At 2 m of HOM fiber propagation, we see that the very tail of the Cerenkov radiation overlaps in time with the residual input, and some cross-phase modulation occurs (Fig. 5.2 (e)).

For a picosecond input into a short length of fiber, the dynamics are more complex. We simulate a 5 nJ, 4 ps sech input with added SPM (~6.5 π) to simulate the spectral broadening caused by the fiber amplifier and SMF pigtail of the HOM fiber module. Representative spectrograms at different fiber lengths (0.3 m increments) for the picosecond input are shown in Fig. 5.2 (f-j). We see that the picosecond input pulse requires a considerable length of HOM fiber propagation for pulse compression (Fig. 5.2 (f) is at fiber length 4.2 m). Also, when the initial pulse compresses, it breaks up into many pulses, which is characteristic of soliton fission for high soliton orders [9, 10]. We see that the first soliton formed shifts and forms Cerenkov radiation over a very short length of fiber, and thus the temporal extent of the Cerenkov is much shorter than in the femtosecond case. We also observe that like in Fig. 5.2 (e), the Cerenkov band formed overlaps in time with the residual input, and becomes modulated (Fig. 5.2 (g)). Furthermore, as the light continues to propagate, the residual input fissions additional solitons (Fig. 5.2 (h-j)). These solitons interfere with the initially formed Cerenkov, as well as contribute to the energy in the Cerenkov band as they shift towards the ZDW and fulfill the phase matching condition between soliton and Cerenkov radiation. The case shown here in Fig. 5.2 (f-j) serves to illustrate multiple-pulse behavior that happens with large input pulse energies; at lower input pulse energies the picosecond input also exhibits single-soliton-Cerenkov generation as was seen with the femtosecond input. We draw a few conclusions from our simulations: First, at low input pulse energies, the Cerenkov radiation is formed by a

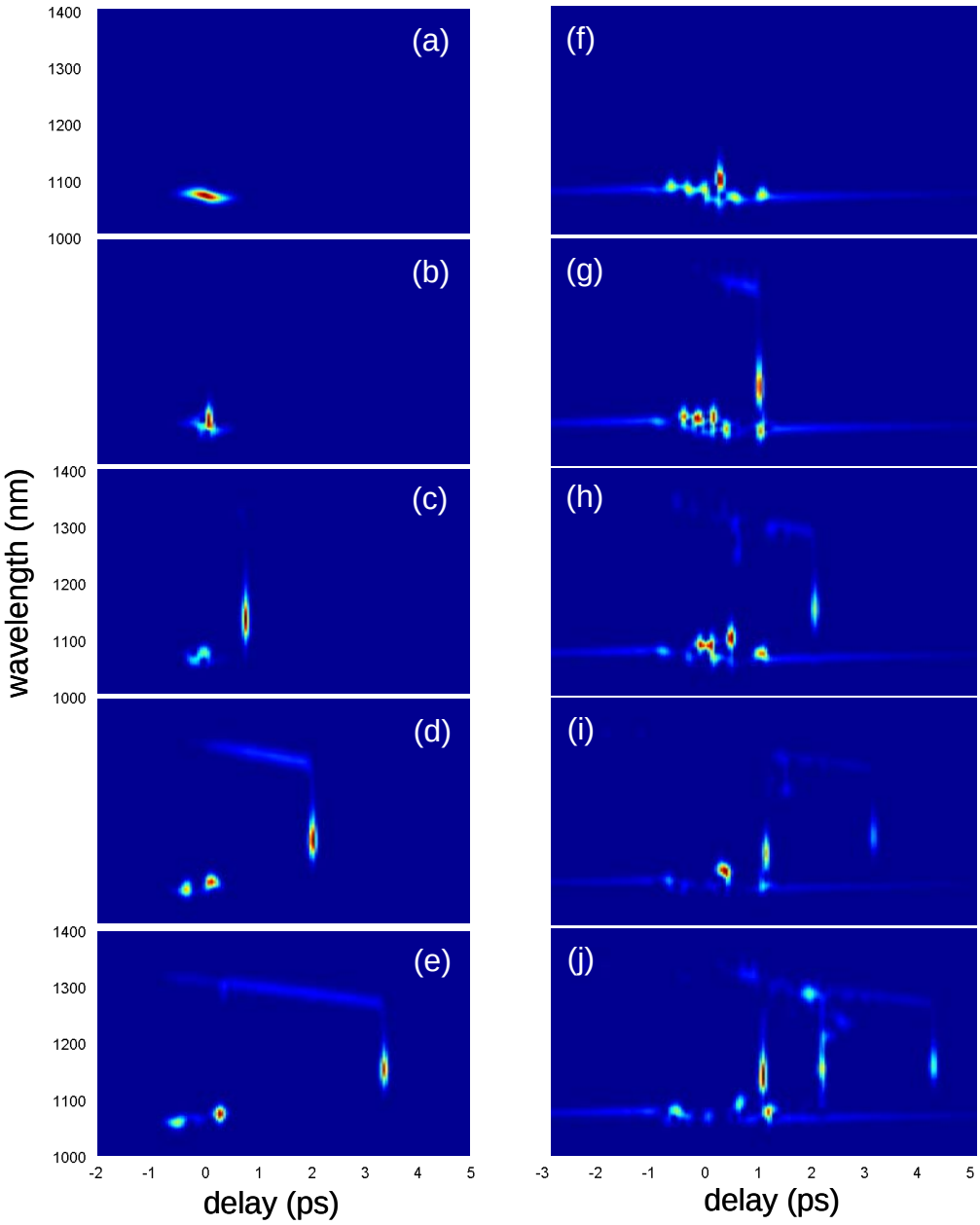

Figure 5.2. Calculated spectrograms for (a-e) 400 fs input into an HOM fiber,at 0.4m increments, starting with 0.4m fiber length in (a). Final output at fiber length of 2 m is shown in (e). (f-j) show spectrograms for 4 ps input, starting at 4.2m fiber length in (f) at 0.3 m steps for successive frames. Final fiber length in (j) is 5.5 m. Wavelength scale is the same for each subfigure.

single soliton and does not interact with radiation at other wavelengths. Second, when input energy increases, the temporal overlap between the Cerenkov radiation and the residual input causes interference in the leading edge (smaller delay side) of the Cerenkov pulse. Third, at even higher input energy, multiple solitons emerge successively from the input, and the later solitons both interact with and contribute to the initial Cerenkov radiation band.

5.3 Experimental Methods

We experimentally investigated the propagation of picosecond pulses in an HOM fiber. We used a semiconductor saturable absorber mirror (SESAM)-modelocked fiber laser [11, 12] as the light source for seeding our HOM fiber module. A schematic of the laser is shown in Fig. 5.3 (a). The linear cavity of the oscillator consisted of 0.75 m of Yb-doped gain fiber (Coractive), a SESAM (BATOP) which provided the modelocking mechanism, and a chirped fiber Bragg grating (CFBG, O/E Land) that served as both the source of anomalous in-cavity dispersion as well as the output coupler. Two seed sources were built for this work, one with center wavelength 1029 nm and the other at center wavelength 1062 nm. The oscillator design was the same except for the grating bandwidth of the CFBG. The oscillator was then amplified with a Yb-doped fiber amplifier (YDFA). The power amplifier stage utilized a large-mode-area (10 μm core) double-clad Yb-doped fiber (Liekki). For the 1029 nm source, a pre-amplifier stage (with 0.75 m Yb-doped fiber) before the final power amplifier stage was also used to boost the oscillator power to suitable levels for the power amplifier. Both the cavity and the preamplifier (when used) were pumped by a single-mode 980 nm fiber-coupled laser diode combined with a fiber wavelength division multiplexer (WDM) coupler, the high power amplifier employed a fiber-coupled 976 nm multimode pump diode combined with a high-power signal-pump

combiner (ITF Labs). Fiber inline isolators (Novawave) are used between amplifier stages to protect from back reflections. All components of the picosecond laser source are in-fiber and assembled by fiber splicing, except for the SESAM which was mechanically secured to the endface of a polished fiber. The SESAM allows for self-starting operation and the entire system is very robust to environmental fluctuations. Pump current of the final power amplifier stage was adjusted to achieve power tuning. The resulting source had ~65 MHz repetition rate and ~4 ps output pulsewidth, and average power up to 575 mW. Measurements at the output of the power amplifier indicate slight SPM broadening at the levels of amplification used in this experiment, but this is not of detriment to the results.

This picosecond laser source was then spliced directly to the HOM fiber module (OFS, od 134), and the output collimated and measured. The HOM fiber module consisted of ~0.8 m length of SMF pigtail, a long period grating (LPG) mode converter written on the HOM fiber, and total HOM fiber length of ~5.5 m. Total insertion loss (including splice loss and loss through the mode converter) was ~0.5 dB.

Since the picosecond source did not require any free-space compression optics (as with high-power femtosecond fiber sources employing chirped-pulse amplification), instability due to coupling a free space input to the HOM module was completely circumvented. Indeed, we observed remarkable power stability at the output of the HOM module (less than 1% fluctuation over 1 Hz - 100 kHz bandwidth and 2 % over 4 hours).

To characterize the output of the HOM fiber module spectrally, we measured its optical spectrum with an optical spectrum analyzer. Temporal characterization was carried out with a second-order autocorrelator in a Michelson interferometer setup (collinear geometry), and a prism compressor-based SFG cross-correlator [13]. A

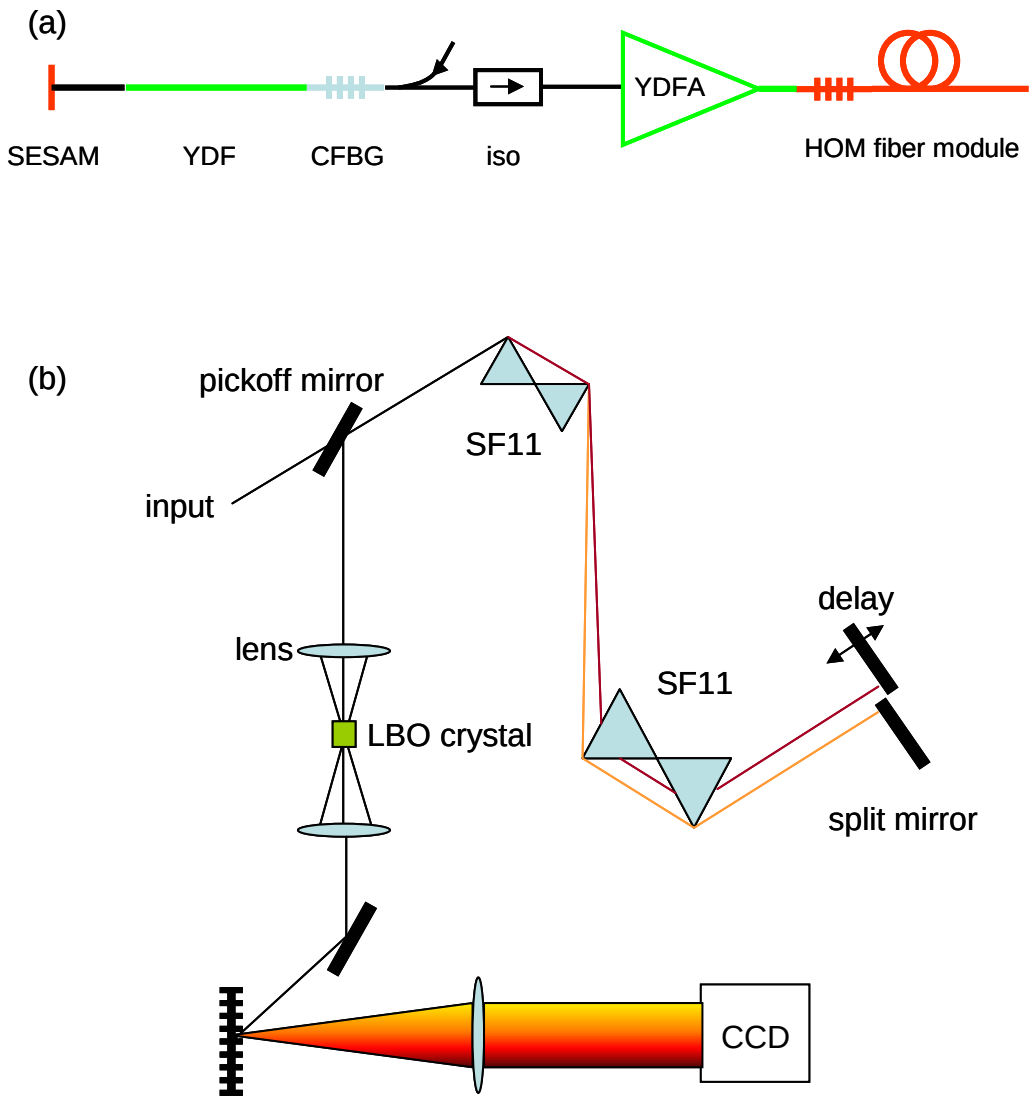

Figure 5.3 (a). Schematic of all-fiber HOM source. Arrows entering optical path denote locations of pump diodes. CFBG: chirped fiber bragg grating, YDFA: Ytterbium-doped fiber amplifier, iso: isolator. In (b), a schematic of the prism-compressor based cross-correlator.

schematic of the cross-correlator setup is shown in Fig. 5.3 (b). A pair of crossed SF11 prisms were used to obtain greater angular dispersion with less prism separation [14]. The prism compressor was aligned to provide zero dispersion. A split-mirror placed across the dispersed beam served to selectively delay different wavelength components. After the prism pair, the beam was focused (f = 5 cm) onto a Lithium triborate (LBO) crystal (5 mm), and the sum frequency signal detected with a GaAsP photodiode for the cross-correlation traces. Alternately, spectrally-resolved cross correlation traces were obtained by dispersing the sum frequency signal with a grating and imaging it onto a charge-coupled device (CCD) camera. For Cerenkov pulse compression, we used a pair of silicon prisms polished at Brewster's angle for dispersion compensation.

To verify the viability of our setup for biomedical imaging purposes, we performed two-photon fluorescence microscopy with our HOM fiber source. The output of the HOM fiber was directed to a raster-scanned TPM (Cambridge Technologies galvo-scanner, Sutter Instruments Movable Objective Microscope). The raster-scanned beam was focused into the sample by a high numerical aperture water immersion objective (Olympus UMPlanFL N 20x 0.5NA for the lens tissue imaging and Olympus XLMPlan Fluar 20x 0.95NA for the mouse imaging). The fluorescence from the sample was epi-collected and directed to a photomultiplier tube (PMT) by a dichroic mirror. We used a GaAs PMT (Hamamatsu H7422P-50) to collect the fluorescence signal. Microscope movement and image acquisition were controlled by a computer running MPScope [15]. Spectral components of the HOM fiber output were filtered for selective excitation of different fluorophores. For the residual and soliton wavelengths, lens tissue samples were prepared by staining with Texas Red (Invitrogen) and Alexa647 (Invitrogen). For the Cerenkov wavelength, the vasculature of an *in vivo* mouse brain was imaged. The vasculature was labeled with Alexa680

(Invitrogen). Methods used for *in vivo* sample preparation are detailed in Kobat et al [8].

5.4 Results and Discussion

First, we study the spectral output from the picosecond-pulse pumped HOM fiber. In previous chapters, we showed that a femtosecond input had sufficient peak power to induce the nonlinearities that cause soliton formation and soliton self-frequency shift (SSFS), and subsequently Cerenkov radiation. Here, we show that with sufficiently long HOM fiber length (a few meters), a picosecond input pulse can also generate the same phenomenon. Fig. 5.4 (a) shows the output spectra of a femtosecond pulse input (Polaronyx Uranus, center wavelength 1064 nm, 400 fs pulsewidth, 80 MHz) and in (b), picosecond input. Power was adjusted such that all three spectral features (residual input, shifted soliton, and Cerenkov radiation) are visible. Dispersion curves of the fiber are overlaid with the spectra, with the zero dispersion wavelength marked. Note that the soliton and Cerenkov radiation appear at the same positions (the soliton centered at 1180 nm, the Cerenkov about 1300 nm) despite differences in input wavelength and pulse width. This confirms our understanding that the locations of the spectral features are solely determined by the shape of the dispersion curve.

We note that though the picosecond input requires more pulse energy to generate equivalent spectra, the efficiency is respectable at high pulse energies where the Cerenkov band is saturated. Fig. 5.5 shows the output Cerenkov pulse energy as a function of input energy, as measured with the 1062 nm source. At maximum input energy available to our system, we observe a 2.4 nJ pulse energy in the Cerenkov

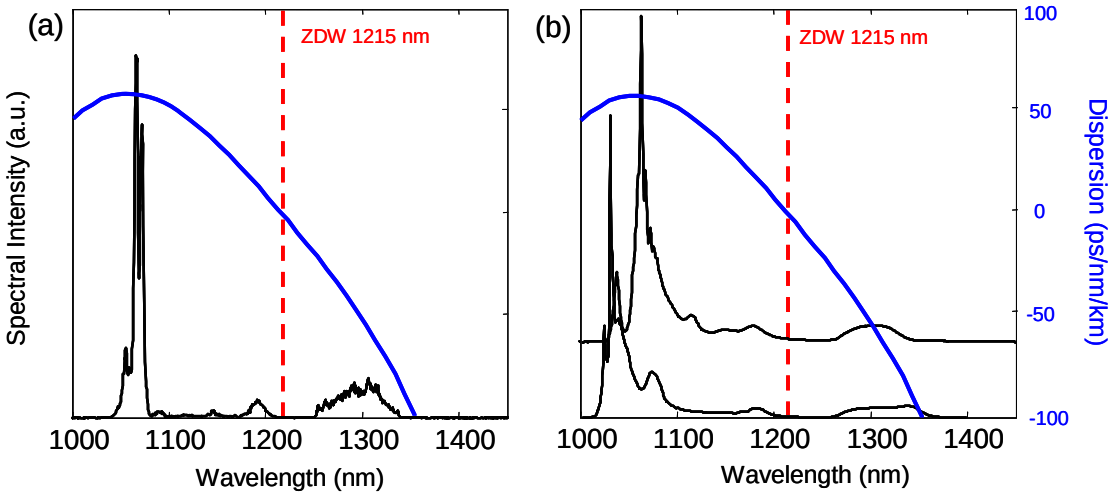

Figure 5.4: Experimentally measured output spectra for (a) femtosecond input to HOM fiber module, and (b) picosecond input to same HOM module, for both a 1029 nm source and one at 1062 nm, showing the locations of locked soliton and Cerenkov radiation. Spectra are offset in (b) for clarity.

radiation band, with 28% power conversion efficiency (35% photon efficiency) from the input wavelength to the Cerenkov wavelength. We note the shape of the power conversion curve in Fig. 5.5. The first sharp rise in Cerenkov energy occurs because of the thresholding behavior of the Cerenkov radiation as the soliton shifts to the ZDW. As input energy is increased, the Cerenkov energy then exhibits a knee as the soliton is now locked in wavelength and continues to transfer energy into the Cerenkov band. A second sharp rise in the Cerenkov energy occurs ~4.4 nJ input energy. Our simulations show that this is indicative of a second soliton beginning to also pump the Cerenkov band. At this first knee, where the Cerenkov radiation is only pumped by one soliton, the Cerenkov pulse energy is is ~0.4 nJ.

The ability to use a picosecond input is especially compelling because it enables us to have a truly all-fiber source that exhibits the nonlinear behavior in the HOM fiber, which was not possible in our previous work [5, 6]. The longer HOM fiber length here is the key to being able to use a picosecond input. Qualitatively, a long (picosecond) input shortens the effective "length" of HOM fiber propagation. Whereas in previous demonstrations, the entire 1-2 m length of HOM fiber was required to generate the shifted soliton and Cerenkov radiation, here the initial portion of the HOM fiber simply acts to generate the needed SPM-induced spectral broadening and pulse compression to produce a high peak power short pulse that then fissions a soliton and undergoes SSFS and Cerenkov generation.

Next we characterize the temporal properties of the output of the HOM fiber. We first verify that the soliton at the output is indeed a short pulse. The measured second order interferometric autocorrelation trace is shown in Fig 5.6 (a), and it shows a 86 fs autocorrelation FWHM, a 46 fs pulsewidth deconvolved assuming a sech^2 shape. We also characterize the output of the Cerenkov pulse by measuring its cross-correlation. The reference pulse used in the cross-correlation was the soliton,

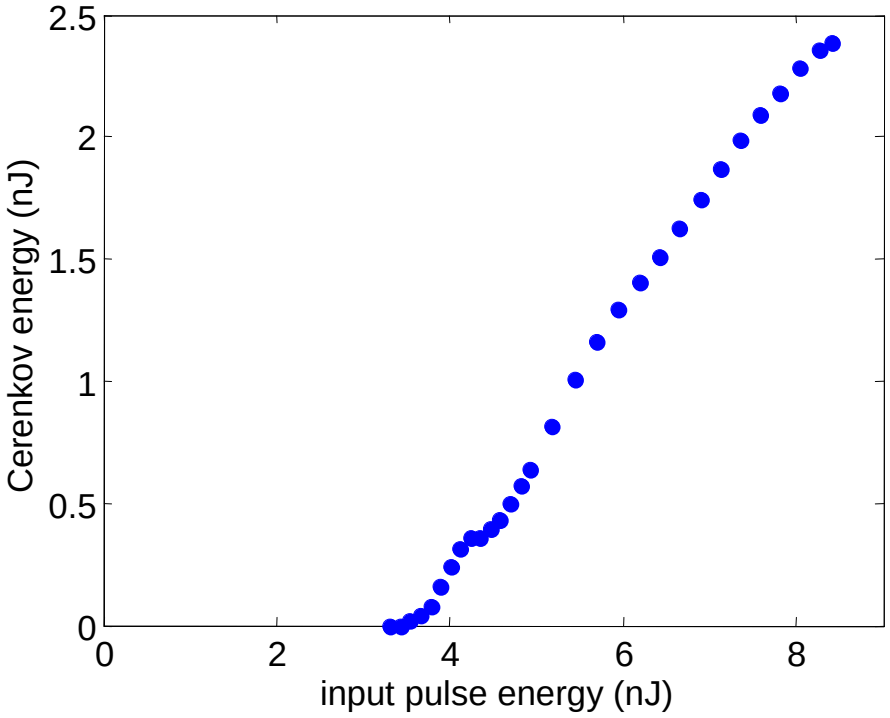

Figure 5.5 Energy in the Cerenkov band as a function of input pulse energy.

spectrally filtered in the cross-correlator. As the Cerenkov pulse at appreciable pulse energies has a pulsewidth much larger than the soliton, using the soliton to gate the Cerenkov faithfully maps the shape of the Cerenkov pulse in time. We show also in Fig. 5.6 two sample cross-correlation traces at 3.8 nJ input energy (Fig. 5.6 (b)) and 4.7 nJ input energy (Fig. 5.6 (c)). Fig. 5.6 (b) shows the shape we expect to see in the Cerenkov pulse. The mechanism of Cerenkov formation by the soliton gives it the sharp edge on the large delay side. The diminishing tail on the small delay side is indicative of the Cerenkov radiation's dispersive behavior. Fig. 5.6 (c) shows a cross-correlation trace at higher input energy. Here we see in addition to the sharp edge and diminishing tail, a skirt on the large delay side. This is due to the formation of a second soliton which is temporally offset from the first soliton. This behavior was seen in the calculated spectrograms shown in Fig. 5.2 (f-j).The second soliton also gates the Cerenkov pulse, but at a different relative delay. As such, the measured cross-correlation trace is a sum of the cross-correlation between the first soliton and the Cerenkov, and the second soliton and the Cerenkov. The second soliton, when just formed, is not as short as the initial soliton, which gives the cross-correlation the sloping edge on the positive delay side. While this overlay of cross-correlations from multiple solitons distorts the cross-correlation trace, we can make an estimate of the temporal extent of the Cerenkov by measuring the temporal width on the negative delay side of the cross-correlation (the edge at zero delay marking the overlap with the initial soliton).

Fig. 5.7 (a) shows a plot of measured Cerenkov cross-correlation widths as a function of input pulse energy. We show in Fig. 5.7 (b-e) a few representative frequency resolved cross-correlations. As with the cross-correlation traces, we

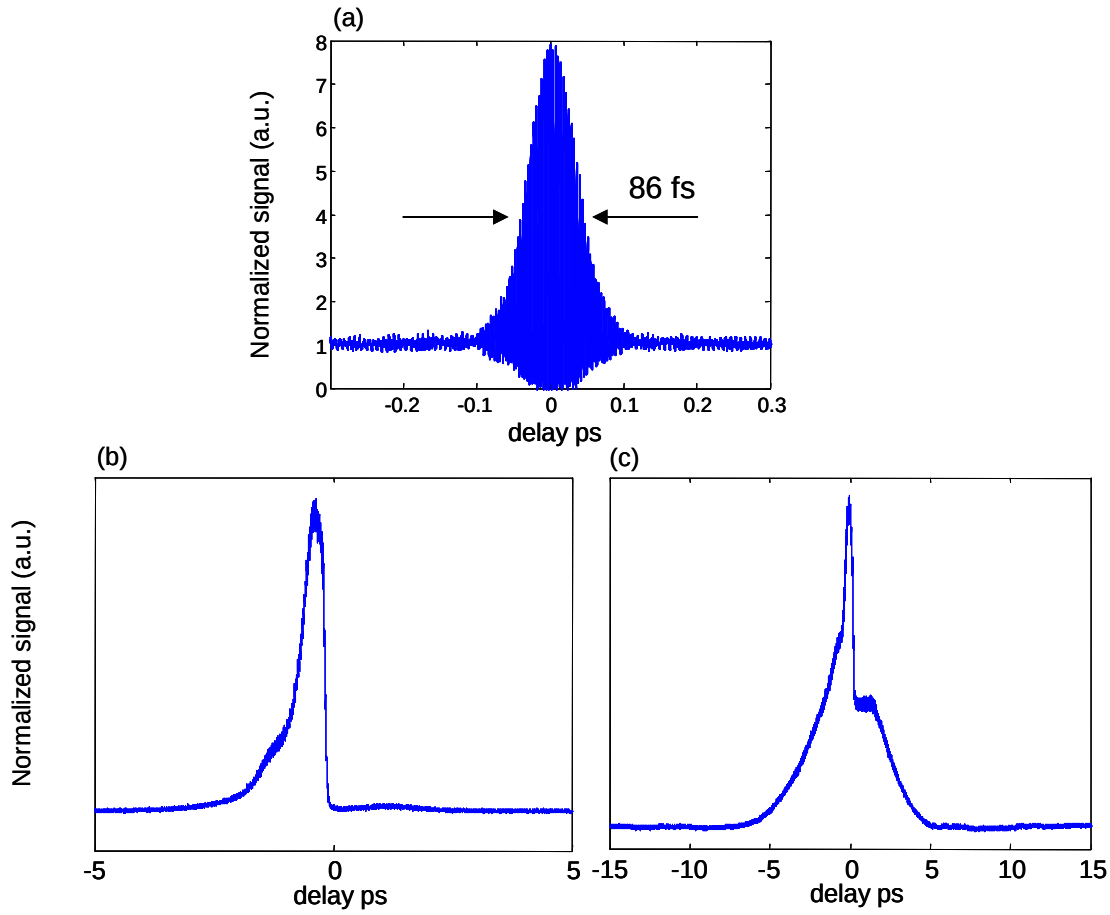

Figure 5.6 (a) Interferometric autocorrelation of the soliton pulse, its FWHM is 86 fs, 46 fs pulsewidth assuming a sech^2 shape. (b) and (c) show sample measured cross-correlation traces, for an input pulse energy 3.8 nJ in (b) and 4.7 nJ in (c).

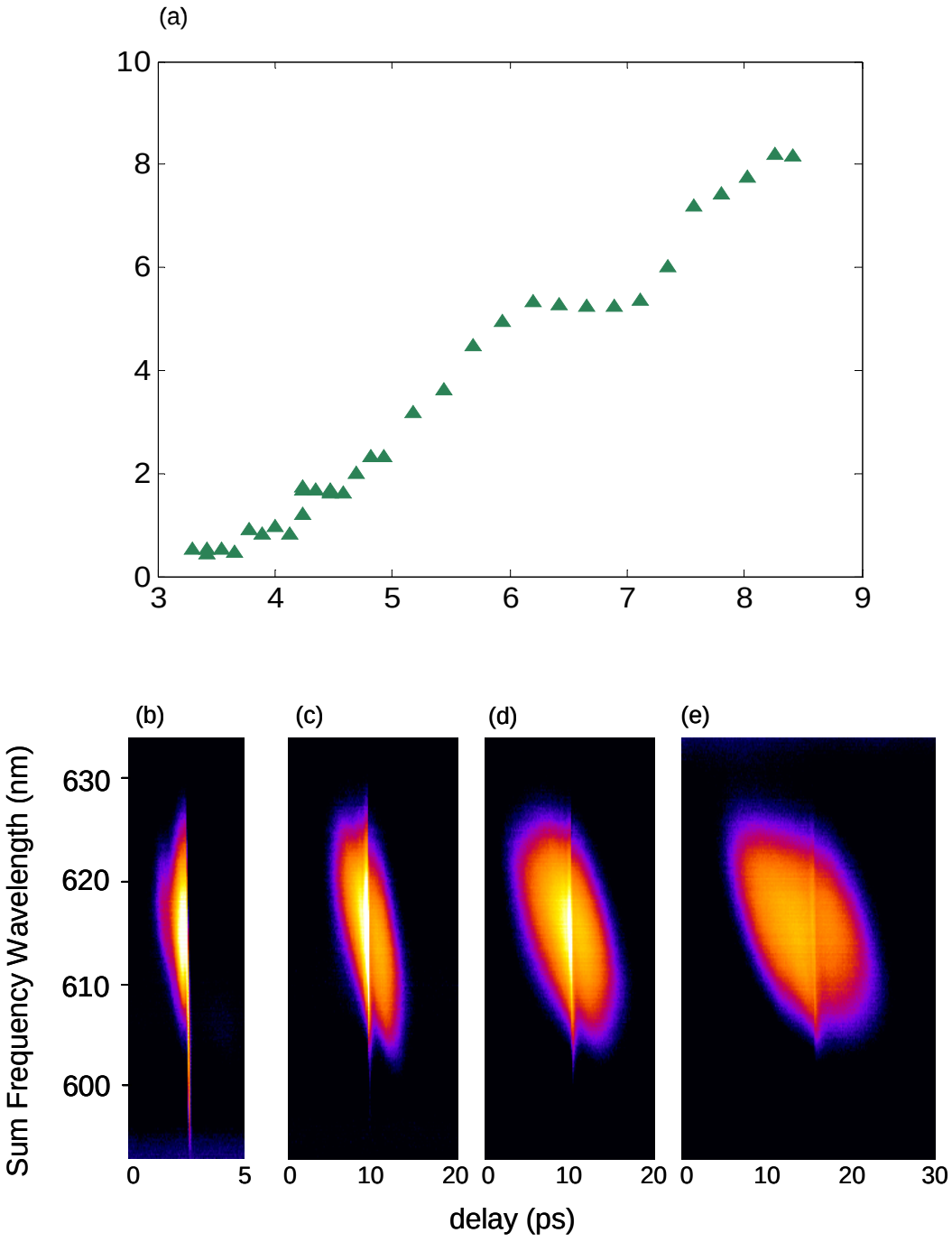

Figure 5.7 (a) Measured cross-correlation widths of the Cerenkov radiation with increasing input pulse energy. (b)-(e) show representative spectrally resolved sum-frequency generation cross-correlation traces, at input pulse energies are 3.8 nJ, 4.7 nJ, 6.2 nJ, and 8.4 nJ, from left to right.

examine the negative delay in relation to the first soliton (the first soliton creates a bright line at zero delay). The spectrogram shows that the Cerenkov energy is broad temporally as well as spectrally. We see that the Cerenkov width increases with increasing input pulse energy, both as a consequence of fiber dispersion, as well as the process of its formation by multiple solitons (for input pulse energies higher than ~4.4 nJ). In the regime where the Cerenkov radiation is formed by a single soliton and its broadening is governed by fiber dispersion, its energy is compressible, as was shown in Chapter 4 for femtosecond pumped HOM fibers. At higher input pulse energies, as the broadening can no longer simply attributed to chromatic dispersion, compression by group velocity dispersion (GVD) compensation becomes difficult. In our simulations, we see that at input energies where multiple solitons form the Cerenkov band (~4.4 nJ), GVD compensation does not yield significant improvement in expected two-photon fluorescence signal ($\propto \left\langle I(t)^2 \right\rangle$ [16]). Here, for long HOM fiber length and energetic picosecond input, we obtained best-effort compression of a Cerenkov pulse from 4.0 ps to 313 fs (measured intensity autocorrelation FWHM), and the shortest compressed pulse we were able to obtain was 230 fs, compressed from a 1.1 ps pulse (also intensity autocorrelation FWHM). Uncompressed and compressed interferometric autocorrelation traces are shown in Fig. 5.8 (a) through (d). The small skirt that remains in the compressed pulses may be due to residual third order dispersion that was not removed by the silicon prisms. Even with increasing cross-correlation widths and increasingly complex pulse profiles at Cerenkov energies, measured two-photon signal increases nonlinearly with Cerenkov energy. Fig. 5.9 shows normalized two-photon signal as a function of Cerenkov energy, with no dispersion compensation applied to the Cerenkov radiation. A fit of the log-log plot

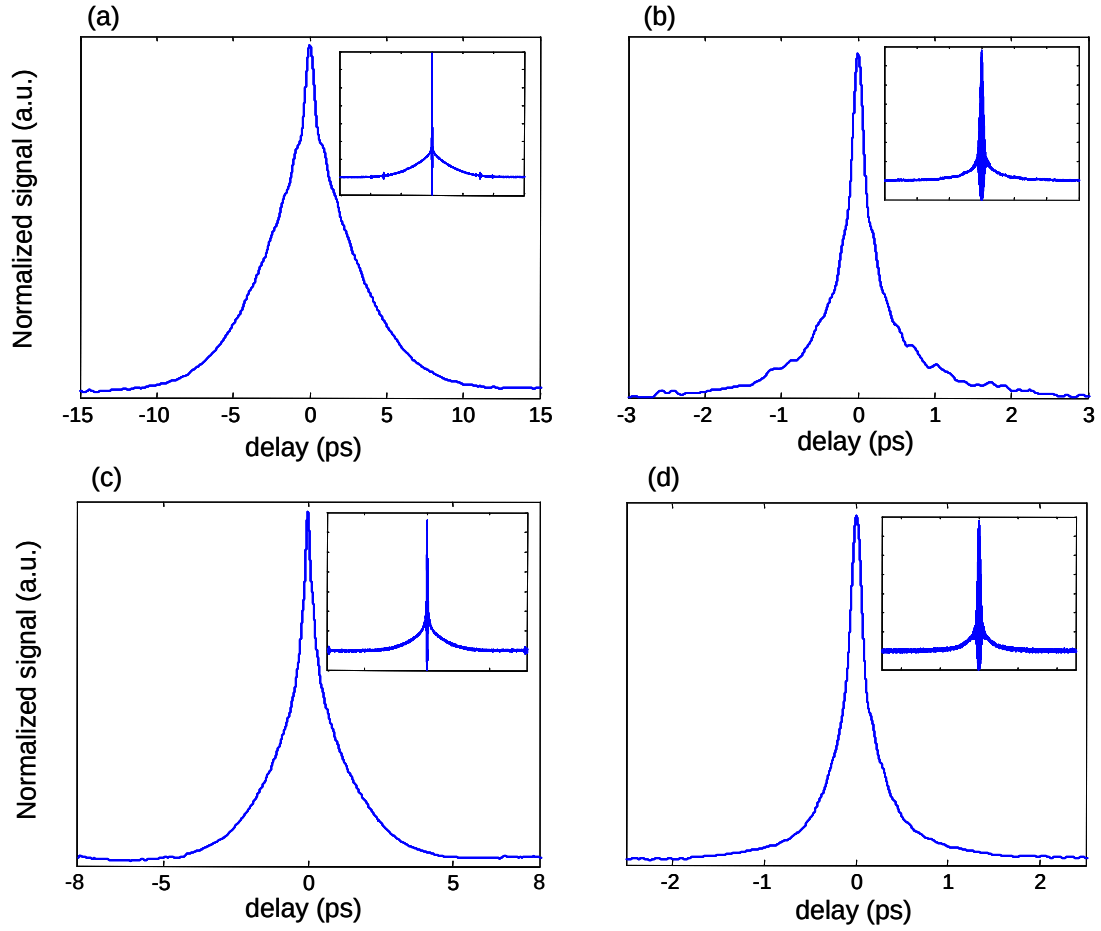

Figure 5.8 Autocorrelation traces for best-effort compressed Cerenkov pulses, in (a) and (b), an uncompressed 4.1 ps pulse and its corresponding 313 fs compressed pulse, in (c) and (d), an uncompressed 1.1 ps pulse and its corresponding 230 fs compressed pulse. All widths quoted are measured intensity autocorrelation FWHMs. Intensity autocorrelations shown in main figure, second order interferometric traces shown in inset.

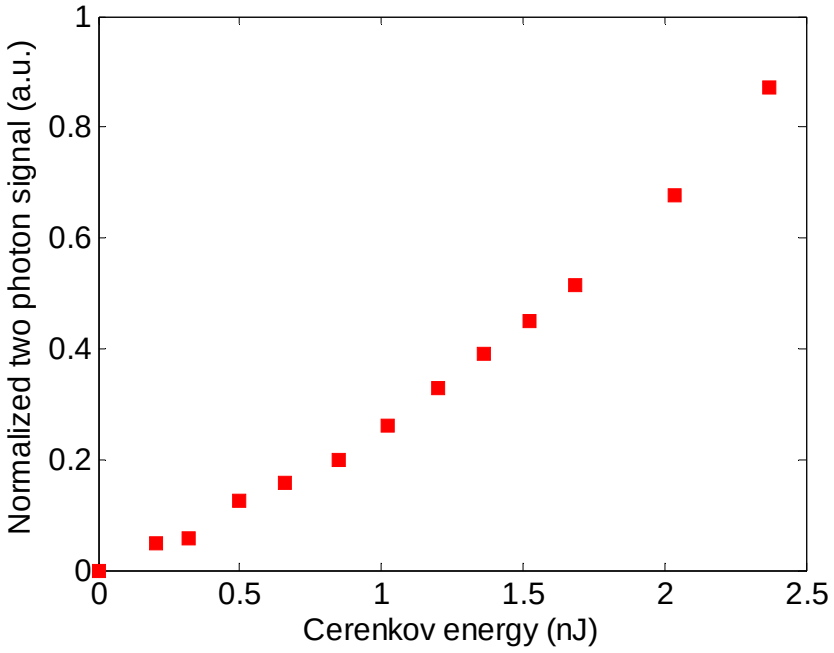

Figure 5.9 Measured two-photon signal as a function of Cerenkov energy. Two-photon signal is normalized.

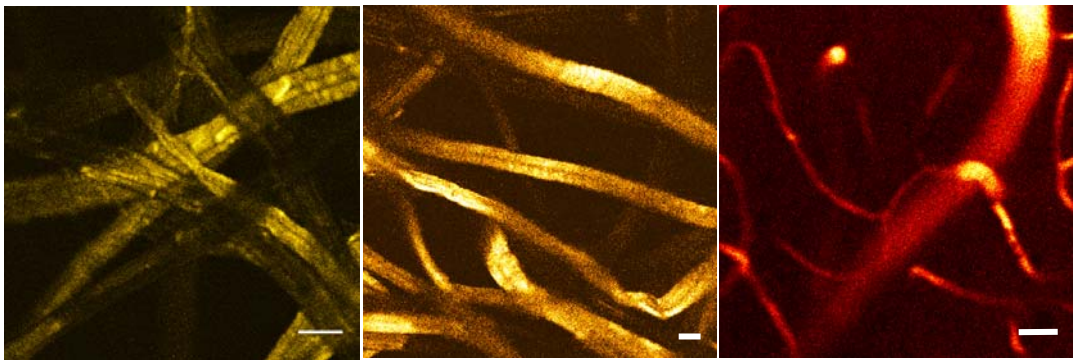

Figure 5.10 A few TPM images taken with the HOM fiber output. They are from left to right, imaged with the residual pump light at 1062 nm, the soliton at 1180 nm, and the Cerenkov about 1300 nm. The samples are dye-stained lens tissue for the residual and soliton, and an *in vivo* image of mouse brain vasculature for Cerenkov. Each image has a scale bar for 20 μm.

indicates the two-photon signal scales as $\sim \langle P_{Cerenkov} \rangle^{1.3}$. We conclude that though the Cerenkov radiation band is not a source of ideal pulses, its energetic output can still be viable for TPM applications.

Lastly, we take this system and show its usefulness for biological imaging applications. Lens tissue samples and cortical vasculature of a mouse were imaged by using this HOM-fiber-based source as the excitation light in a two-photon fluorescence microscope. Fig. 5.10 shows the images obtained, from left to right, with the residual input wavelength of 1064 nm, at the soliton wavelength of 1180 nm, and the Cerenkov radiation centered at 1300 nm. Each image shows a single z-section. A scale bar in each marks 20 μm. For each wavelength imaging, the output from the fiber source was filtered for each of the wavelength components; the Cerenkov energy was used uncompressed. We can see that even without compression, the Cerenkov light (26 mW measured at the sample) has sufficient peak power to excite two-photon fluorescence in this biological sample.

5.5 ***Conclusions***

We have shown an all-fiber short-pulsed source covering wavelengths from 1029 nm to ~1300 nm. This source employs a picosecond fiber laser in conjunction with long HOM fiber to generate a wavelength-shifted soliton at 1180 nm and a Cerenkov radiation band about 1300 nm, with the residual input ~ 1 μm, all three suitable for biomedical imaging. We have characterized both the soliton and the Cerenkov, and shown that even with the long input pulse, short and energetic pulses can be obtained from the long HOM fiber length. We measured a 46 fs soliton pulse, and a maximum Cerenkov energy of 2.4 nJ (28% power conversion efficiency). Lastly, we showed this system in application as the light source for two-photon fluorescence microscopy. The combination of the picosecond input, all-fiber

configuration, and fiber delivered short pulse output make this an attractive component for further imaging applications.

REFERENCES

1. S. Ramachandran, S. Ghalmi, J. W. Nicholson, M. F. Yan, P. Wisk, E. Monberg and F. V. Dimarcello, "Anomalous dispersion in a solid, silica-based fiber," *Optics Letters*, vol. 31, pp. 2532-2534, 2006.

2. J. C. Knight, J. Arriaga, T. A. Birks, A. Ortigosa-Blanch, W. J. Wadsworth and P. S. Russell, "Anomalous dispersion in photonic crystal fiber," *IEEE Photonics Technology Letters*, vol. 12, pp. 807-809, 2000.

3. R. F. Cregan, B. J. Mangan, J. C. Knight, T. A. Birks, P. S. Russell, P. J. Roberts and D. C. Allan, "Single-mode photonic band gap guidance of light in air," *Science*, vol. 285, pp. 1537-1539, 1999.

4. E. M. Dianov, A. Y. Karasik, P. V. Mamyshev, A. M. Prokhorov, V. N. Serkin, M. F. Stelmakh and A. A. Fomichev, "Stimulated-Raman Conversion of Multisoliton Pulses in Quartz Optical Fibers," *JETP Letters*, vol. 41, pp. 294-297, 1985.

5. J. van Howe, J. H. Lee, S. Zhou, F. Wise, C. Xu, S. Ramachandran, S. Ghalmi and M. F. Yan, "Demonstration of soliton self-frequency shift below 1300 nm in higher-order mode, solid silica-based fiber," *Optics Letters*, vol. 32, pp. 340-342, 2007.

6. J. H. Lee, J. van Howe, C. Xu, S. Ramachandran, S. Ghalmi and M. F. Yan, "Generation of femtosecond pulses at 1350 nm by Cerenkov radiation in higher-order-mode fiber," *Optics Letters*, vol. 32, pp. 1053-1055, 2007.

7. D. V. Skryabin, F. Luan, J. C. Knight and P. S. Russell, "Soliton self-frequency shift cancellation in photonic crystal fibers," *Science*, vol. 301, pp. 1705-1708, 2003.

8. D. Kobat, M. E. Durst, N. Nishimura, A. W. Wong, C. B. Schaffer and C. Xu, "Deep tissue multiphoton microscopy using longer wavelength excitation," *Optics Express*, vol. 17, pp. 13354-13364, 2009.

9. A. V. Husakou and J. Herrmann, "Supercontinuum Generation of Higher-Order Solitons by Fission in Photonic Crystal Fibers," *Physical Review Letters*, vol. 87, pp. 203901, 2001.

10. J. Herrmann, U. Griebner, N. Zhavoronkov, A. Husakou, D. Nickel, J. C. Knight, W. J. Wadsworth, P. S. J. Russell and G. Korn, "Experimental Evidence for Supercontinuum Generation by Fission of Higher-Order Solitons in Photonic Fibers," *Physical Review Letters*, vol. 88, pp. 173901, 2002.

11. O. Katz, Y. Sintov, Y. Nafcha and Y. Glick, "Passively mode-locked ytterbium fiber laser utilizing chirped-fiber-Bragg-gratings for dispersion control," *Optics Communications*, vol. 269, pp. 156-165, 2007.

12. K. Kieu, B. G. Saar, G. R. Holtom, X. S. Xie and F. W. Wise, "High-power picosecond fiber source for coherent Raman microscopy," *Optics Letters*, vol. 34, pp. 2051-2053, 2009.

13. M. R. X. de Barros and P. C. Becker, "Two-color synchronously mode-locked femtosecond Ti:sapphire laser," *Optics Letters*, vol. 18, pp. 631-633, 1993.

14. B. Proctor and F. Wise, "Quartz prism sequence for reduction of cubic phase in a mode-locked Ti:Al2O3 laser," *Optics Letters*, vol. 17, pp. 1295-1297, 1992.

15. Q.-T. Nguyen, P. S. Tsai and D. Kleinfeld, "MPScope: A versatile software suite for multiphoton microscopy," *Journal of Neuroscience Methods*, vol. 156, pp. 351-359, 2006.

16. W. R. Zipfel, R. M. Williams and W. W. Webb, "Nonlinear magic: multiphoton microscopy in the biosciences," *Nature Biotechnology*, vol. 21, pp. 1369-1377, 2003.

CHAPTER 6

FOCUSING OF THE HIGHER ORDER MODE

6.1 Introduction

Higher order mode (HOM) fibers have generated interest as potential platforms for creating fiber-based sources for biomedical imaging. It is of particular interest to the nonlinear microscopy field because the ability of such fibers to deliver short pulses in the near infrared. Conventional single mode fiber cannot support soliton propagation below 1.3 μm due to the normal dispersion contribution of both the material and the waveguide for the fundamental mode. On the other hand, HOM fibers are capable of achieving anomalous waveguide dispersion to counteract the material dispersion of silica [1]. In addition, the index profile is engineerable to tune the region of anomalous dispersion. Anomalous dispersion allows for energetic short-pulse delivery via the nonlinear phenomena surrounding soliton propagation [2], and HOM fibers have been shown to support solitonic propagation over a wavelength range spanning 1.0 um to 1.3 μm [3]. These pulses fit the high-peak-power low-repetition rate requirements for multiphoton microscopy [4]. While the HOM fiber can generate the temporal profile desirable for nonlinear microscopy techniques, its spatial profile is different from the Gaussian beam profile typical to light sources for nonlinear microscopy. The HOM shows promise, though, as it was recently reported that the LP_{02} mode (from a similar HOM fiber as used here) has improved lateral resolution over the LP_{01} mode for nonlinear focusing [5]. In this chapter, we investigate the full 3-D focusing properties of the LP_{02} mode obtained from an HOM fiber. We study its nonlinear excitation focal volume by looking at its intensity-squared point spread

function (PSF), as measured by two-photon fluorescence microscopy (TPM) of 1.0 μm fluorescence-labeled beads. We show that at various back aperture filling ratios, we can obtain vastly differing PSFs. At one particular filling ratio, we obtain a null at the focal spot, much like the depletion beam focus of stimulated emission depletion microscopy systems. Finally, we conclude by discussing the potential uses of such a mode for applications to microscopy and micromanipulation.

6.2 Calculating the point spread function

To understand the image focus, we consider an incident field distribution on a pupil defined by radius α. By the Huygens-Fresnel principle, we consider every point in the pupil to be an emitter of spherical wavelets and construct the field in the focal region as a superposition of these point emitters. Assuming radial symmetry of the incident field, $F(\theta)$, we can introduce it as a pupil function to the derivation of the focus from a circular aperture. Following Richards and Wolf [6], we write the field in the focal region as

$$\begin{aligned} E_x &= -iA\left(I_0 + I_2\cos(2\phi)\right) \\ E_y &= -iAI_2\sin(2\phi) \\ E_z &= -2AI_1\cos(\phi) \end{aligned} \quad . \tag{6.1}$$

A is a constant proportional to the incident field amplitude, and ϕ is the azimuthal angle in the spherical coordinate system. The integrals I_0, I_1, and I_2 are given by

$$\begin{aligned} I_0(u,v) &= \int_0^\alpha F(\theta)\cos^{\frac{1}{2}}(\theta)\sin(\theta)\left(1+\cos(\theta)\right)J_0\left(v\frac{\sin(\theta)}{\sin(\alpha)}\right)e^{iu\frac{\cos(\theta)}{\sin^2(\alpha)}}d\theta \\ I_1(u,v) &= \int_0^\alpha F(\theta)\cos^{\frac{1}{2}}(\theta)\sin^2(\theta)J_1\left(v\frac{\sin(\theta)}{\sin(\alpha)}\right)e^{iu\frac{\cos(\theta)}{\sin^2(\alpha)}}d\theta \\ I_2(u,v) &= \int_0^\alpha F(\theta)\cos^{\frac{1}{2}}(\theta)\sin(\theta)\left(1-\cos(\theta)\right)J_2\left(v\frac{\sin(\theta)}{\sin(\alpha)}\right)e^{iu\frac{\cos(\theta)}{\sin^2(\alpha)}}d\theta \end{aligned} \tag{6.2}$$

where θ is the radial coordinate in the pupil plane, and the optical coordinates (u,v) are defined with origin at the focus and have the following relation to spatial coordinates z and r:

$$\begin{aligned} u &= kz\sin^2(\alpha) \\ v &= kr\sin(\alpha) \\ NA &= n\sin(\alpha) \end{aligned} \quad . \tag{6.3}$$

$k = 2\pi/\lambda$, NA is the numerical aperture of the focusing element, and n is the index in the focal region. Under the limit of low-NA focusing and for regions close to the focus (θ and α small), Eqn. (6.2) reduces to

$$\begin{aligned} I_0(u,v) &= 2e^{i\frac{u}{\alpha^2}}\int_0^\alpha F(\theta)\theta J_0\left(v\frac{\theta}{\alpha}\right)e^{-iu\frac{\theta}{2\alpha^2}}d\theta \\ I_1(u,v) &= e^{i\frac{u}{\alpha^2}}\int_0^\alpha F(\theta)\theta^2 J_1\left(v\frac{\theta}{\alpha}\right)e^{-iu\frac{\theta}{2\alpha^2}}d\theta \\ I_2(u,v) &= \frac{1}{2}e^{i\frac{u}{\alpha^2}}\int_0^\alpha F(\theta)\theta^3 J_2\left(v\frac{\theta}{\alpha}\right)e^{-iu\frac{\theta}{2\alpha^2}}d\theta \end{aligned} \tag{6.4}$$

In addition, integrals I_1, and I_2 are much smaller than I_0 for the case of low-NA focusing, so we will only consider I_0 when calculating the field in the focal region. The field in the focus is proportional to I_0, and the two-photon emission fluorescence (TPEF) signal scales as the intensity squared, so the TPEF PSF follows an I_0^4 dependence.

$$PSF_{two-photon} \propto \left[\left|2e^{i\frac{u}{\alpha^2}}\int_0^\alpha F(\theta)J_0\left(v\frac{\theta}{\alpha}\right)e^{iu\frac{\theta}{2\alpha^2}}d\theta\right|^2\right]^2 \tag{6.5}$$

6.3 Experimental Methods

We characterized the focusing properties of the LP_{02} mode by measuring the two-photon fluorescence PSF. The light source used to supply the HOM beam was a semiconductor saturable-absorber mirror (SESAM)-modelocked picosecond Yb-fiber

laser system (homebuilt) at center wavelength 1062 nm, spliced to a HOM fiber module (OFS Laboratories, od134). The fiber laser served as a seed for pumping the HOM fiber, which at large input energies exhibits the nonlinear phenomena of self phase modulation, soliton fission, soliton self-frequency shift, and subsequently Cerenkov radiation generation. These nonlinear processes provide three wavelength bands of radiation, each with pulsed energy, which could be used separately to excite different fluorescent probes. For the measurement of PSFs the seed laser power was kept relatively low and while some spectral broadening from self-phase modulation was observed, no additional wavelength bands (soliton, Cerenkov) were generated. The measured intensity autocorrelation full-width at half-maximum (FWHM) of the excitation pulse was about 2 ps, showing some soliton-effect compression within the HOM fiber. The HOM beam used was at center wavelength 1064 nm, with maximum power (at greatest underfilling) of 51 mW measured at the sample. We measured the profile of the beam at the back aperture by scanning a single mode fiber (SM980) across the beam and measuring the transmitted power with a fiber power meter.

The output of the higher order mode fiber was collimated with a 0.4 NA aspheric lens and directed to a raster-scanned TPM (Cambridge Technologies 6 mm galvo-scanner, Sutter Instruments Moveable Objective Microscope). The beam was focused through a 20x, 0.50 NA water immersion microscope objective (Olympus UMPlanFL N) onto the sample, the two-photon fluorescence epi-collected and directed via a dichroic mirror to a GaAs photomultiplier tube (PMT, Hamamatsu H7422P-50). A 700 nm short pass filter (Thorlabs) was used to separate the fluorescence signal from the excitation light. We prepared a sample of 1.0 μm orange fluorescent beads (540/560, Invitrogen) in a 3% solution of low-melting point agarose gel (Sigma Aldrich). Bead dilution was controlled to have individually resolvable

beads within each image stack. Sample TPM images were taken of lens tissue samples stained with Texas Red dye (Invitrogen).

We varied the back aperture filling ratios by inserting appropriate telescopes in the beampath to achieve the correct beam size at the back aperture. We observed the beam at the back aperture with a charge coupled device (CCD) camera, and measured the diameter of the null ring in the LP_{02} mode to obtain back aperture filling parameter β. We define the parameter as $\beta = d_{BA} / d_{null}$, where d_{null} is the diameter of the null ring, and d_{BA} is the diameter of the back aperture of the objective. Larger β values correspond to underfilling of the objective, and in the limit of $\beta \to 0$, the field incident on the back aperture is a plane wave. For the objective used in this work, the back aperture diameter was 10 mm. The software program MPScope [7] was used to control the objective movement and acquire the image stacks. Bead images were recorded by taking 16 μm by 16 μm x-y plane images at 0.2 μm depth increments. Each frame was 512 by 512 pixels taken at ~3 fps, averaged for 3 frames per depth step. Vertical stacks were acquired over sufficient depth to capture the axial extent of the bead fluorescence. Image stacks were assembled in ImageJ to extract the PSF cross-sections; axial and radial profiles were extracted from these cross-sectional images. No smoothing or additional image processing was applied to the cross-section images. To verify our understanding, we also calculated the PSF numerically using Eqn. (6.5). We used the calculated LP_{02} mode solution of the HOM fiber for the pupil function $F(\theta)$; the mode profile was provided by scientists at OFS Laboratories. Fig. 6.1 (a) plots the mode profile used in calculations and the mode profile measured at the back aperture. Fig. 6.1 (b) shows calculated fraction of total mode intensity retained at various filling ratios β.

6.4 Results and Discussion

We recorded TPM images of the 1.0 μm beads. We note that the beads are below the diffraction limit in the axial dimension, but are close to but not below the diffraction limit in the lateral dimension. We verified with 0.2 μm beads that the lateral dimension of the PSF obtained with the 1.0 μm bead was not noticeably exaggerated. Due to low signal from the 0.2 μm beads, we chose to image the 1.0 μm beads. Acknowledging this, we will still refer to the TPM images as PSFs for simplicity. Note that these are the intensity squared PSFs, as the TPEF signal $\propto I^2$.

Several representative PSFs are shown in Fig. 6.2 at different back aperture filling ratios, from underfilling on the left to overfilling on the right. The back aperture filling ratios are, from left to right, $\beta = 3.7$, 2.8, 2.5, 1.9, 1.4, and 0.5. A scale bar in the upper right hand corner demarks 5 μm. It is important to recognize that while the PSFs are shown as a cross-section, all of the PSFs measured were symmetric under rotation about the optical axis. We note the evolution of the PSF as the beam is expanded to overfill the back aperture, from a PSF with extended axial confinement and narrow lateral confinement (large β), to one with two distinct axial focal lobes and an annular ring at the focal plane, to a near diffraction-limited focal spot (small β). We note further that for β larger than 1.4, all PSFs exhibit an annular ring structure at the focal plane.

We can understand the focusing behavior as follows: with the outer ring of the LP_{02} mode being of opposite phase from the central peak, for the proper back aperture filling, the focused field from the central peak and the outer ring can exactly cancel, forming the null that is observed at $\beta = 1.9$. As the filling parameter β is decreased, the contribution from the opposite phase outer ring is less and dark region diminishes until at $\beta = 1$ ($d_{null} = d_{BA}$) only the central peak remains. Further decreasing β from there, the focus behaves as a Gaussian beam that is increasingly apertured. As β approaches

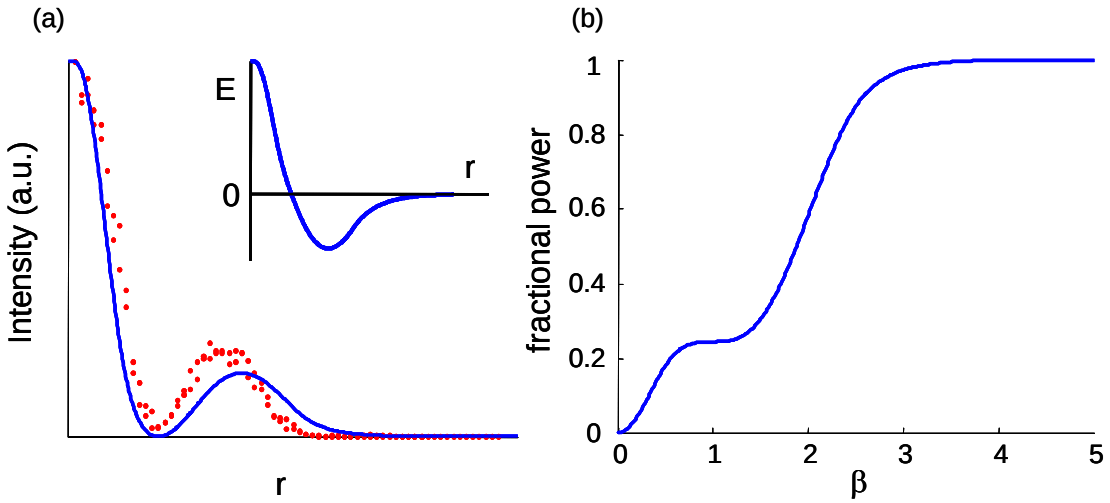

Figure 6.1 (a) Theoretical (solid line) and measured (dots) intensity profile of the LP_{02} mode plotted against radial distance, at the back aperture of the imaging objective. Inset in (a) plots the field against radial distance, showing the phase change across the null of the mode; (b) shows the fractional power in the mode for various back aperture filling ratios β, calculated by integrating the theoretical mode profile shown in (a).

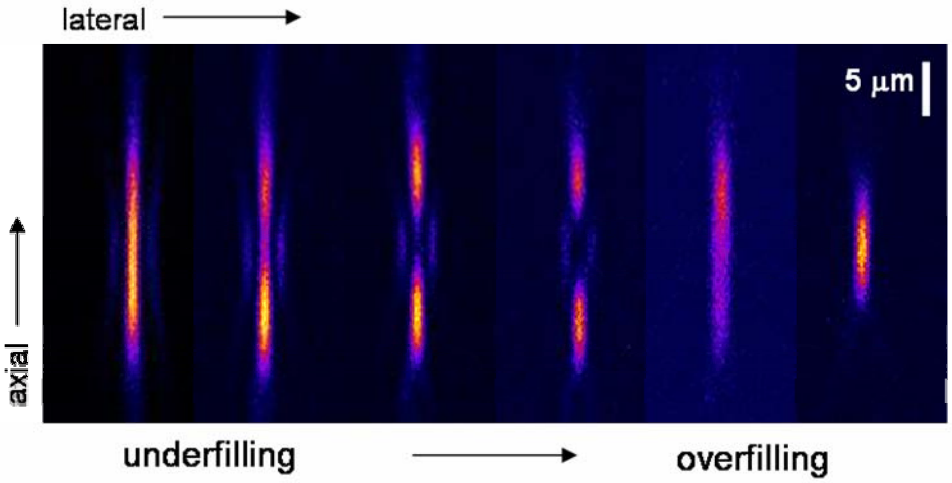

Figure 6.2 Intensity squared point spread functions as measured from two-photon fluorescence imaging of 1μm dyed polystyrene beads. Back aperture filling was adjusted by adding appropriate telescopes. PSFs are shown for increasing beam size on the back aperture from left to right, shown for a few representative filling ratios: $\beta = 3.7$, 2.8, 2.5, 1.9, 1.4, and 0.5. This spans the range from under- (for $\beta = 3.7$) to over-filling (for $\beta = 0.5$) of the objective back aperture. Raster-scanned images were recorded at 0.2 μm steps in depth, the images stacked and cross sections shown here. Scale bar is 5 μm, shown in the upper right hand corner.

zero, the field at the aperture approaches a plane wave and the focus approaches the diffraction limit. On the other side, as β is increased from the condition with the null focus, the field at the focus gains more contribution from the outer ring, raising the intensity at the focus. At largest β the lateral PSF approaches the 2D Fourier transform of the LP_{02} mode.

We verify our understanding of the HOM focusing by comparing the measured lateral and axial profiles of the PSFs with that calculated from Eqn.(6.5). Fig. 6.3 and Fig. 6.4 show the profiles at several representative back aperture fillings; the radial TPEF profile is plotted in Fig. 6.3 against radial distance in microns, and the axial TPEF profile is plotted in Fig. 6.4 against axial distance in microns. TPEF values are normalized independently for each profile. Profiles shown are for experimentally measured β = 3.7, 2.6, 1.9, and 0.5, from top to bottom, and best-match calculated profiles are for β = 3.0, 2.2, 1.6, and 0.5. The difference between measured β values and β values of best-fit calculated profiles is due to the deviation between measured LP_{02} mode profile and the mode solution used in the calculations. While the LP_{02} mode was calculated for the index-profile designed, variations in manufacturing can lead to minor differences in calculated and observed mode profiles. We can see this difference, especially for the outer ring of the mode, in the measured and calculated mode profiles shown in Fig. 6.1(a). We will use the β values for calculated profiles when we refer to the PSFs; these are noted in Fig. 6.3 and Fig. 6.4. Measured β values can be scaled by 0.8 to match β used in calculations.

We note the excellent agreement between calculated and experimentally observed radial and axial profiles. Looking at Fig. 6.3, we see that the shape of the radial profile evolves from a Gaussian-like shape for lowest β values (overfilling, approaching plane-wave focus) to a central dip and a peak a few microns from the optical axis for moderate β values, to a profile much like the starting mode itself for

highest β values. The axial profiles in Fig. 6.4, like the radial, start with a Gaussian-like shape for the lowest β values, evolves into a central dip with an outer lobe at moderate β values, back to a more centralized focus at highest β values. If we examine the radial and axial profile for $\beta = 1.6$, we can clearly discern the central null that was observed in one of the PSFs shown in Fig. 6.2.

We show in Fig. 6.5 two sample TPM images taken at different back aperture fillings. Both images are of a single z-section of dyed lens tissue samples. The scale bar shows 20 μm, a total field of view of 315 μm x 315 μm. Subfigure (a) shows the resulting image with back aperture filling $\beta \sim 1$, and (b) shows image with back aperture filling $\beta \sim 3$. We observe that the fibers of the lens paper are not as sharp in (b) as in (a), due to the extended axial focus of the HOM at large β values. The annular ring in the focal plane for large β values is dim enough not to cause significant distortion to the TPM image. We conclude that the LP_{02} mode from an HOM fiber can feasibly be used for TPM for either under- (large β) or over-filled (small β) cases.

6.5 Focal "Holes" and Phase Modification

Figure 6.5 shows the "darkness" of the PSF at the focus. For each β value, two-photon signal at the focus is plotted, normalized to the highest two-photon signal in the PSF. Background signal, determined by averaging pixels far away from the focus, is subtracted from both signal at focus and maximum signal of the PSF. β values measured in experiment were scaled by 0.8 to match the calculated β. We see for $\beta \sim 1.3$ to 2.0 there is a measured hole in the center of the focal volume.
We take a closer look at the case $\beta = 1.6$, where there is a measured null at the focus of the beam. We calculate the "darkness" of the focal "hole" by measuring the average pixel value in a small volume at the focus, and comparing it to the bright axial lobes and the focal plane annular ring. To account for photon noise, a background

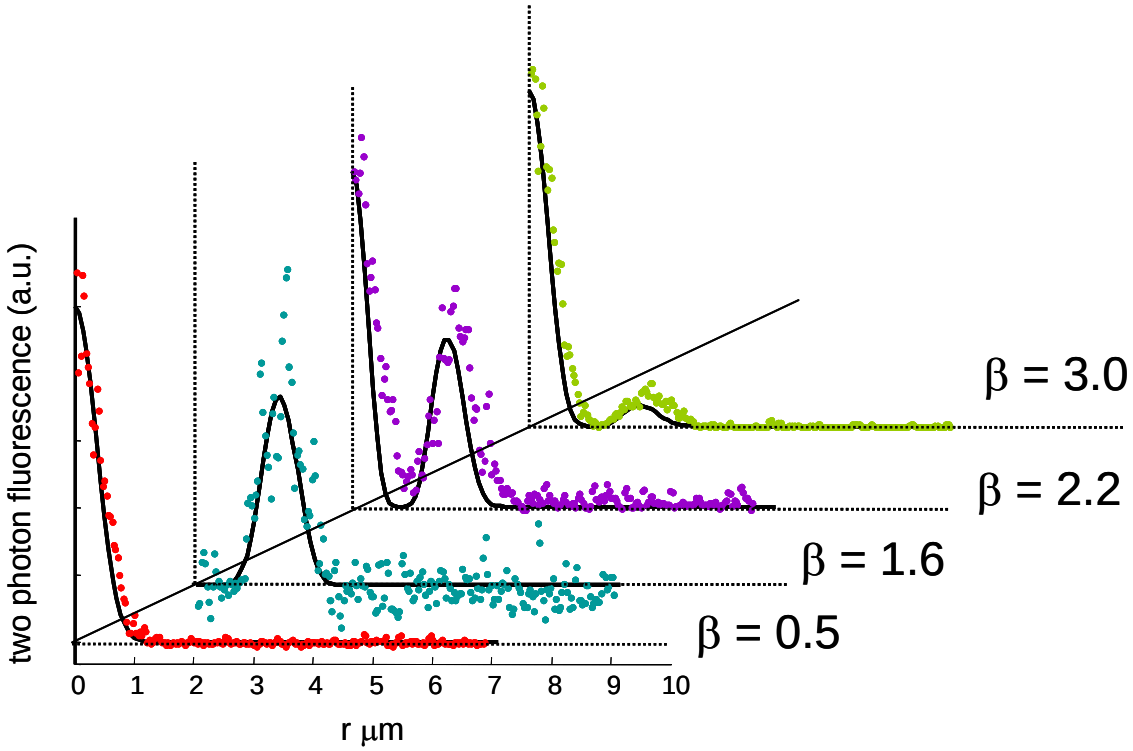

Figure 6.3 Radial profiles of the intensity squared point spread functions. The profiles from top to bottom are for back aperture filling ratios $\beta = 3.0$, 2.2, 1.6, and 0.5. Experimental profiles, shown in the colored dots, were taken from recorded point spread functions as shown in Figure 6.2. Black curves show calculated profiles. Curves are offset for clarity.

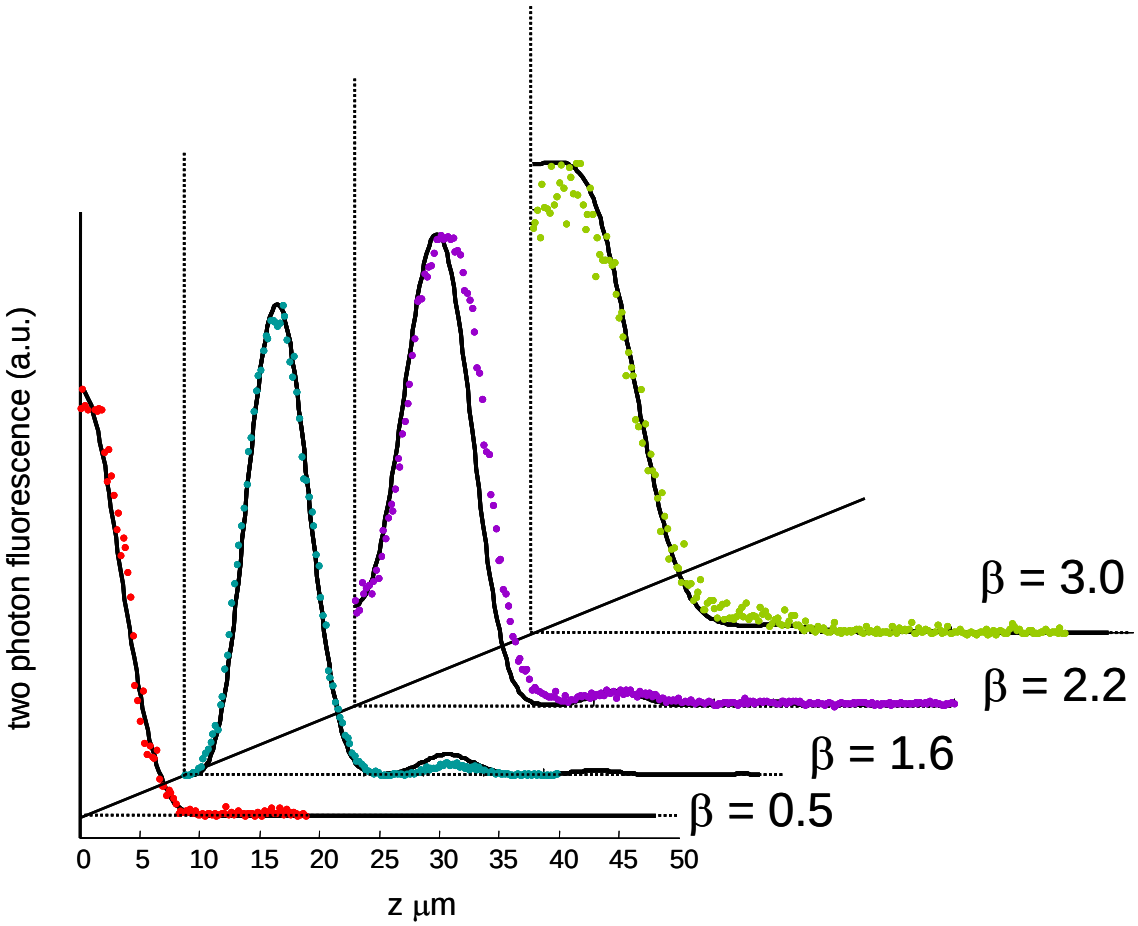

Figure 6.4 Axial profiles of the intensity squared point spread functions. The profiles from top to bottom are for back aperture filling ratios $\beta = 3.0$, 2.2, 1.6, and 0.5. Experimental profiles, shown in the colored dots, were taken from recorded point spread functions as shown in Figure 6.2. Black curves show calculated profiles. Curves are offset for clarity.

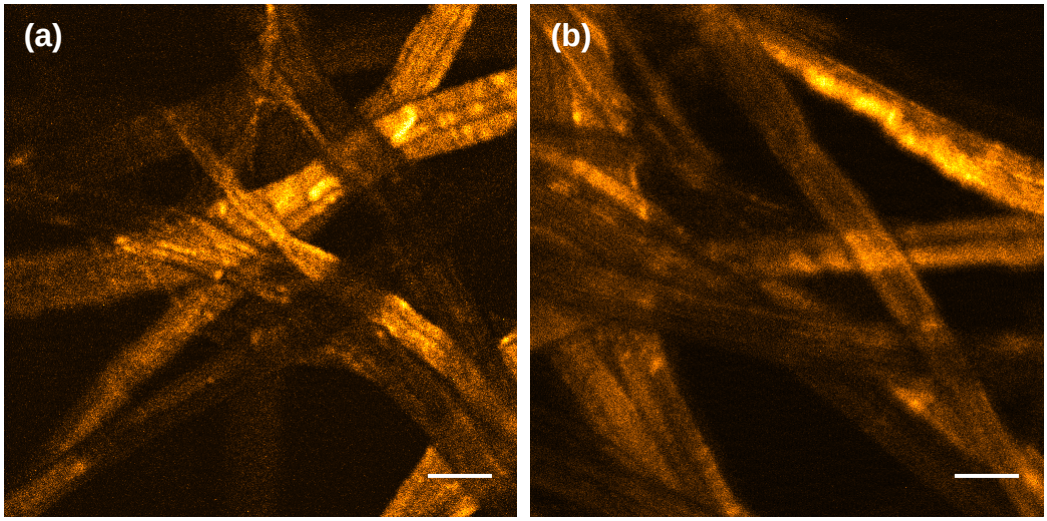

Figure 6.5 Two examples of images taken with the HOM. Both are lens tissue samples stained with Texas Red dye, (a) with a just-overfilled beam (β~1), (b) with an underfilled beam (β~3). The white scale bar indicates 20 μm.

pixel value is determined by measuring the average pixel value in some small volume far away from the bead in the acquired stack. For $\beta = 1.6$, the contrast of the bright axial lobe to the dark focus is ~33 dB and the annular ring to the dark focus is ~20 dB. Our calculated PSF for $\beta = 1.6$ yields 52 dB and 43 dB for axial and radial contrast, respectively. The experimentally measured contrast is limited by photon noise and the dynamic range of our measurement method, we believe that for the correct filling ratio the focal hole can be completely dark.

We note that this special case has a very similar focal volume shape as a beam used for stimulated emission depletion (STED) microscopy [8]. Since STED microscopy employs a one-photon depletion process, comparison between intensity (not intensity squared) PSFs will be discussed here. In Fig. 6.7, we show the calculated intensity PSF for our focused HOM beam at $\beta = 1.6$ in (a), and a typical depletion beam for STED microscopy in (b). The insets of Fig. 6.7 (a) and (b) show the intensity profile at the back aperture for the HOM (a), and the phase profile at the back aperture for the STED beam (b). The STED beam was created by placing a phase mesa (defined as a cylindrical bump centered on the optical axis) in the beampath, giving the center of the beam π phase shift compared to the outer regions. For the correct choice of mesa size, yielding opposite phase for half of the amplitude in the back aperture, a null appears at the focus due to destructive interference of the π phase-shifted wavefronts [8]. We calculate here a plane wave with a mesa radius of $r_{mesa} = a/\sqrt{2}$, where a is the radius of the back aperture. This yields the condition described above; we will refer to this type of beam as the plane-phase beam.

We see qualitatively in Fig. 6.7 (a) and (b) the match between the HOM focus and the plane-phase focus. We also plot the radial and axial profiles in (c) and (d) to show the similarity of the two focal distributions. The power at the back aperture for

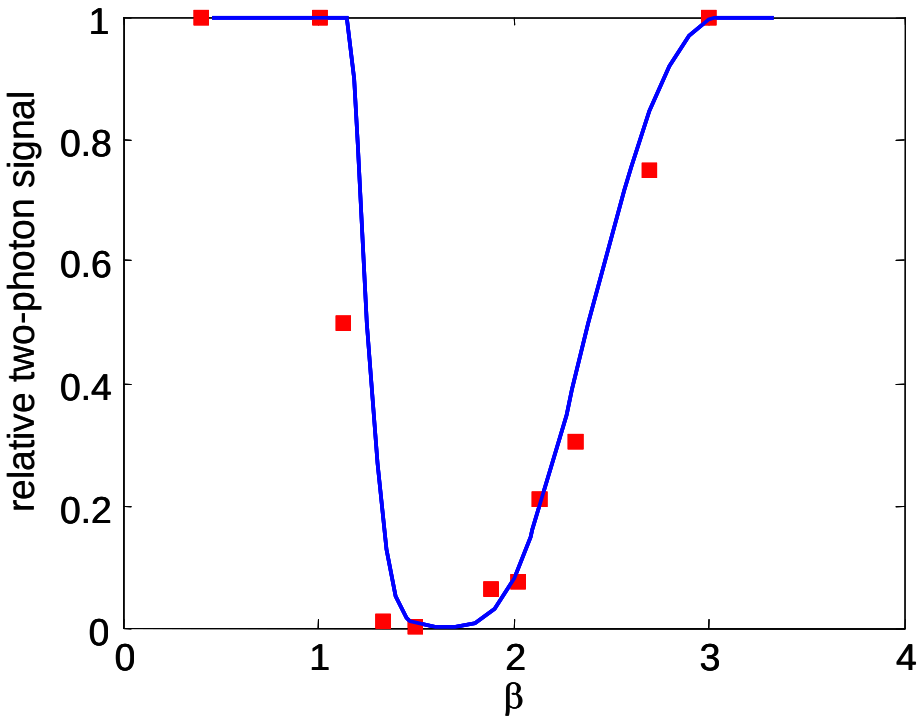

Figure 6.6 Relative two-photon fluorescence signal at focus at different filling ratios, normalized to maximum signal in PSF at that filling ratio. Red squares mark experimentally measured values; the blue line denotes calculated values.

the HOM and the plane-phase beam are normalized to a plane wave incident on the back aperture. We note that the intensity value of the peak of the annular ring in the HOM focus is 50% more than that of the STED beam, and the axial profiles are comparable. We can also compare the size of the focal "holes" created by the HOM focus and the plane-phase focus. We define a dark focus half-width at half-maximum (HWHM) by measuring the inner location of the half-maximum intensity along each axis. In the radial direction, both the HOM and plane phase focus have HWHM of 0.8 μm. In the axial direction, the HOM focus has a HWHM of 3.9 μm, somewhat smaller than the plane-phase HWHM of 4.3 μm. We conclude that the HOM with $\beta = 1.6$ generates a nearly identical focal volume as a common depletion beam for STED microscopy, but with tighter axial confinement and a brighter annular ring. Furthermore, as resolution improvement from fluorescence depletion scales as the intensity of the depletion signal, we believe the HOM focus could provide (for the same incident power) better resolution improvement for STED microscopy than the mesa phase-plate.

On the other hand, for applications to multi-photon microscopy, a tight, centralized focus is desired. To this end, we also consider the modification of the HOM focus by manipulating the phase of the HOM at the back aperture. While we know that true reconstruction of the fundamental mode (to generate a Gaussian beam focus) is not possible with a simple binary phase plate [9, 10], we can recover a centralized focus for $\beta = 1.6$ with a properly placed phase plate. We verify in our calculations that with a mesa phase plate situated with the π phase step at the null of the HOM, the dark focus disappears. Plots of the radial and axial intensity squared profiles of the HOM focus are shown in Fig. 6.8 (a) and (b), for the HOM and the phase-modified HOM in solid and dashed lines, respectively. Fig. 6.8 (c) and (d) show

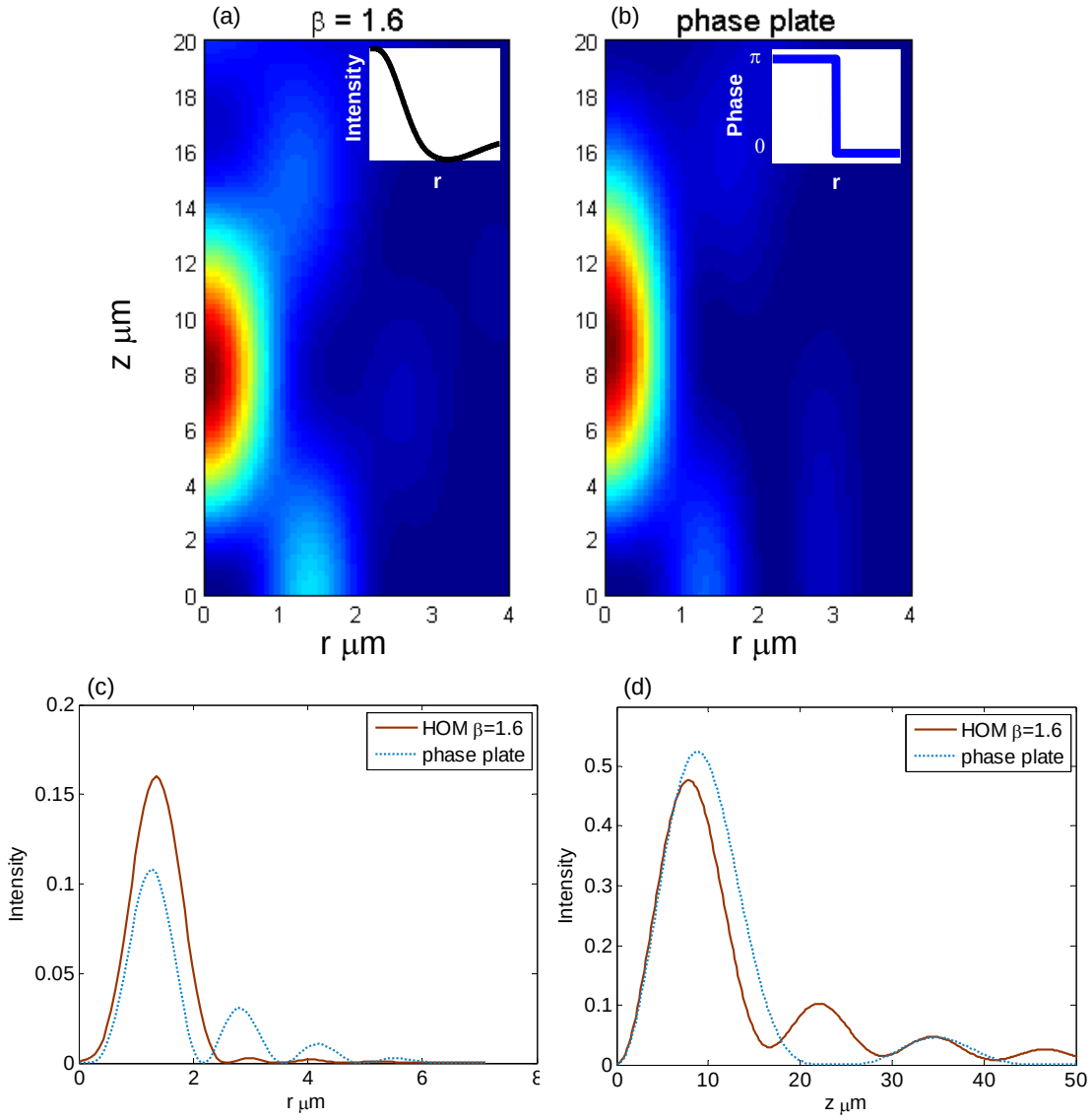

Figure 6.7 Calculated intensity PSFs for (a) HOM with filling ratio $\beta = 1.6$, (b) plane wave with π phase across a central spot 0.71 times the diameter of the beam. Insets in (a) and (b) show radial profiles at back aperture; for (a) intensity as a function of radial distance, (b) phase as a function of radial distance (intensity is uniform). In addition, radial and axial profiles of the point spread functions are shown in subfigures (c) and (d), respectively.

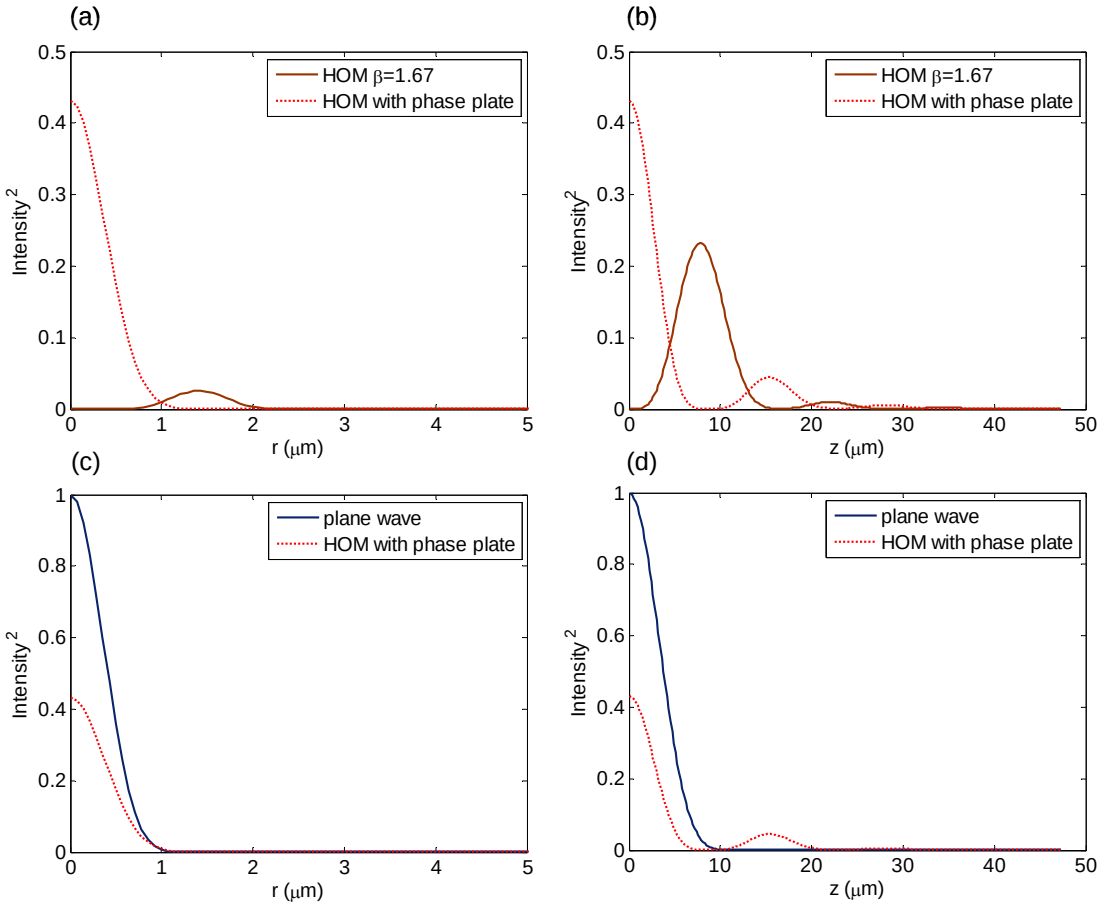

Figure 6.8 Focal properties of an HOM with a phase plate that lends π phase to the outer ring of the HOM, for an HOM with filling ratio $\beta = 1.6$. Calculated radial (a) and axial (b) intensity squared profiles are plotted for the HOM, in the darker solid line, and the HOM with the phase plate, in the brighter dashed line. As a comparison, radial (c) and axial (d) profiles of the focused phase-modified HOM (dashed red) are also plotted with the plane wave focus (solid blue).

the phase- modified HOM focus in comparison to a plane wave focus, the dashed red being the phase-modified HOM, and the solid blue being the plane wave. Power is normalized at the back aperture; we can see that the two-photon excitation efficiency ($\propto I^2$) of the HOM is lower than that of a plane wave, which is not surprising. The lateral FWHM of the phase-modified HOM focus is calculated to be 0.88 μm, slightly larger than the diffraction limited focus. Interestingly, the axial FWHM of the phase-modified HOM focus is smaller than the diffraction limited focus. The secondary peak in the axial distribution at about 15 μm from the focus is likely responsible for this. While the phase plate corrects for the phase at the back aperture, the amplitude profile remains and the focus is still somewhat structured.

6.6 Structured Illumination and its Applications

One very promising application of the HOM focus is to STED microscopy. As was shown above, the HOM at filling ratio $\beta = 1.6$ makes it an ideal candidate to form the depletion beam for a STED microscope. In STED microscopy, the excitation beam (of typical Gaussian mode profile) excites a fluorophore, and a depletion beam with an annular ring in the focal plane follows immediately to de-excite the dye in regions outside the central focus. When the fluorescence from the excitation beam is collected, only the photons emitted from the undepleted regions remain, resulting in an effective excitation volume much smaller than the diffraction limit [8, 11, 12]. STED microscopy requires two light sources of different wavelengths and different focusing properties to be coincident; this is typically supplied by two lasers, beam combiners, and specially fabricated phase plates. With an HOM fiber, we could obtain both the excitation beam and depletion beam from the same device. It was shown in previous chapters that for high pump powers at the output of the HOM fiber, three wavelength bands exist: the residual input, the shifted soliton, and the Cerenkov radiation. The

same LPG that is used to initially launch the light into the LP_{02} mode can be used to reconvert a portion of light back into the fundamental mode, while leaving the remainder of light outside the bandwidth of the LPG in the LP_{02} mode. The multi-wavelength, multi-modal output of the HOM fiber can be collimated and used for STED microscopy directly, without need for beam combination or special phase plates. About 40% of total power should be retained with aperturing of the HOM to achieve the STED focus.

Besides STED, we recognize the many other interesting research problems that can be probed with such a structured focus. It has been demonstrated that dark foci can be created with various phase and interference tricks, as well as from cylindrical vector beams [13-17]. At the focal plane the annular ring could be used for the manipulation of molecules and small particles [18-20], and the 3-dimensional focal "hole" for optical trapping of atoms [21-23].

6.7 Conclusions

We have shown the focusing properties of the LP_{02} mode from a HOM fiber by measuring the TPM PSFs. We showed that by varying the back aperture filling ratio, vastly different PSFs can be obtained. Interestingly, we observed that for a particular back aperture filling ($\beta = 1.6$), a null appeared at the center of the focal spot. The measured two-photon signal contrast of the central dark spot to the bright regions of the focus was 33 dB in the axial direction and 20 dB in the focal plane. We verified in our calculations that the PSF for filling ratio $\beta = 1.6$ matched well with one used for fluorescence depletion in STED microscopy. We also confirmed in our calculations that a centralized focus can be recovered by proper phase manipulation of the HOM. We conclude that the HOM focus is appropriate for multi-photon microscopy for large

and small β, and the focal distribution at $\beta = 1.6$ has great potential for applications in structured illumination microscopy and micromanipulation.

REFERENCES

1. S. Ramachandran, S. Ghalmi, J. W. Nicholson, M. F. Yan, P. Wisk, E. Monberg and F. V. Dimarcello, "Anomalous dispersion in a solid, silica-based fiber," *Optics Letters*, vol. 31, pp. 2532-2534, 2006.

2. L. F. Mollenauer and J. P. Gordon, *Solitons in optical fibers: fundamentals and applications*, Burlington, MA: Elsevier Academic Press, 2006.

3. J. H. Lee, J. van Howe, C. Xu and Xiang Liu, "Soliton Self-Frequency Shift: Experimental Demonstrations and Applications," *IEEE Journal of Selected Topics in Quantum Electronics*, vol. 14, pp. 713-723, 2008.

4. W. R. Zipfel, R. M. Williams and W. W. Webb, "Nonlinear magic: multiphoton microscopy in the biosciences," *Nature Biotechnology*, vol. 21, pp. 1369-1377, 2003.

5. C. Smith, J. W. Nicholson, P. Balling, S. Ghalmi and S. Ramachandran, "Enhanced Resolution in Nonlinear Microscopy Using the LP_{02} Mode of an Optical Fiber," presented at Conference on Lasers and Electro-Optics, 2010, CWL5.

6. B. Richards and E. Wolf, "Electromagnetic Diffraction in Optical Systems. II. Structure of the Image Field in an Aplanatic System," *Proceedings of the Royal Society of London. Series A. Mathematical and Physical Sciences*, vol. 253, pp. 358-379, 1959.

7. Q.-T. Nguyen, P. S. Tsai and D. Kleinfeld, "MPScope: A versatile software suite for multiphoton microscopy," *Journal of Neuroscience Methods*, vol. 156, pp. 351-359, 2006.

8. T. A. Klar, S. Jakobs, M. Dyba, A. Egner and S. W. Hell, "Fluorescence microscopy with diffraction resolution barrier broken by stimulated emission," *Proceedings of the National Academy of Sciences*, vol. 97, pp. 8206-8210, 2000.

9. A. E. Siegman, "Binary phase plates cannot improve laser beam quality," *Optics Letters*, vol. 18, pp. 675-677, 1993.

10. N. Lindlein, G. Leuchs and S. Ramachandran, "Achieving Gaussian outputs from large-mode-area higher-order-mode fibers," *Applied Optics*, vol. 46, pp. 5147-5157, 2007.

11. T. A. Klar, E. Engel and S. W. Hell, "Breaking Abbe's diffraction resolution limit in fluorescence microscopy with stimulated emission depletion beams of various shapes," *Physical Review E*, vol. 64, pp. 066613, 2001.

12. G. Donnert, J. Keller, R. Medda, M. A. Andrei, S. O. Rizzoli, R. LÃ¼hrmann, R. Jahn, C. Eggeling and S. W. Hell, "Macromolecular-scale resolution in biological fluorescence microscopy," *Proceedings of the National Academy of Sciences*, vol. 103, pp. 11440-11445, 2006.

13. J. Arlt and M. J. Padgett, "Generation of a beam with a dark focus surrounded by regions of higher intensity: the optical bottle beam," *Optics Letters*, vol. 25, pp. 191-193, 2000.

14. R. Ozeri, L. Khaykovich, N. Friedman and N. Davidson, "Large-volume single-beam dark optical trap for atoms using binary phase elements," *Journal of the Optical Society of America B*, vol. 17, pp. 1113-1116, 2000.

15. W. Chen and Q. Zhan, "Three-dimensional focus shaping with cylindrical vector beams," *Optics Communications*, vol. 265, pp. 411-417, 2006.

16. M. Rashid, O. M. Maragò and P. H. Jones, "Focusing of high order cylindrical vector beams," *Journal of Optics A: Pure and Applied Optics*, vol. 11, pp. 065204, 2009.

17. D. Yelin, B. E. Bouma and G. J. Tearney, "Generating an adjustable three-dimensional dark focus," *Optics Letters*, vol. 29, pp. 661-663, 2004.

18. K. T. Gahagan and J. Swartzlander, "Simultaneous trapping of low-index and high-index microparticles observed with an optical-vortex trap," *Journal of the Optical Society of America B*, vol. 16, pp. 533-537, 1999.

19. M. Reicherter, T. Haist, E. U. Wagemann and H. J. Tiziani, "Optical particle trapping with computer-generated holograms written on a liquid-crystal display," *Optics Letters*, vol. 24, pp. 608-610, 1999.

20. A. Jonás and P. Zemánek, "Light at work: The use of optical forces for particle manipulation, sorting, and analysis," *Electrophoresis*, vol. 29, pp. 4813-4851, 2008.

21. T. Kuga, Y. Torii, N. Shiokawa, T. Hirano, Y. Shimizu and H. Sasada, "Novel Optical Trap of Atoms with a Doughnut Beam," *Physical Review Letters*, vol. 78, pp. 4713, 1997.

22. P. Xu, X. He, J. Wang and M. Zhan, "Trapping a single atom in a blue detuned optical bottle beam trap," *Optics Letters*, vol. 35, pp. 2164-2166, 2010.

23. L. Isenhower, W. Williams, A. Dally and M. Saffman, "Atom trapping in an interferometrically generated bottle beam trap," *Optics Letters*, vol. 34, pp. 1159-1161, 2009.

CHAPTER 7

CONCLUSIONS AND FUTURE DIRECTIONS

7.1 Summary

In this dissertation, I showed that HOM fiber, when seeded by a short, pulsed source, was capable of generating light pulses in the 1 μm to 1.5 μm range. These pulses arose from the phenomena of SSFS and Cerenkov radiation generation, and were measured to be short (46 fs for the soliton pulse) and energetic (a few nJ in the Cerenkov radiation band). I outlined the demonstration of wavelength-tunable solitons by the power tuning of SSFS in HOM fiber, over wavelength ranges of up to 240 nm. The Cerenkov radiation band, formed as a result of the shifting soliton approaching a zero dispersion wavelength, was shown to be compressible and provided a fixed-wavelength pulsed source at 1.3 μm. A true all-fiber system for generating SSFS and Cerenkov radiation in HOM fiber was also demonstrated by using a few-meter long fiber and a picosecond fiber laser. The all-fiber source was used as the light source for a TPM, confirming its applicability for nonlinear imaging. Lastly, I showed that the focusing properties of the LP_{02} mode emerging from the HOM fiber make it interesting for multi-photon microscopy as well as structured illumination techniques.

7.2 Outlook

7.2.1 Future Fiber Designs

With the demonstration of a functioning all-fiber source for imaging purposes, our eyes turn to probing the true potentials of such a system. We showed that engineering the dispersion in an HOM fiber can predictably change the wavelengths of

the soliton and Cerenkov. Fig. 7.1 shows the dispersion profiles and output spectra from 6 different HOM fibers. We see that the wavelength of the shifted soliton and Cerenkov radiation are precisely determined by the shape of the dispersion curve. In addition to engineering dispersion for wavelength access, new fiber designs are currently under development for producing more energetic pulses, especially enabling more energetic and precisely wavelength-tunable solitons. The HOM fiber designs used in this dissertation all employed the dispersion-decreasing ($dD/d\lambda < 0$) side of the anomalous dispersion regime, causing a shifting soliton that accelerates towards the zero dispersion wavelength. Thus, the exact wavelength of the shifting soliton is very sensitive to changes in input energy. However, if the HOM fiber is designed such that the input pulse is launched on the dispersion-increasing side, the shifting soliton will decelerate as it approaches the dispersion peak, making it less susceptible to input energy fluctuations. In addition, launching the input on the dispersion-increasing side also results in more energetic soliton formation. Calculations have shown that up to 5 nJ solitons can be obtained with appropriate dispersion design. Furthermore, cascaded HOM fiber designs -- multiple fibers with overlapping anomalous dispersion bands -- have also been theoretically investigated for extending the wavelength tuning range of the HOM fibers. Since the dispersion and nonlinearity characteristics of the HOM fibers are highly engineerable, the possibilities are numerous for the design of fibers to target the wavelengths and pulse energies one desires.

7.2.2 Applications of the Higher order Mode for Imaging

One major impetus for the work in this dissertation was for the development of an all-fiber, turnkey source for a multiphoton fiber endoscope. Chapters 5 and 6 showed the HOM fiber's capability as a light source for TPM. Integration with fiber-scanning endoscopes currently under development will bring to reality this dream of a

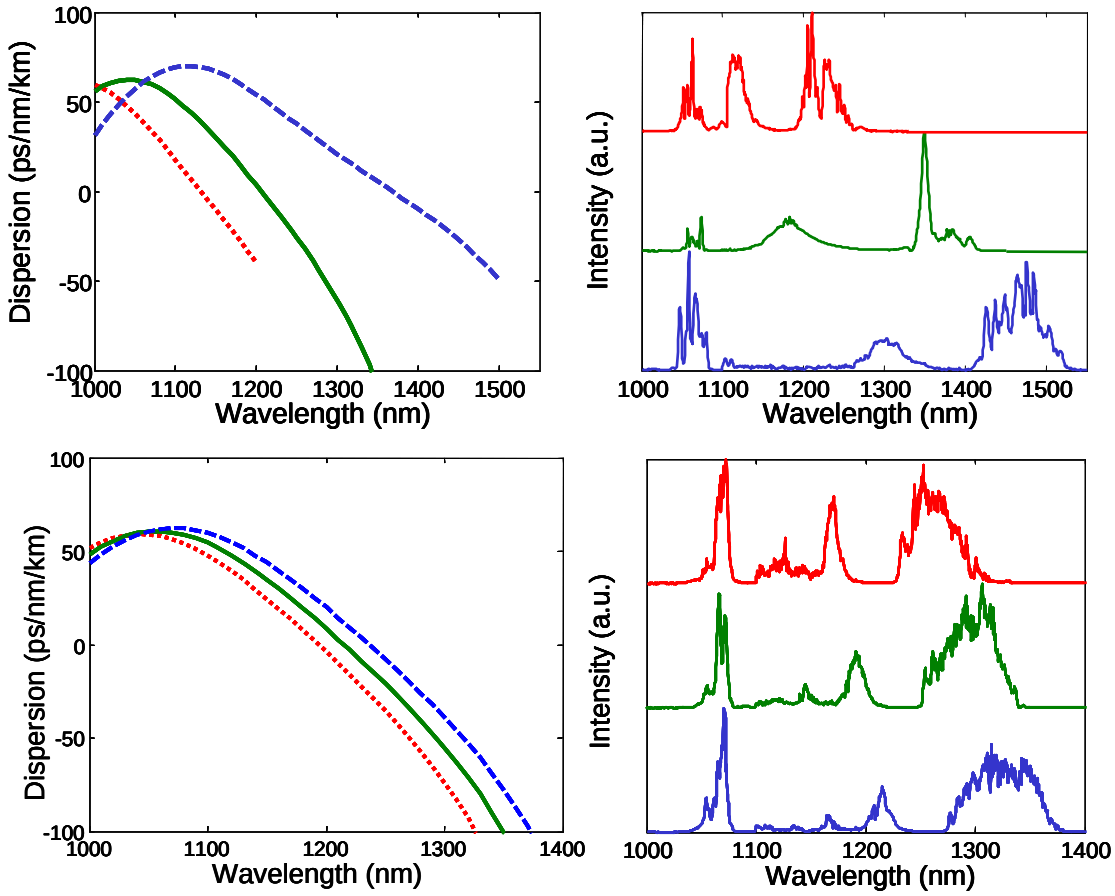

Figure 7.1 Dispersion profiles and measured output spectra for 6 different HOM fibers. For each fiber, the same color is used to plot each dispersion curve and corresponding spectrum. Residual input was attenuated 7dB to accentuate wavelength-shifted features.

compact, easy-to-operate fiber endoscope for minimally invasive optical biopsy and medical diagnostics.

In addition, as was described in Chapter 6, the HOM demonstrates interesting focusing properties with proper aperturing of the mode. A focus with a null at the center and an annular ring on the focal plane can be achieved. This, coupled with the multiple-wavelength output of the HOM fiber, can be an ideal candidate for STED microscopy [1]. By using a LPG to reconvert selected wavelength bands after SSFS and Cerenkov generation in the HOM fiber, one can obtain a dual-mode, multi-wavelength source that could provide both the excitation and depletion beams for a STED microscope system. Recent developments in STED microscopy has pushed its implementation towards fiber-based sources, for ease of alignment and simplification of operation [2, 3]. Even with these, specially fabricated phase plates are still needed to create the depletion beam; our proposed HOM fiber would provide – at the fiber output – the correct beam shapes, without need for external modification of the output light. Furthermore, modal dispersion in fiber can be used to relatively delay the excitation and depletion light as STED requirements demand.

The nonlinear phenomena of SSFS and Cerenkov generation in HOM fibers has shown it to be a suitable medium for creating light sources for nonlinear microscopy. With further design advancements, HOM fibers should emerge as a flexible and versatile platform for applications needing wavelength-tunable and energetic short pulses.

REFERENCES

1. T. A. Klar, S. Jakobs, M. Dyba, A. Egner and S. W. Hell, "Fluorescence microscopy with diffraction resolution barrier broken by stimulated emission," *Proceedings of the National Academy of Sciences*, vol. 97, pp. 8206-8210, 2000.

2. D. Wildanger, E. Rittweger, L. Kastrup and S. Hell, "STED microscopy with a supercontinuum laser source," *Optics Express*, vol. 16, pp. 9614-9621, 2008.

3. D. Wildanger, J. Bueckers, V. Westphal, S. W. Hell and L. Kastrup, "A STED microscope aligned by design," *Optics Express*, vol. 17, pp. 16100-16110, 2009.

APPENDIX A

TIME LENS SOURCES AND THEIR APPLICATION TO IMAGING

A.1 Introduction

The short pulsed light source is a crucial element to exciting nonlinearities in materials. In the main body of this dissertation we discussed the nonlinear phenomena in HOM fibers, as excited by short light pulses. Furthermore, the primary application of this HOM fiber research, nonlinear microscopy, is made possible by short light pulses. The time lens, which manipulates the temporal phase of incident light, is capable of generating short, energetic pulses without laser modelocking (the usual means of creating short pulses). This appendix will cover the principles and implementation of a time lens for generating short pulses. I will show one example of the its application for imaging, in a picosecond light source at 1064 nm, synchronized to a Ti:Sapphire laser for coherent anti-Stokes Raman scattering (CARS) and stimulated Raman scattering (SRS) microscopy.

A.2 Electro-optic modulators

Time lenses in fiber optics are implemented with inline electro-optic (EO) modulators. The modulators used here are made of $LiNbO_3$ crystal, whose refractive index changes when an electric field is applied to it. In a phase modulator (PM), the light passes through a single $LiNbO_3$ waveguide, and when a voltage is applied to the modulator, the change in refractive index in the waveguide causes a phase change (temporal delay) of the input light. An intensity modulator (IM) uses two such waveguides oriented in a Mach-Zehnder (MZ) geometry, with opposite voltage applied to each arm. The interference of the light from the arms of the MZ modulator

produces signal variation from "on" (constructive interference) to "off" (destructive interference). These EO modulators are characterized by a parameter V_π, which denotes the voltage required to induce a π phase shift in the waveguide (V_π is typically a few volts). For PMs, large drive voltages (>> V_π) are desired for maximal phase shifts. As such, RF (radio frequency) amplifiers for generating PM drive signals need to be high power and placed close (due to loss of RF connections and cables) to the modulators themselves. For IMs, V_π gives the voltage required to sweep from "on" to "off." Correct amplitude of drive voltage as well as proper setting of bias voltage is crucial to obtaining maximum extinction ratio (ER, light intensity at "on" compared to "off") and minimum insertion loss. Standard ER values for IMs used in telecommunications are ~20 dB, and higher ERs can be achieved with fine voltage control or multi-stage modulators. These EO modulators are used in telecommunications for data encoding in transmitters, and are capable of modulating at speeds in the tens of GHz.

A.3 Using time lenses to create short pulses

The time lens works in the temporal domain much as a spatial lens does in space. A focusing lens imposes a quadratic phase profile on a planar wavefront; this combined with propagation (diffraction) brings the light to a focus. In analogy, an ideal time lens imposes a quadratic phase profile on a pulse. The generated chirped bandwidth, with appropriate propagation (dispersion) to remove the chirp, produces a "temporal focus": a short pulse [1, 2]. We can write the phase in space imposed by a lens:

$$\varphi(x,y) = \frac{k(x^2 + y^2)}{2f} \tag{A.1}$$

Where k is the propagation wave vector, and f is the focal length of the lens. Similarly, the phase induced by an ideal time lens has the form

$$\varphi_{PM}(t) = \frac{-\omega_o t^2}{2f_t}, \tag{A.2}$$

Where f_t represents the "focal length," or strength, of the time lens. It is easy to see how a sinusoidal phase drive can approximate this profile: an RF phase drive with modulation frequency ω_m and peak-to-peak voltage $V_{p\text{-}p}$ applied to an EO PM with characteristic V_π, can be expanded in a Taylor series:

$$\varphi_{PM}(t) = \pi \frac{V_{p-p}}{2V_\pi}\cos(\omega_m t) \approx 1 + \frac{-\omega_o t^2}{2f_t} \tag{A.3}$$

The leading term in the expansion is a constant phase across the whole pulse, which we can disregard. The effective time lens "strength" f_t is given by:

$$f_t = \frac{2V_\pi}{\pi V_{p-p}}\frac{\omega_o}{\omega_m^2} \tag{A.4}$$

We can see that a larger peak-to-peak drive voltage and higher modulation frequency applied to the PM gives smaller f_t and thus "tighter focusing," which in turn creates shorter pulses.

We consider this phase on a Gaussian pulse with 1/e half-width τ_0:

$$E_0 \exp\left(\frac{-t^2}{2\tau_0^{\,2}}\right)\exp(i\varphi_{PM}) = E_0 \exp\left[\frac{-t^2}{2\tau_0^{\,2}}\left(1 + i\frac{\omega_0 \tau_0^{\,2}}{f_t}\right)\right] \tag{A.5}$$

This takes the same form as chirp C applied to a Gaussian pulse [3], chirp that can be subsequently removed by dispersion compensation.

$$E_0 \exp\left[-\frac{t^2}{2\tau_0^{\,2}}(1 + iC)\right] \tag{A.6}$$

A typical time lens setup for generating low-duty cycle short pulses is shown in Fig. A.1(a). A continuous wave (CW) laser is first carved into a low-duty cycle pulse train by an IM. The pulses emerging from the IM are long (tens of picoseconds at best), due to finite bandwidth of the RF electronics. To obtain the wide bandwidth

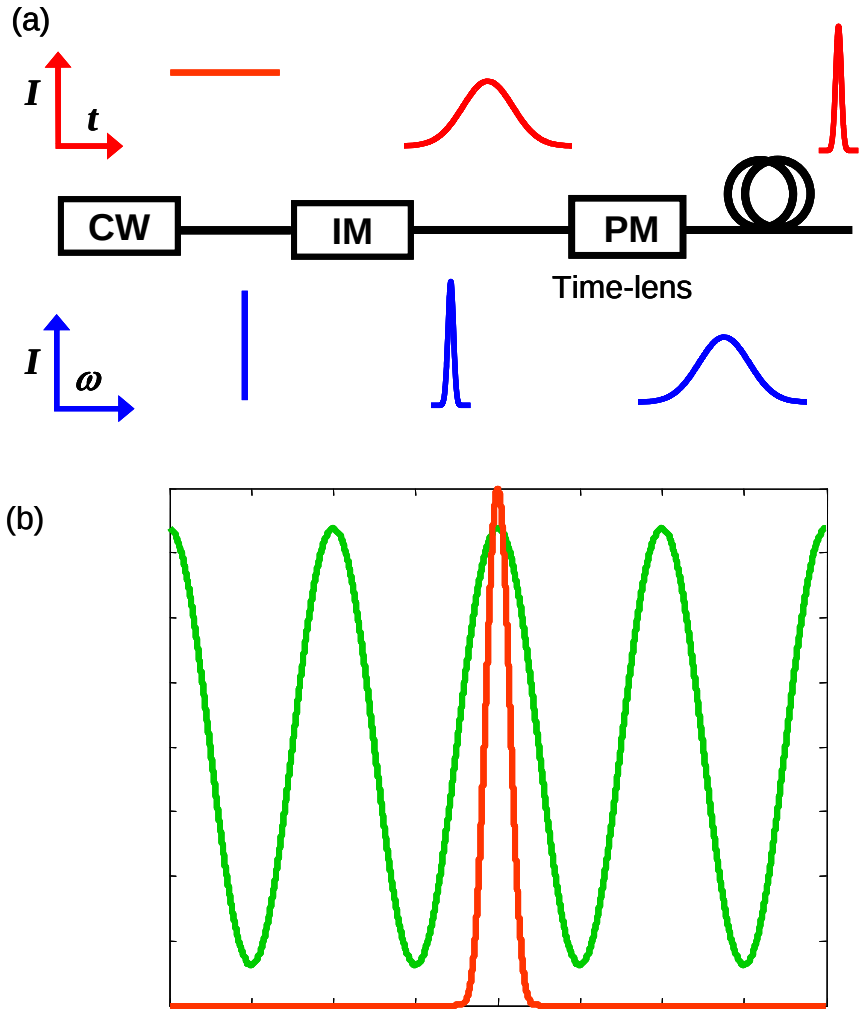

Figure A.1 (a) A typical time lens setup. Red profiles denote temporal shape at points along the system, blue profiles denote spectral shape. (b) Alignment of sinusoidal phase drive (green) with optical pulse envelope (red) for a time lens. CW: continuous wave laser, IM: intensity modulator, PM: phase modulator.

associated with a short pulse, a time lens is required. A PM is driven with a high repetition rate sinusoid, synchronized such that the cusp of the sinusoid aligns with the peak of the pulses, approximating a quadratic phase profile (Fig. A.1(b)). Appropriate dispersion compensation matched to the chirp acquired from the time lens then compresses the pulse. Optical fiber amplifiers can be added inline to boost the signal as needed. Amplification before the dechirping step sees minimal nonlinear penalty as the peak power before compression is relatively low.

The key to generating maximal bandwidth (and consequently the shortest pulse) is the alignment of the phase curvature with the pulse profile. This is easiest achieved by delaying the RF signal driving the PM. To ensure that each pulse acquires the same bandwidth from the time lens, the RF signal driving the IM (a low duty cycle pulse train) and the PMs (a high repetition rate sinusoid) must be synchronized. Either the pulse carver signal can be clocked by the PM signal, or the PM signal can be derived from the pulse carver signal. Typically, a precision frequency synthesizer, which generates a single pure high frequency tone, supplies the signal for the PM. This same single RF frequency is also used as the clock signal to a pulse pattern generator that creates the RF signal to drive the IM. The example we present here does the opposite: a high harmonic of the low duty-cycle drive signal for the IM is filtered and amplified to drive the PM.

It is instrumental to note that while we drew in Fig. A.1(b) the alignment of the pulse with a negative phase curvature ($\varphi_{\mathrm{PM}} \sim -t^2$), the sinusoidal drive can generate the same bandwidth with either sign of chirp depending on which cusp is aligned to the pulse. This gives flexibility to the dispersion compensation techniques one can use to remove the chirp from the pulse, from free space dispersion compensators like gratings and prisms, to fiber-based compensators like standard single mode fiber, dispersion compensating fiber, and chirped fiber Bragg gratings.

Also, we note that components of the time lens system do not need to go in any particular order: PMs and IMs can be swapped in position with no effect on the resulting outcome. In fact, the time lens does not need an IM to generate short pulses. However, as only a portion of the sinusoidal RF signal is well-matched to the parabolic phase profile, many sidelobes result in the temporal profile of the output pulse. We use the IM here to reduce these sidelobes, as well as lower the duty cycle of the pulsetrain. Whereas the modulators can be exchanged in position, amplifier position is of more importance: to maintain a high optical signal-to-noise ratio, amplifiers must be used along propagation to compensate for component insertion loss. In addition, final power amplification should be before pulse compression to reduce nonlinear distortions to the pulse.

In contrast to laser modelocking, using a time lens to generate short pulses requires no cavity or feedback, and thus the repetition rate can be widely tuned and pulses can even be generated "on demand." In addition, the output wavelength of the time lens source can be changed simply by changing the initial CW laser. The modulators, as they are designed for wavelength-division-multiplexed applications in telecommunications, have good performance over many tens of nanometers. Another benefit of the non-modelocking nature of time lens sources, as it is completely feed-forward and deterministic, means that its operation is reliable and predictable. During operation, only minor adjustments to IM bias from day to day are needed to maximize ER, and these adjustments can be incorporated into an electronic feedback control loop for optimization, enabling simple, fuss-free operation. Further, as the optical and electrical components used in a time lens system are standard to telecommunications, they are low-cost and robust. Time lens systems at wavelengths outside standard telecommunication bands operate on the same principle, but its optical components

(CW lasers, EO modulators, amplifiers) incur slightly higher cost due to lower market demand.

A.4 Synchronized time lens source for CARS and SRS microscopy

While time lenses can be used independently to generate short pulses [4, 5], we show in this section the adaptability of the time lens for creating a pulsed source synchronized to a master oscillator for CARS and SRS microscopy. CARS [6] and SRS [7] microscopy are nonlinear imaging techniques that require no contrast agents. These techniques use two wavelengths of light to probe molecular vibrations, the optical frequencies of the two beams separated by the vibrational frequency of the molecule $\omega_{vib} = \omega_{pump} - \omega_{Stokes}$. These coherent Raman microscopy techniques require two synchronized, pulsed laser sources to be spatially and temporally overlapped at the microscope focus. In addition, each laser needs to have a narrow linewidth as to only probe a single molecular vibration of interest. Moreover, wavelength-tunability of one of the laser sources is desired to be able to target different molecular vibration lines. CARS and SRS microscope systems typically employ modelocked laser sources to satisfy these requirements, but the synchronization of multiple modelocked lasers is a nontrivial problem. Early systems used electronic feedback circuits to synchronize laser cavity lengths [8], but these eventually gave way to optical synchronization [9]. Currently, the workhorse laser system for CARS and SRS microscopy is a picosecond Nd:YAG laser at 1064 nm and a synchronously pumped optical parametric oscillator (OPO) tunable from 800 to 1000 nm. A portion of the Nd:YAG laser output is used as the Stokes beam, and the majority of it is frequency-doubled to pump the OPO, which serves as the pump beam. While suitable for laboratory research, such laser systems are cumbersome and make it difficult for these powerful microscopy techniques to see clinical application. We describe here an alternative to this by using a time lens source

synchronized to a pulsed laser source. A tunable-wavelength Ti:Sapphire laser provides the pump pulse, and the time lens source provides the Stokes pulse. We show low jitter between the time lens source and its master oscillator Ti:Sapphire laser, and successful demonstration of CARS and SRS imaging with this system.

Since CARS and SRS microscopy requires picosecond pulses for optimal signal-to-background, molecular specificity, and damage performance, two PMs (lumped as a single time lens) are used to generate the bandwidth required. A simplified schematic of the synchronized time lens system is shown in Fig. A.2. A Ti:Sapphire laser (Coherent) served as the master oscillator, its 76 MHz, 2 ps pulses were tunable between 700 nm and 1000 nm. The time lens source consisted of a single-mode, 1064 nm DFB laser (Qphotonics), two PMs (EOSpace) to generate the chirped bandwidth, an IM (PP1, EOSpace) to carve a pulsetrain matching the master oscillator, Ytterbium-doped fiber amplifiers to boost the optical signal, and a circulator (Novawave) and chirped fiber Bragg grating (Teraxion) for dispersion compensation. A second IM (PP2, EOSpace) was added in the system for modulation of the Stokes beam for SRS imaging, and when not used (in the case of CARS imaging), could be set to a constant bias voltage to allow maximum transmission. The electronic drive signals for the time lens components were derived from the master oscillator. The Ti:Sapphire light was tapped with a beamsplitter and directed to a high speed electro-optic detector (EOT), which output an RF pulsetrain at the same repetition rate as the master oscillator. Due to the response time of the detector, the RF pulses were ~60-70 ps long. The RF signal was divided and one branch was used to drive PP1, creating a low-duty cycle pulsetrain. The other branch was filtered with a narrowband RF filter centered about 9.95 GHz, and this filtered signal (the 131st harmonic) was used to drive the PM for the time lens. RF amplifiers were used to

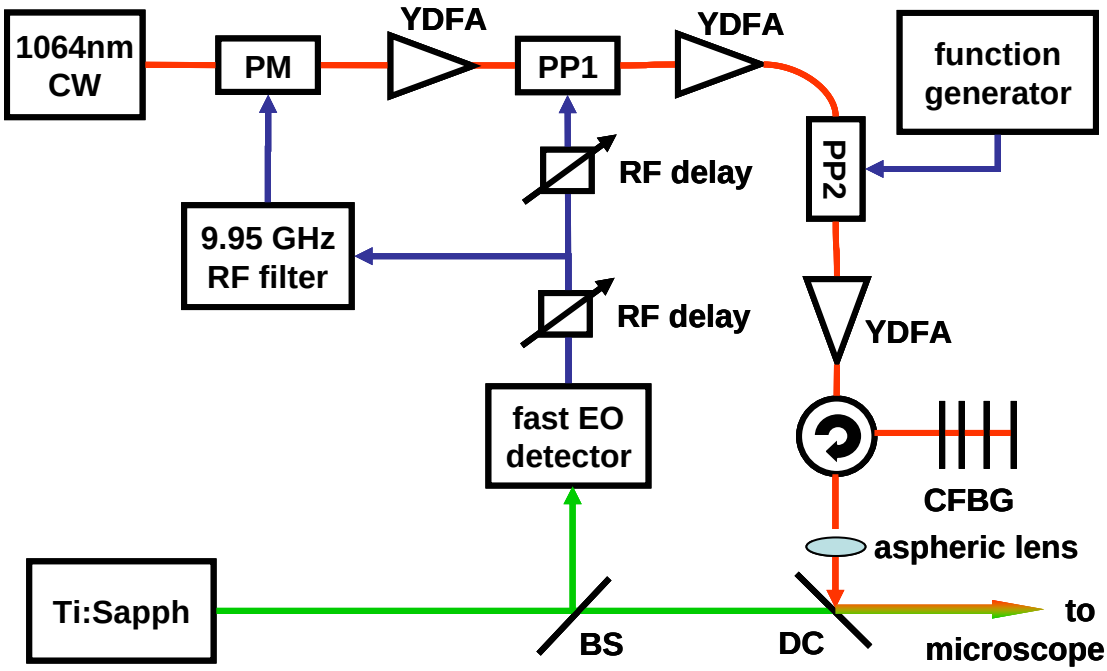

Figure A.2. Simplified schematic of time lens source for CARS and SRS microscopy. Red lines denote optical path of 1064 light, green lines indicate Ti:Sapph optical path, blue lines mark the RF signal path. CW: continuous-wave laser, PC: pulse carver, YDFA: Ytterbium-doped fiber amplifier, PM: phase modulator, PP: pulse picker, EO: electro-optic, CFBG: chirped fiber Bragg grating, BS: beamsplitter, DC: dichroic mirror.

boost signal strength applied to the modulators. An RF delay line before the split controlled the delay of the pulsetrain, and another delay line at the RF signal input to PP1 ensured the phase modulation was properly aligned with the pulse. The fiber-coupled output of the time lens was then collimated with a 0.18 NA aspheric lens and combined with the Ti:Sapphire beam with a dichroic (DC) mirror. The combined beams were sent to a beamscanning microscope for imaging [10]. Spectrum of the time lens output was measured with an optical spectrum analyzer. Temporal characterization of the time lens source was conducted by measuring its sum frequency cross-correlation with the master oscillator.

The spectral and temporal characteristics of the time lens source are shown in Fig. A.3. The output spectrum after amplification and compression is shown in Fig. A.3(a), the inset shows a zoomed view near the center wavelength. We see the characteristic modulated spectrum of a time lens, showing ~2 nm of bandwidth. The pulsewidth of the time lens source was ~1.7 ps, measured by cross-correlation with a synchronized 130 fs fiber laser source. Fig. A.3(b) shows a cross-correlation of the time lens source with the master Ti:Sapphire. The cross-correlation has a width of ~2.9 ps, a convolution of the Ti:Sapphire and the time lens pulsewidths. The inset of Fig. A.3(b) plots the sum frequency signal at the half-maximum point of the cross correlation, showing good long-term jitter performance. Fig. A.3(c) shows the modulated time lens source (Stokes beam) in blue and the unmodulated Ti:Sapphire (pump beam) in the green. Modulation was accomplished by applying a 10 MHz square wave to PP2. As 10 MHz is not an integer factor of the fundamental repetition rate, occasionally the pulse groups show different numbers of pulses. The modulated pulsetrain shows excellent modulation depth, which is crucial to successful SRS microscopy.

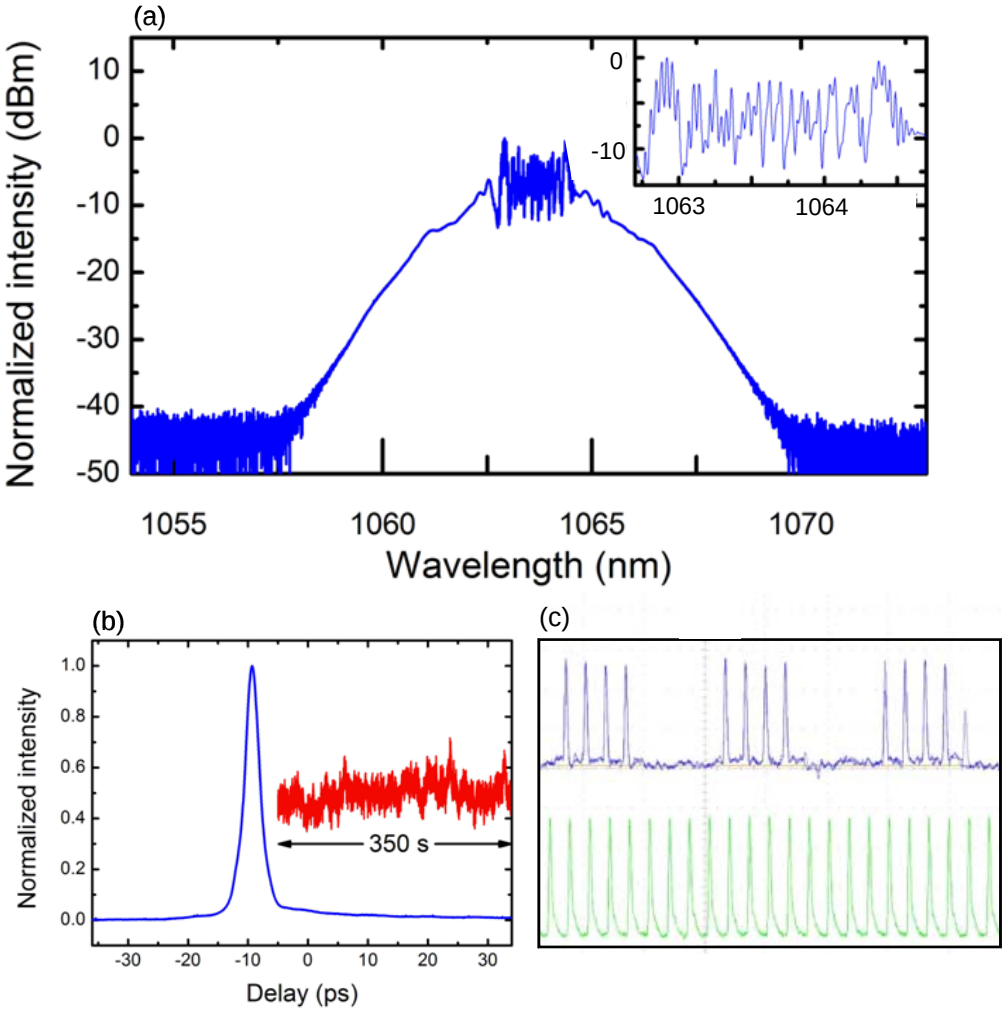

Figure A.3. Output of the time lens source. In (a), the output spectrum, in log scale. Inset shows fine spectral features at the center wavelength. Cross-correlation of time lens source with Ti:Sapph laser is shown in (b), inset shows stability of signal at half-maximum. (c) shows recorded pulsetrains of Ti:Sapph laser in green and time lens source modulated at 10 MHz in blue.

The time lens source synchronized to the master Ti:Sapphire laser was used for CARS and SRS imaging of mouse skin. SRS images of various structures in the skin are shown in Fig. A.4(a-c). Structures shown are (a) a sebaceous gland, (b) the viable epidermis, and (c) the *stratum corneum*. The Ti:Sapphire was tuned to 817 nm to match the CH_2 vibration at 2850 cm^{-1}, which highlights the lipid-rich regions of the skin tissue. Fig. A.4(d) shows drug penetration into the spaces between corneocytes in the *stratum corneum*. For this image retinoic acid was applied to the mouse skin, and the Ti:Sapphire was tuned to 909 nm to match the resonance of retinoic acid at 1600 cm^{-1}. The images show no adverse effects from jitter, which would manifest itself in nonuniformity of image brightness.

The time lens source demonstrated here is flexible, as it can be synchronized to any optical or electrical pulsetrain. Since the time lens pulses are simply triggered by the master oscillator, there is no feedback involved and the synchronization is instantaneous. The time lens source has additional flexibility because the pulses can be generated "on demand," and pulse amplitude varied pulse-to-pulse. Also, while in this demonstration the time lens source was fixed-wavelength, the wavelength of the time lens could be changed by replacement of the CW seed laser.

The time lens source is convenient, as it provides a mechanism to delay its pulses without changing optical alignment. The RF delay simply controls the electrical signals triggering the time lens pulses, and the fiber-coupled output of the time lens is temporally delayed without movement of the optical beam. Fine control of the delay is accomplished through manual and electronically controlled RF delay lines, but large amounts of delay can be added or subtracted by addition or removal of RF cables and optical fibers. In addition to the alignment-free control of pulse delay, modulation of the pulsetrain for SRS and other pump-probe type experiments is incorporated to the system, without need for external modification of the optical beam. In this

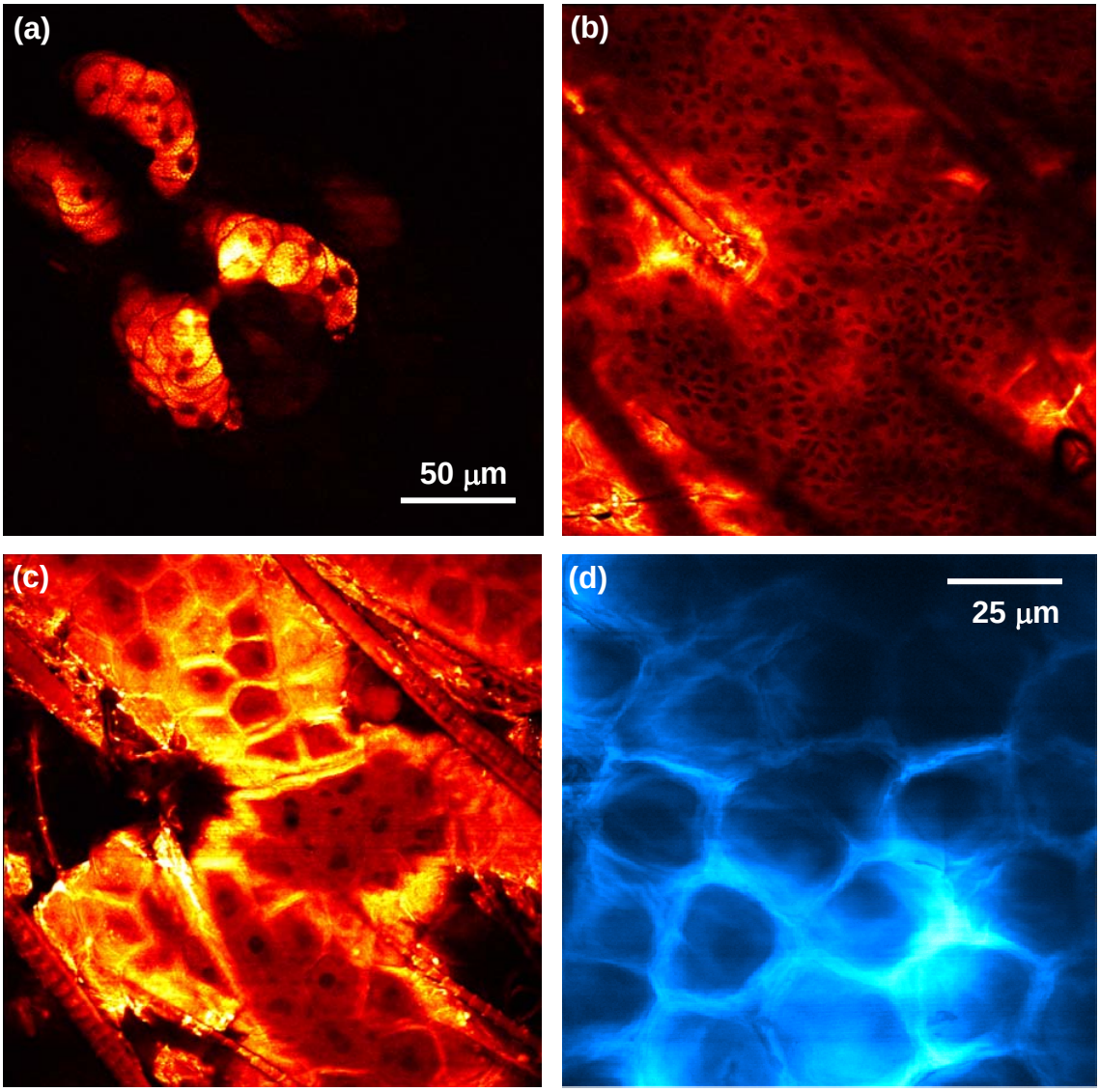

Figure A.4. Sample SRS microscopy images taken with the time lens source, of (a) the sebaceous gland, (b) viable epidermis, and (c) stratum corneum of mouse skin, imaged by probing the CH_2 resonance (2850 cm^{-1}). (d) shows drug delivery through mouse skin, imaged by probing the resonance of retinoic acid (1600 cm^{-1}). Scale is as shown in (a) and (d). Scale in (a) applies also to (b) and (c).

demonstration a second IM was used to achieve this modulation capability, but it could also be accomplished by electrically mixing the SRS modulation signal with the input signal to PP1, or by directly modulating the CW seed laser.

A.5 Conclusions

We have shown here that the time lens-based pulsed source is viable for nonlinear imaging applications. We demonstrated a time lens source synchronized to a tunable-wavelength modelocked laser for CARS and SRS microscopy. The time lens source provides a low-jitter synchronized pulse train, allows for alignment-free tuning of pulse delay, and has integrated pulsetrain modulation capability. Furthermore, as the system is all-fiber, it is robust and easy-to-transport, and can be a very compact system with proper packaging.

REFERENCES

1. B. H. Kolner and M. Nazarathy, "Temporal imaging with a time lens," *Optics Letters*, vol. 14, pp. 630-632, 1989.

2. J. van Howe and C. Xu, "Ultrafast optical signal processing based upon space-time dualities," *Journal of Lightwave Technology*, vol. 24, pp. 2649-2662, 2006.

3. G. P. Agrawal, *Nonlinear Fiber Optics*, San Diego, California: Academic Press, 2001.

4. J. van Howe, J. Hansryd and C. Xu, "Multiwavelength pulse generator using time-lens compression," *Optics Letters*, vol. 29, pp. 1470-1472, 2004.

5. J. van Howe, J. H. Lee and C. Xu, "Generation of 3.5 nJ femtosecond pulses from a continuous-wave laser without mode locking," *Optics Letters*, vol. 32, pp. 1408-1410, 2007.

6. C. L. Evans and X. S. Xie, "Coherent Anti-Stokes Raman Scattering Microscopy: Chemically Selective Imaging for Biology and Medicine," *Annu. Rev. Anal. Chem.*, vol. 1, pp. 883-909, 2008.

7. C. W. Freudiger, W. Min, B. G. Saar, S. Lu, G. R. Holtom, C. He, J. C. Tsai, J. X. Kang and X. S. Xie, "Label-Free Biomedical Imaging with High Sensitivity by Stimulated Raman Scattering Microscopy," *Science*, vol. 322, pp. 1857-1861, 2008.

8. E. O. Potma, D. J. Jones, J.-X. Cheng, X. S. Xie and J. Ye, "High sensitivity coherent anti-Stokes Raman scattering microscopy with two tightly synchronized picosecond lasers," *Optics Letters*, vol. 27, pp. 1168, 2002.

9. F. Ganikhanov, S. Carrasco, X. S. Xie, M. Katz, W. Seitz and D. Kopf, "Broadly tunable dual-wavelength light source for coherent anti-Stokes Raman scattering microscopy," *Optics Letters*, vol. 31, pp. 1292-1294, 2006.

10. CARS and SRS imaging was conducted at Harvard University, in collaboration with Sunney Xie's group. For details about the microscope setup and sample preparation please see Science **322**, 1857 (2008)